
Artificial cilia for microfluidics

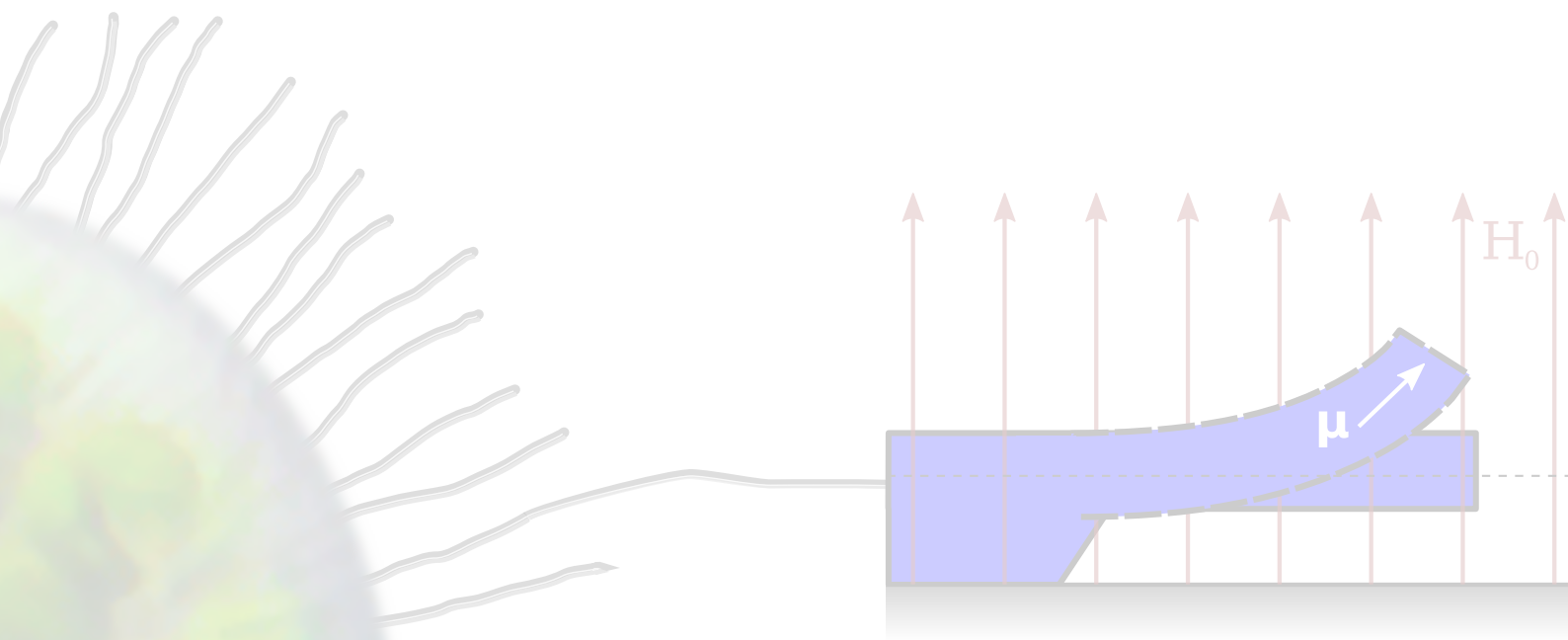
exploring the use of a horizontally micro-structured ferromagnetic PDMS composite

master's thesis of
Willem van Engen

2007 - 2008

research carried out at
Eindhoven University of Technology
Department of applied physics
Molecular biosensors for medical diagnostics (MBx)

under supervision of
M.Sc. F. Fahrni and dr. L.J. van IJzendoorn



Abstract

Cilia are thin, flexible rods found in nature which induce mixing and pumping on a microscale. This way of inducing motion in a fluid can be applied to the domain of microfluidics. As a step towards microfluidic control by artificial cilia, magnetic actuation of artificial cilia was investigated in theory and tested in practise by feasibility prototypes; both confirmed the possibility of inducing motion in ferromagnetic artificial cilia using a magnetic field.

The bending of a cilium as a result of a magnetic field was estimated theoretically for a paramagnetic as well as a ferromagnetic material; the former in the high-gradient field of a current wire, and the latter in the homogeneous field of a magnet. When combined with an estimation of the parameters involved, the resulting cilia movement favoured the ferromagnetic cilium, which could achieve a greater deflection than the paramagnetic cilium and whose behaviour was independent of scaling. Both showed a p^3 -dependence on aspect-ratio.

Feasibility prototypes were created for experimental verification. The soft polymer polydimethylsiloxane (PDMS) was used as a material for artificial cilia. It was doped with 70nm Fe@C particles to make it magnetic. Characterisation by a vibrating sample magnetometer (VSM) showed that the magnetic behaviour was independent of the concentration of magnetic particles in PDMS, with which the saturation magnetisation M_s , remanent field M_r and susceptibility χ scaled linearly. Extrapolating the measurements to a 100vol% Fe@C-PDMS composite resulted in $M_s = 0.6\text{MA/m}$, $M_r = 0.16M_s$ and $\chi \approx 5$. The coercive field was measured to be $H_c = 17.5\text{mT}$. Field-curing of the composite did not substantially enhance its magnetic properties.

To obtain micro-fabricated high-aspect ratio structures, PDMS was structured horizontally using a sacrificial layer lift-off technique. For this procedure, two photosensitive PDMS formulations were investigated, of which s-PDMS was selected. This resulted in micro-structured artificial cilia of about $10\mu\text{m}$ in thickness and $250\mu\text{m}$ in length. Actuation with a 50mT field resulted in a deflection of about $180\mu\text{m}$, which was in the same order of magnitude as calculated from theory and VSM measurements. Also artificial cilia with a size of one order of magnitude larger were found to behave accordingly. Although the actuating field exceeded the coercive field of the composite, a permanent moment perpendicular to the field was shown to remain and cause the cilium to deflect.

Preface

Nature is full of wonderful things. Surprising things, living things. In normal life, we see the outside, and marvel at its beauty. In science, we look at the matter inside. Zooming in (and out) at different levels, new things are discovered. Interconnections are made between the world we perceive normally, and the larger and smaller things. And we are led to wonder again, discovering beauty, complexity and efficiency.

Not only do we venture to describe or understand these worlds, there is also the application of ideas found to our own problems, the world acting as a sort of idea-pool with proved track records. Human flight, for example, can be found as early as in the myth of Icarus, who escapes from the island of Crete by a pair of feather wings. The existence of birds who can fly using wings can be seen as working prototypes: a convincing argument that the principle of flight using wings is attainable. And indeed, aeroplanes are all too common nowadays. They are not exact copies of the example set by nature, since the materials and production methods we use are different from nature's, and so are our requirements. But aviation has become a reality because of a founded belief that such is attainable. That is why nature-inspired design, if treated with some care, is a fruitful endeavour.

And then the nature-inspired idea meets science, the continuous process that refines our description of nature. Inspiration meets technology, which applies science to create something tangible; a fusion between the something found in nature, and the technological world we have shaped; something new.

This work begins with an idea present in nature: cilia, small moving tentacles that can be found in organisms. When combined with scientific theories and technological fabrication methods, something tangible can emerge; a step towards microfluidic control by means of magnetically actuated artificial cilia.

This document contains many hyperlinks in its digital form, which are not accessible in the hardcopy version. If you happen to be in possession of the latter, you can find the digital version on the website mentioned below. Additional material, like full-page experimental graphs and numerical data, will be available at the same place.

<http://willem.engen.nl/uni/intern-mba/>

Contents

1	Introduction	9
1.1	Cilia in nature	9
1.2	Microfluidics	10
1.3	Cilia for microfluidics	10
1.4	Approach	11
1.5	Related work	11
1.5.1	Magnetic micro-actuators	11
1.5.2	Artificial cilia in microfluidics	12
1.6	Thesis overview	12
2	Design	13
2.1	Introduction	13
2.2	An engineer's theory	13
2.2.1	Force	13
2.2.2	Torque	14
2.2.3	Anisotropy	14
2.3	Exploring the parameters	18
2.3.1	Magnetic field	18
2.3.2	Material	18
2.3.3	Dimensions	19
2.3.4	Magnetic composite	19
2.4	Expected order of magnitude	22
2.4.1	Scaling behaviour	24
2.5	Conclusion	25
3	A permanently magnetic PDMS composite	27
3.1	PDMS	27
3.2	Particle selection	28
3.3	Fabrication	28
3.3.1	Dispersion	28
3.3.2	Casting & curing	28
3.4	Result	30
3.4.1	Optical inspection	30
3.4.2	Magnetic characterisation	32
3.5	Conclusion	35

4	Micro-fabrication of artificial cilia	37
4.1	Photosensitive PDMS	37
4.1.1	photoPDMS	38
4.1.2	s-PDMS	40
4.1.3	Conclusion	42
4.2	Permanently magnetic photosensitive PDMS	42
4.3	Micro-structured artificial cilia	43
4.3.1	Procedure	43
5	Feasibility prototypes	47
5.1	Large	47
5.1.1	Estimation of induced moment	48
5.1.2	The coercive field	49
5.2	Small	52
5.2.1	Very long cilia	54
5.3	Conclusion	54
6	Conclusion & outlook	55
6.1	Conclusion	55
6.2	Outlook	56
A	Critical diameters in nano-magnetism	59
A.1	Single- and multi-domain particles	59
A.2	Homogeneous rotation	60
A.3	The superparamagnetic limit	61
A.4	The different regimes	61
A.5	Critical diameters for selected materials	62
B	Commercially available ferromagnetic micro- and nanoparticles	65
B.1	Iron nanoparticles	65
B.2	Cobalt nanoparticles	66
B.3	Nickel nanoparticles	66
B.4	Alloy nanoparticles	66
	Bibliography	67

Chapter 1

Introduction

1.1 Cilia in nature

Cilia are tail-like protrusions on a cell, extending into the surrounding liquid or gas. Discovered in 1898[56] but not well understood until the 1990s, they are a good example of how an organism interacts with a fluid or gas on a microscale. Cilia can either probe the environment for sensory information, or set the surroundings in motion by bending to and fro themselves. The former, non-motile cilia, are sensory organelles found for example in the human nose, ear and eye; in kidneys, non-motile cilia send signals to a cell when they bend in response to a fluid flow.

Motile cilia constantly beat in one direction, inducing movement in the surrounding fluid. Many of these are often found together to create a substantial effect. This type of cilium often exists in mammals, including humans. In the windpipe, they filter and transport dirt toward the nostrils. In the brain, they enhance ion transport by inducing mixing [13]. Another notable example of motile cilia is found in the single-celled organisms called paramecia (figure 1.1). These rugby-ball shaped cells are covered completely with cilia, with which it moves itself through the fluid and draws food into its cell mouth. Paramecia are 50-350 micrometres in length, may have five to six thousand cilia, and reach speeds of 0.4-2 millimetres per second [32, 96]. This shows that cilia have a great potential in fluid manipulation on a milli- and micrometre scale.

Most cilia are about 5-10 micrometres long and about 0.2 micrometres in diameter [33, 95]. Because of the small size, it is not straightforward to do *in vivo* mechanical measurements. The larger motile cilia found in the common mussel (*mytilus edulis*) have been measured, however. They are



Figure 1.1: Paramecium bursaria, a single-celled organism that is covered with cilia by which it moves through the surrounding fluid. [61]

up to 100 micrometres long and about 3 micrometres in diameter. The Young's modulus was measured to be 5-9 GPa for various sizes [9]. In related work, a Young's modulus of 0.1 to 1 gigapascal was found for micrometre-sized cilia-like structures of haircells in the cochlea [70]. Sperm flagella (the much longer brothers of cilia) have been measured to have a Young's modulus of several gigapascal [8, 14].

Much more can be said on the subject of cilia and similar organic structures found in nature. But having touched the surface of this concept, it's time to look at an application area that may benefit from this.

1.2 Microfluidics

In the past couple of decades, miniaturisation of electronic devices has changed everything related to computation, information and communication. From a technical point of view, downscaling of individual components that build up an electronic circuit have been key to this: transistors, resistors, and the like. A similar development is taking place in chemistry and biology. Complex chemical reactions happen on a large scale in chemical plants, and biological tests are being carried out with tabletop analysis systems. When these techniques are scaled down in size, new possibilities arise. Small-scale custom synthesis can be done without the overhead of large-scale methods. And the lesser amount of input sample needed would convenience, for example, patients giving blood for medical tests. The small scale on which the process takes place can also accelerate research on small phenomena that is otherwise much more complicated; measurement and manipulation of single cells and DNA molecules, for example [27, 35, 49, 83].

To achieve miniaturisation of biochemical devices, miniaturised building-blocks are needed: channels, valves, pumps, mixers, etc. These can be put together into a single device, much like a digital microchip consists of minuscule resistors, tran-

sistors, and the like. Such a microfluidic chip has been named *micro total analysis system* (μ TAS), or *lab-on-a-chip* (LoC). When they are commercially available, it opens up new possibilities in all areas related to chemistry and biology: molecular analysis, bio-defence, cell biology, chemical synthesis, medicine, heat management, and more [65, 74].

Already microfluidic consumer devices have begun to appear. Blood glucose meters for diabetes patients may be the first and most simple example, and they are all too common nowadays. The Biosite Triage system is a more sophisticated commercial example, which contains a microfluidic network for blood analysis in a disposable cartridge [44]. More complex devices are being developed, like a wristwatch that is able to measure multiple blood parameters [51], or an *in vivo* wireless drug-delivery microchip [87]. In laboratories, complex microfluidic devices are being used [99], as shown in figure 1.2. Still a lot of work is needed to bring microfluidics to the masses.

An important technological issue is the availability of microfluidic building-blocks that are small, easy to use, and easy to produce. For disposable components, low cost is another important issue. It is here that the idea of cilia can be of use: they can be put to work as actuators micro-pumps and micro-mixers.

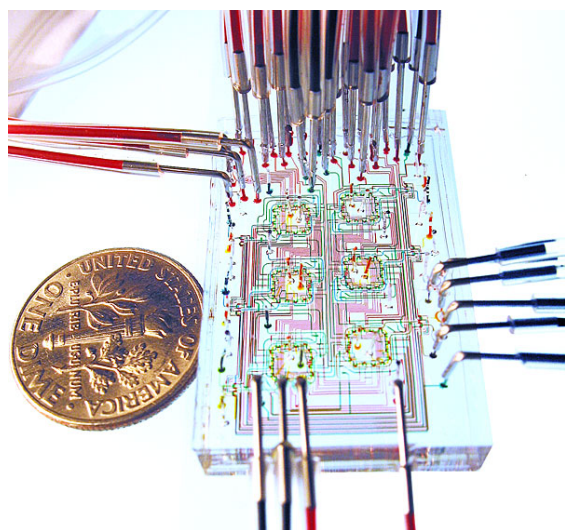


Figure 1.2: A microfluidic bioreactor for the monitoring of bacteria with single-cell resolution, which can dynamically control population density. [59, 72]

1.3 Cilia for microfluidics

Motile cilia have been found to induce fluid movement (section 1.1), so artificial cilia would naturally be useful for the creation of micro-pumps and micro-mixers. Pumping is still mostly done using macroscopic, external pumps. Although many designs for micro-pumps have been presented [53, 91], the use of multiple artificial cilia is new. The convincing proof of concept found in nature shows its potential.

Mixing needs special attention in microfluidic devices. In macroscopic mixers, a stirrer usually induces turbulence to provide efficient mixing. On a microscopic scale, however, this is much harder to achieve because of the low Reynolds number¹.

¹The ratio of inertial versus viscous forces is given by the dimensionless Reynolds number $Re = \frac{v_s L}{\nu}$, with v_s the mean fluid velocity, ν the kinematic viscosity, and L the characteristic length scale. When the length scale decreases

In this situation, mixing only happens by diffusion. To achieve any reasonable mixing speed, chaotic advection is required to increase the contact area of the constituents. This mixing can be achieved by artificial cilia, as has been shown by nature.

The details of how cilia movement exactly induces pumping and mixing is important for such behaviour in artificial cilia, and has been researched in theory and practise, e.g. [82, 97]. But this work confines itself to showing the feasibility of creating artificial cilia and actuating them; then comes the application to microfluidic systems, which is outside the scope of this work.

1.4 Approach

To use artificial cilia as actuators in microfluidics, one has to be able to build them and make them move. One of the methods to induce motion is by magnetism: a magnetic rod can be made to rotate or bend in the presence of a magnetic field. Compared with other mechanisms, like electric field, temperature or pH, magnetism has little influence on biochemical processes² [73]. The magnetic field can be created by an external (electro)magnet or integrated current wire. The latter would enable local control of the magnetic field, and possibly of the motion of single artificial cilia.

One can use magnetic actuation with two kinds of magnetic material: paramagnetic (induced magnetisation) and ferromagnetic (permanent magnetisation). The former has been investigated before and has had some success [78, 90]. The use of a permanent magnetic moment in artificial cilia is a new idea that may improve performance. In this project, the use of a permanently magnetic material for actuation is investigated.

Since it is still a question if magnetic actuation is feasible, it is useful to start with a relatively soft material to require relatively little force to bend a cilium. The polymer polydimethylsiloxane

considerably as a result of miniaturisation, the Reynolds number naturally goes with it, so that viscous forces start to dominate and prevent turbulence. See [94, 80] for quantitative examples.

²Although there are magneto-tactic bacteria that are sensitive to the earth's low magnetic field, this is exception rather than rule.

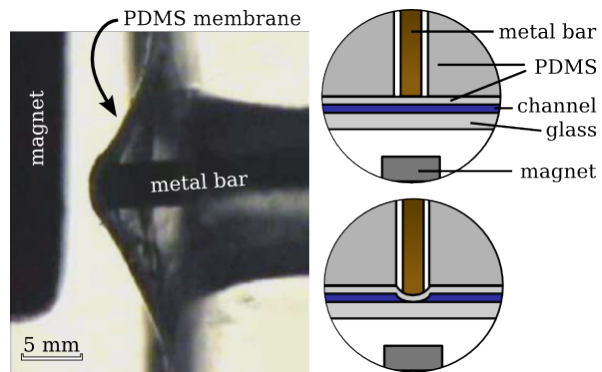


Figure 1.3: Magnetic valve with bar and magnet. [79]

(PDMS) has a Young's modulus of about a megapascal. It is widely used in microfluidic systems, easy to process and bio-compatible (see also section 2.3.2). While natural cilia have a much higher modulus, the lower modulus of PDMS makes it easier to induce movement. PDMS is not magnetic in itself, but it can be made so by doping it with magnetic particles.

Cilia in nature are cylindrical rods, standing upright. Their high aspect-ratio enables them to have large movements and to penetrate the fluid over some distance. Both increase the effect they have on the surrounding fluid. In analogy with this, it is desirable to have artificial cilia with a high aspect-ratio. This has not been easy to attain with PDMS, however, where an aspect-ratio of fifteen is considered high already [43, 86]. Therefore, another approach was taken: horizontal instead of vertically standing. The use of a sacrificial layer lift-off technique overcomes the difficulty of obtaining a high aspect-ratio inherent in production processes like replication-molding and lithography.

1.5 Related work

This section summarises existing publications that are closely related to artificial cilia and magnetically actuated microfluidic systems.

1.5.1 Magnetic micro-actuators

Magnetism and microfluidics have only been combined at large recently. In the last couple of years, various micro-valves and micro-pumps have ap-

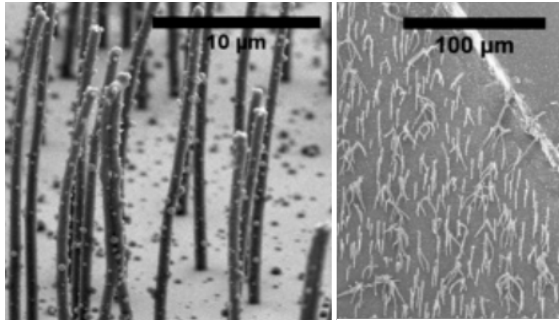


Figure 1.4: Artificial cilia that can bend under influence of a magnetic field [78].

peared where a piece of magnetic material is attracted to a magnet with a micro-channel in between (figure 1.3). The typical dimensions of this kind of device are in the order of millimetres. [66, 79, 92]

Not only have pieces of metal or magnets been embedded into PDMS, also magnetic powders have been mixed with PDMS to create a composite magnetic polymer. Magnetic membranes were used to create micro-valves[40] or -pumps[57, 67, 69]. Ground rare-earth magnets were mixed with PDMS to create millimetre-sized membranes deflected by an external (electro)magnet, or micrometre-sized iron particles were used. The rare-earth particles had sizes of tenths of millimetres and could be mixed with PDMS in concentrations of 50wt% (percentage in weight). Iron particles were $< 10\mu\text{m}$ and could be mixed with PDMS up to concentrations of 75wt% = 11vol%.

Deflection of a copper cantilever with a PDMS composite magnet has also been demonstrated [29]. In other work, there are efforts to incorporate superparamagnetic particles into PDMS at concentrations of 5vol% [78, 90].

1.5.2 Artificial cilia in microfluidics

There has been some previous work on artificial cilia in microfluidics. Arrays of microposts of plain PDMS of $30\mu\text{m}$ wide and $570\mu\text{m}$ high were created, suitable (for non-motile) flow-sensing cilia by optical detection [64]. Artificial cilia of down to 200nm in diameter and up to $25\mu\text{m}$ high, created of superparamagnetic particles in a PDMS matrix, have been shown to move under influence of a magnetic

field [78] (figure 1.4). Superparamagnetic slabs deflected by the magnetic gradient field of current wires are work in progress [81, 90]. Electrostatically actuated artificial cilia, fabricated horizontally, have been shown to induce mixing [94].

1.6 Thesis overview

This report describes the effort to show the feasibility of creating artificial cilia using a permanently magnetic PDMS composite in a horizontal fashion, that can be bent by a magnetic field. First, the idea is worked out in chapter 2, including a theoretical analysis. Then the creation process of the magnetic PDMS composite and its characterisation are treated in chapter 3. The fabrication of the half-suspended beam in PDMS using a sacrificial layer lift-off technique is described in chapter 4, after which the resulting feasibility prototype is investigated in chapter 5. A recapitulation of results and conclusions, as well as suggestions for future work is given in the final chapter 6.

Chapter 2

Design

2.1 Introduction

Before moving on to the production of an artificial cilium, it is worthwhile to have an idea of its expected behaviour. This results in an understanding of the relevant parameters involved and aids in choosing materials and design. As a starting point, we take a ferromagnetic PDMS composite to create horizontal beams, supported at one side (see figure 2.1). These are made to bend by application of a magnetic field. For comparison with the existing effort of a paramagnetic artificial cilium, an induced magnetic material (paramagnetic) is also analysed in this chapter.

2.2 An engineer's theory

To get an idea of the behaviour of a magnetic artificial cilium under application of a magnetic field, a basic order-of-magnitude calculation has been done. Goal is to find out what conditions are required to induce movement in an artificial cilium, and for this it suffices to make an approximation. The result is verified with a finite element simulation (section 2.4). A summary of the resulting formulae is given in table 2.1 on page 17, which are derived below.

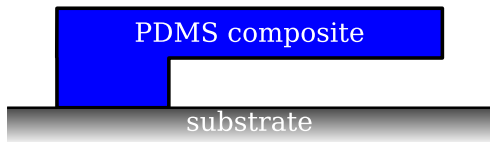


Figure 2.1: The proposed design for an artificial cilium: a horizontal half-suspended beam.

2.2.1 Force

Consider the interaction of the magnetic moment of an artificial cilium with a magnetic field. The cilium is taken as a single, solid block on which a force and torque may act as a result of an average field. It has length L , width W and thickness T , as shown in figure 2.2. When the cilium has a moment $\vec{\mu}$, it experiences a force

$$\vec{F} = \mu_0 (\vec{\mu} \cdot \nabla) \vec{H}_0, \quad (2.1)$$

where μ_0 is the permeability of vacuum, and \vec{H}_0 the applied magnetic field¹. In words: the force is proportional to the magnetic moment, and to the gradient of the field in the direction of the magnetic moment. This relation applies directly to a permanently magnetic cilium, with $\vec{\mu} = \vec{M}V$, where \vec{M} is the volume magnetisation, and V the volume of the magnetic material.

When the cilium's material is paramagnetic, the magnetic moment is induced by the externally applied magnetic field \vec{H}_0 : $\vec{\mu} = \vec{M}V = \chi \vec{H}_0 V$, with χ the magnetic susceptibility. Subsequently, the moment is always parallel to the field². The force

¹ \vec{H}_0 is the magnetic field as created by an external source (magnet). The presence of a magnetic moment alters the actual field, but \vec{H}_0 indicates the field in absence of the cilium.

² χ is a scalar. But when anisotropy is present, there is a different susceptibility in different directions and it becomes a tensor. In case of a long beam, there is a significant shape anisotropy. However, if the field remains parallel to the beam, it can be neglected. For an induced moment and small deflections (as will be explained shortly), this is the case anyway. See section 2.2.3 for a further treatment of anisotropy.

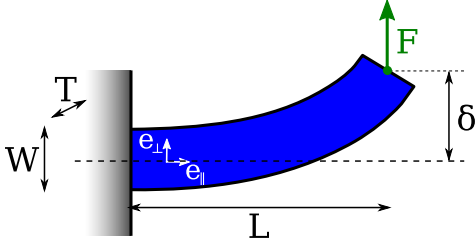


Figure 2.2: A half-suspended beam deflects over a distance δ under the influence of a force F exerted on its free end. The beam has a length L , width W , and thickness T (out of plane). This only holds for small deflections, so the length of the deflected beam is equal to the length of the bent beam.

becomes

$$\vec{F} = \mu_0 \chi V \left(\vec{H}_0 \cdot \nabla \right) \vec{H}_0. \quad (2.2)$$

In words: the force is proportional to the susceptibility of the cilium, to the field, and to the gradient of the field in the direction of the field.

Since the cilium is fixed at one side, a perpendicular force makes it bend. For small displacements, this is described by standard beam deflection theory³. The deflection δ of a half-suspended beam with Young's modulus E that is loaded at its free end with a force F is [12, 15]

$$\delta = \frac{4L^3 F}{ETW^3}. \quad (2.3)$$

Since $\delta \propto L^3$, the end of the beam contributes most to the deflection, even though the whole beam experiences a magnetic force⁴. In analogy with [90], we take an area of $W \times W \times T$ at the tip. The force F is acting in a direction \vec{e}_\perp perpendicular to the

³The assumptions are that the material is homogeneous, the radius of curvature $\geq 10W$, the force is perpendicular to the beam's axis, $L \gg W$, and the material behaves as a Hookean solid.

⁴In case of a current wire perpendicular to the plane of paper, the gradient is far from homogeneous over the beam. Since the end contributes most to the deflection, it is positioned most favourably close to it. This makes only the end contribute significantly.

beam⁵,

$$\delta = \frac{4\mu_0 L^3}{EW} \left[\left(\vec{M} \cdot \nabla \right) \vec{H}_0 \right] \cdot \vec{e}_\perp. \quad (2.4)$$

For an induced magnetic moment, this becomes

$$\delta = \frac{4\mu_0 \chi L^3}{EW} \left[\left(\vec{H}_0 \cdot \nabla \right) \vec{H}_0 \right] \cdot \vec{e}_\perp. \quad (2.5)$$

2.2.2 Torque

The force is caused by the gradient of the magnetic field. But there is also a torque, induced by a non-parallel magnetic moment: $\vec{\tau} = \mu_0 \vec{\mu} \times \vec{H}_0$. When the fixed end of the beam is taken as a rotation point⁶, the effect of the torque is the same as that of a force F at the free end:

$$\begin{aligned} \vec{\tau} &= \mu_0 \vec{\mu} \times \vec{H}_0 = L \vec{e}_\parallel \times \vec{F} \\ \Rightarrow F &= \frac{\mu_0}{L} \left(\vec{\mu} \times \vec{H}_0 \right) \cdot \vec{e}_z, \end{aligned} \quad (2.6)$$

where \vec{e}_\parallel is the unit vector parallel to the beam, and $\vec{e}_z = \vec{e}_\parallel \times \vec{e}_\perp$. Again, this only holds for small deflections, when F is perpendicular to the beam.

Now that the torque is translated into a force acting on the end of the beam, it can be applied to the deformation problem:

$$\delta = \frac{4\mu_0 L^3}{EW^2} \left(\vec{M} \times \vec{H}_0 \right) \cdot \vec{e}_z. \quad (2.7)$$

There is only a deflection if the magnetic moment and field are not parallel. In case of an induced moment, $\vec{\mu} \propto \vec{H}_0$, and the torque and deflection are zero.

2.2.3 Anisotropy

As already mentioned in footnote 2 on the previous page, the induced magnetisation of a beam may not be completely parallel to the field. This is due to

⁵The working point of the force in equation 2.3 is at the end, while it is at the centre of the $W \times W \times T$ block for the magnetic force in equations 2.4 and 2.5. But since $L \gg W$, the difference is negligible in this order-of-magnitude calculation.

⁶The beam is far from being a solid block; equation 2.3 explicitly uses the deformability. But to avoid a more complex treatment of the problem, the magnetic torque is taken as working on an undeformable block; to verify this and other approximations, the result is tested with a finite element simulation in section 2.4.

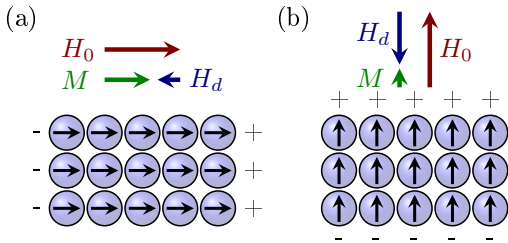


Figure 2.3: The demagnetising field H_d can be thought of as induced by free magnetic poles at the surface (indicated by + and -). A thin layer exhibits two extreme cases: (a) the field is parallel, leading to $\mathcal{N} \rightarrow 0$, whereas (b) for a perpendicular field, $\mathcal{N} \rightarrow 1$. The depicted material has a susceptibility χ slightly smaller than one, since $M = \chi H_i$, and $H_i = H_0 + H_d$, with $H_d < 0$.

anisotropy and the demagnetising field, which will be explained shortly. For a more thorough treatment, please refer to [42, §3] and standard textbooks on magnetism.

When a material is magnetised, magnetic poles are formed at the ends, creating a field opposite to the magnetisation. This is the demagnetising field H_d , which reduces the internal field H_i with respect to the external field H_0 : $H_i = H_0 + H_d$. Since H_d is directly a result of the magnetisation of the material, it is defined as $H_d = -\mathcal{N}M$, with \mathcal{N} the demagnetisation factor.

For a very thin specimen with a perpendicular magnetisation, the number of magnetic poles on the surface is large with respect to the volume of the sample (figure 2.3b). This results in a large demagnetisation factor⁷: $\mathcal{N}_\perp \rightarrow 1$. When the magnetisation of the same sample is parallel, the demagnetisation factor becomes (almost) zero (figure 2.3a): $\mathcal{N}_\parallel \rightarrow 0$. For other shapes than thin layers, the demagnetisation factor is between zero and one, and $\mathcal{N}_\parallel + \mathcal{N}_\perp = 1$ holds. This generalises in three dimensions to $\mathcal{N}_x + \mathcal{N}_y + \mathcal{N}_z = 1$.

Only for ellipsoids and infinitely long, thin plates

⁷ It is actually not magnetic poles that cause demagnetisation directly. Magnetic poles cause the magnetic moments at the surface to orient themselves parallel to the surface, which causes an amount of flux closure that lowers the stray field. This is not always explained clearly, though [50] touches upon it in chapter 3. An important consequence is, that in a saturated sample even the moments at the surface orient themselves to the external field, and no demagnetisation is present.

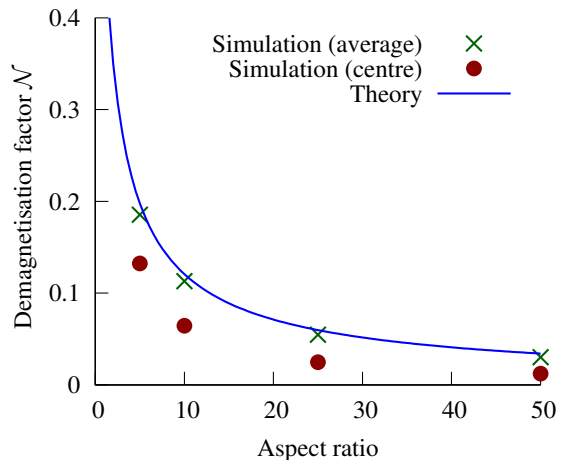


Figure 2.4: The long axis demagnetisation factor \mathcal{N}_\parallel of a two-dimensional rectangular prism as a function of aspect ratio $p = \frac{L}{W}$. The short axis demagnetisation factor naturally is $\mathcal{N}_\perp = 1 - \mathcal{N}_\parallel$. The solid line is according to the formula given by [23], while points are results of finite element simulations of a box in a homogeneous field. The red circles are a result of the demagnetising field at the centre of the box, while the green crosses are averaged over the whole body. This shows that the demagnetising field of a rectangular prism is indeed not homogeneous. The theory describes the average demagnetisation field over the whole box, which is useful for the current analysis that approaches the cilium as a single, homogeneous body.

the demagnetising field is homogeneous throughout the shape, resulting in manageable analytic expressions [1]. A sphere is completely symmetric in all three dimensions, so $\mathcal{N} = \frac{1}{3}$. The demagnetising field in cylinders and rectangular prisms varies over the shape, but it is possible to define an effective demagnetisation factor [17, 23]. The latter is shown in figure 2.4 for a two-dimensional prism ($\mathcal{N}_z \rightarrow 0$).

For a paramagnetic material, the magnetisation is dependent on the external field, and so is the demagnetising field. Subsequently, the total magnetic response of the material is dependent on \mathcal{N} . This results in an effective susceptibility χ_{eff} that depends on the shape, and the “clean” susceptibility χ with no demagnetising field present. To quantify, the effective susceptibility is derived:

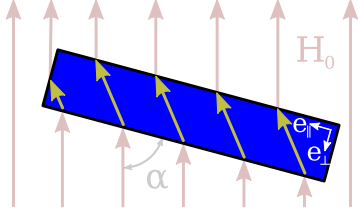


Figure 2.5: Anisotropy can cause a non-parallel magnetisation in a paramagnetic material. The external magnetic field H_0 is at an angle α with the beam's long axis \vec{e}_{\parallel} . The susceptibility of the beam is different in both directions due to shape anisotropy, so its magnetisation is not parallel with H_0 . The resulting internal field H_i is shown with arrows inside the material.

$$\begin{aligned} M &= \chi H_i = \chi (H_0 - \mathcal{N}M) \\ &= \frac{\chi}{1 + \mathcal{N}\chi} H_0 \Rightarrow \chi_{\text{eff}} = \frac{\chi}{1 + \mathcal{N}\chi}. \end{aligned} \quad (2.8)$$

The “clean” susceptibility χ can be measured in a sample with $\mathcal{N} \rightarrow 0$ in the correct direction. In that case $\chi_{\text{eff}} \rightarrow \chi$.

An asymmetric shape has different demagnetisation factors in different directions, so the demagnetisation factor and effective susceptibility χ_{eff} is different for different directions. This can be the cause of non-parallelism between the induced magnetic moment and the external field. In case of a two-dimensional beam ($T \rightarrow \infty$), the demagnetisation factor \mathcal{N}_{\parallel} soon is smaller than 0.1 for aspect ratios over ten, as can be seen in figure 2.4, so that there is an order difference between the parallel and perpendicular demagnetisation factors. This can create an induced moment that is not parallel to the external field, so that there is a magnetic torque in a cilium with a magnetically induced moment.

The magnitude of this effect can be quantified by considering a paramagnetic block with susceptibility χ in a magnetic field H_0 with the unit vector \vec{e}_{\parallel} pointing along its long axis, and \vec{e}_{\perp} perpendicular to it. The angle between the magnetic field and \vec{e}_{\parallel} is α . This is depicted in figure 2.5. The magnetisation along these directions is $M_{\parallel} = \chi_{\parallel} H_0 \cos \alpha$ and $M_{\perp} = \chi_{\perp} H_0 \sin \alpha$. The induced torque then

becomes

$$\begin{aligned} \vec{\tau} &= \mu_0 \vec{\mu} \times \vec{H}_0 = \mu_0 V \vec{M} \times \vec{H}_0 \\ &= \mu_0 V (\chi_{\parallel} H_0 \cos \alpha \vec{e}_{\parallel} + \chi_{\perp} H_0 \sin \alpha \vec{e}_{\perp}) \times \vec{H}_0 \\ &= \frac{1}{2} \mu_0 V |\vec{H}_0|^2 \sin 2\alpha (\chi_{\parallel} - \chi_{\perp}) \vec{e}_z, \end{aligned} \quad (2.9)$$

with χ_{\parallel} the effective susceptibility in the direction parallel to the block's long axis, and χ_{\perp} the effective susceptibility along its perpendicular axis. Their difference is a result of demagnetisation, expressed by equation 2.8. When $\chi < 1$, it can be shown that the torque is limited to

$$\begin{aligned} |\vec{\tau}| &< \frac{1}{2} \mu_0 V \chi^2 |\vec{H}_0|^2 |\sin 2\alpha| (2\mathcal{N}_{\perp} - 1) \\ &< \frac{1}{2} \mu_0 V \chi^2 |\vec{H}_0|^2 |\sin 2\alpha|, \end{aligned} \quad (2.10)$$

and, using equations 2.3 and 2.6, the resulting deflection

$$\begin{aligned} \delta_{i,\tau} &< \frac{2\mu_0 L^3}{EW^2} \chi^2 |\vec{H}_0|^2 |\sin 2\alpha| (2\mathcal{N}_{\perp} - 1) \\ &< \frac{2\mu_0 L^3}{EW^2} \chi^2 |\vec{H}_0|^2 |\sin 2\alpha|, \end{aligned} \quad (2.11)$$

When comparing this with the deflection caused by a parallel induced moment (formula 2.5), it becomes clear that in the field of a current wire (see section 2.3.1.1 and table 2.1)

$$\frac{\delta_i}{\delta_{i,\tau}} = \frac{2W}{\chi R |\sin 2\alpha|}, \quad (2.12)$$

and a large susceptibility is needed if the induced torque is to be of any significant influence (R is in the same order as W , as explained in section 2.3.1.1).

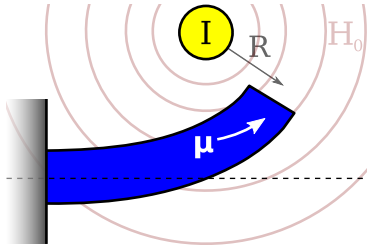
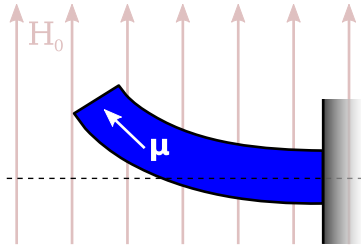
	<i>induced</i> paramagnetic	<i>permanent</i> ferromagnetic
	$\vec{\mu}$ is parallel to \vec{H}_0	$\vec{\mu}$ is parallel to the cilium's long axis $\vec{e}_{ }$
	$\vec{F} = \mu_0 (\vec{\mu} \cdot \nabla) \vec{H}_0$	$\vec{F}_i = \mu_0 \chi T W^2 (\vec{H}_0 \cdot \nabla) \vec{H}_0$
	$\vec{\tau} = \mu_0 \vec{\mu} \times \vec{H}_0$	$\vec{\tau}_i = 0$
	$\vec{\tau}_p = \mu_0 T W L \vec{M} \times \vec{H}_0$	$\vec{F}_p = \mu_0 T W^2 (\vec{M} \cdot \nabla) \vec{H}_0$
	$\frac{\delta}{W} = \frac{4L^2}{ETW^4} (L\vec{F} \cdot \vec{e}_{\perp} + \vec{\tau} \cdot \vec{e}_z)$	$\frac{\delta_i}{W} = \frac{4\mu_0 \chi L^3}{EW^2} [(\vec{H}_0 \cdot \nabla) \vec{H}_0] \cdot \vec{e}_{\perp}$
	$\frac{\delta_p}{W} = \frac{4\mu_0 L^3}{EW^3} \left\{ W [(\vec{M} \cdot \nabla) \vec{H}_0] \cdot \vec{e}_{\perp} + (\vec{M} \times \vec{H}_0) \cdot \vec{e}_z \right\}$	
	magnetic field of a current wire	homogeneous magnetic field by (electro)magnet
		
	$H_0 = \frac{I}{2\pi R}, \nabla H_0 = \frac{I}{2\pi R^2}$	$H_0 = H_{0,magnet}, \nabla H_0 = 0$
maximum deflection	$\frac{\delta_i}{W} = \frac{\mu_0 \chi L^3 I^2}{EW^2 \pi^2 R^3}$	$\frac{\delta_p}{W} = \frac{4\mu_0 L^3 M H_0}{EW^3}$

Table 2.1: Comparison of induced (subscript i) and permanently (subscript p) magnetic behaviour. The first part discusses the general relations for the force \vec{F} and torque $\vec{\tau}$ on a half-suspended beam in a magnetic field, and the resulting deflection δ as discussed in section 2.2. The bottom part treats a specific magnetic field and applies it to the deflection. For the induced moment, a field with a large gradient is useful: that of a current wire with current I and distance R from the centre of the beam. For the permanently magnetic material, a large field perpendicular to the beam is more appropriate. The “maximum deflection” discards the vector character and is valid when the angle between field and beam is optimal. Please refer to the text for an explanation of the other symbols used.

2.3 Exploring the parameters

Now that the basic theory is known, it is useful to look at the parameters involved and what can be expected of them in practise. Upper and lower bounds are identified, enabling a prediction of the deflection in section 2.4. The results of this section are summarised in table 2.3.

2.3.1 Magnetic field

As discussed before, deflection is dependent on the field magnitude. Only for an induced moment parallel to the beam, the field gradient is additionally important. Because of this difference between the induced and permanent moment, they will be treated separately.

2.3.1.1 Current wire

To achieve a high gradient for the cilium with an induced magnetic moment, a current wire has been used before [90] and will be taken as reference. A current wire placed at the origin induces a magnetic field and gradient of

$$\vec{H}_{wire} = \frac{I}{2\pi R} \vec{e}_\phi, \quad \nabla \vec{H}_0 = -\frac{I}{2\pi R^2} \vec{e}_r, \quad (2.13)$$

with I the current perpendicular to the 2D-plane of the beam (going into the paper of the figure “induced” in table 2.1), and R the distance between the centres of wire and cilium tip.

The upper limit to the magnetic field is determined by two factors: heat dissipation in the wire and available power. Heat dissipation is due to the non-zero resistance of a current wire. The maximum current density strongly depends on heat management details, but an upper limit can be set by considering electromigration. This phenomenon destroys the wire within an hour if the current density j is in the order of $10^{11} A/m^2$ [10, 90]. Small wires may suffer from this, larger wires are limited by a practical upper limit on the current. In a laboratory, tens of amperes can be achieved; in a handheld device, this is rather like hundreds of milliamperes. When a low duty cycle is used, up to several amperes are possible. A maximum current of $5A$ will be used as upper bound.

The distance between current wire and cilium should be as small as possible, since both field and

gradient decrease with increasing distance. The distance between the centres of the current wire and cilium tip is R . There must be some space for deflection, so a distance of three times the width W of the cilium is a sensible minimum. This would give room for a deflection of $\frac{3}{2}W$, and a wire radius of W .

2.3.1.2 Magnet

For a cilium with a permanent moment, a field perpendicular to it is needed. This is best achieved using an external (electro)magnet. Nowadays’ rare-earth magnets are small (millimetres) and can have a remanent field of a bit more than a Tesla. At a working distance of a millimetre from the pole, it is about half a Tesla.

For a switchable field, an electromagnet is preferable. Though large electromagnets can produce fields of several Tesla, they are too bulky for use in microfluidic systems. Smaller electromagnets can produce fields in the order of $100mT$ with currents of amperes. This is possible even on a microscopic scale [41].

2.3.2 Material

As discussed in section 1.4, polydimethylsiloxane (PDMS) was chosen as material. It has a low Young’s modulus E , which makes it easy to deform (equation 2.3). This polymer is widely used in microfluidics and is readily available at low cost⁸. It is bio-compatible[39], which is beneficial for use in biochemical devices⁹. Also does it seal against leakage [38].

PDMS consists of long chains of the monomer $\text{SiO}(\text{CH}_3)_2$. It is supplied in a liquid (visco-elastic) state. After it is cast into the desired shape, links are created between the chains, and it becomes a solid¹⁰. Depending on the amount of links, the resulting material can have a Young’s modulus ranging from about 0.5 to 5 megapascal [25]. Since the deflection is inversely related to the modulus, a value of 0.5MPa is used for the current discussion.

⁸Sylgard-184 is available for less than €0.15 per gram.

⁹In fact, PDMS can also be present in food as anti-foaming or anti-caking agent. In this area, it is usually known as E900.

¹⁰How this cross-linking is performed will be explained in section 3.1.

2.3.3 Dimensions

A typical micro-channel is tenths of millimetres wide and tens of micrometres high. Components like valves are often in the millimetre range (see section 1.5.1 and [71]). For a complex lab-on-a-chip containing many components, this is still rather large. One millimetre will be taken as upper limit for application as a microfluidic element.

A lower limit is set, in a practical way, by the structuring of PDMS. It is possible to reach a resolution of 100nm [36, 60], but most methods are in the micrometre-range. This sets a limit on the size of the cilia that can be produced, which must be at least a couple of times the resolution. The horizontal fabrication of a cilium makes it possible to create one with a low thickness W down to the sub-micrometre range. This would enable high aspect-ratio's $p = L/W$ for small structures. It may be useful to note that nanofluidic effects begin to play a role at dimensions below a micrometre, changing the interaction between the fluid and cilia.

All in all, the thickness will be taken to be between $0.1\mu\text{m}$ and 1mm , and the length between $1\mu\text{m}$ and 1mm .

2.3.4 Magnetic composite

Finally, the magnetic response of the cilium is important. To make PDMS magnetic, it is doped with magnetic particles. This should be possible to concentrations of up to 5 or 11 vol% (see section 1.5.1). The exact attainable concentration depends on the interaction between polymer and particle material, and details of chemical processes (particles may pollute parts of the cross-linking process). It can be tuned by using a surfactant. When assuming that doping permanently magnetic particles into PDMS is similar to previous work, a maximum concentration of 5vol% is a safe assumption. The magnetisation M is the magnetic moment per unit of volume, so the magnetisation of the composite is $M_{\text{composite}} = \frac{\text{vol}\%}{100\%} \cdot M_{\text{particles}}$.

While small particles are beneficial for dispersion, homogeneity, mechanical stability and allow the fabrication of small structures (the cilium must be a couple of times bigger than the particles), there is a lower limit on their size. When permanently magnetic particles shrink, the magnetic behaviour changes at some point, and finally they become su-

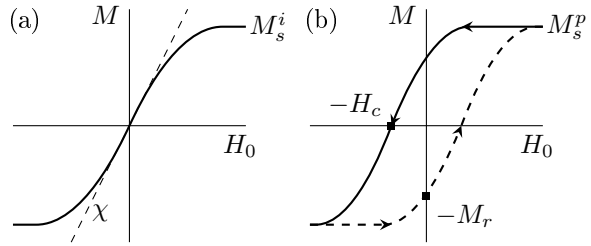


Figure 2.6: Magnetisation curves for (a) paramagnetic and (b) permanently magnetic materials. It shows how a magnetic material responds to an applied magnetic field H_0 by changing its magnetisation M . The saturation magnetisation M_s (indicated by M_s^i for the induced paramagnetic material, and M_s^p for the permanent ferromagnetic material), susceptibility χ , coercive field H_c , and remanent magnetisation M_r are indicated. Note that the magnetisation curves are symmetric, and H_c and M_r are defined as positive quantities.

perparamagnetic. This is explained in appendix A. For the current discussion, it is assumed that particles are large enough to show the same permanently magnetic behaviour as bulk, and small enough to be able to approach the composite as a homogeneous material.

Paramagnetic substances align their moment to an externally applied magnetic field, thereby contributing to the total field. Permanently magnetic materials keep their orientation until the external field exceeds the barrier H_c , after which their magnetic moment is aligned too. Figure 2.6 shows the magnetisation curves for both situations. The relation between the material's magnetisation and the external field is determined by its susceptibility χ ; it is defined by $M = \chi H_0$. At high fields, however, the magnetisation is saturated and reaches the saturation magnetisation M_s .

A paramagnetic material has zero magnetisation when there is no external field, but a permanently magnetic material has a remanent magnetisation M_r . It can be seen in figure 2.6b, that there is hysteresis: the remanent magnetisation can be either positive or negative. This depends on the direction in which the curve is traversed. Consider a large field that is applied so that $M = M_s^p$ (top right in figure 2.6b). Then the external field decreases to zero, at which point a remanent magnetisation remains: $M = M_r$. When the field becomes negative, the magnetisation remains positive

(units MA/m)	M_s	M_r	H_c	ref
Fe	1.71	1.11		[6]
Co	1.42	0.39		[6]
Nd ₂ Fe ₁₄ B	1.23	1.02	0.90	[28, 84]
SmCo ₅	0.76	0.70	0.66	[28, 84]

Table 2.2: Bulk magnetic properties of some permanently magnetic materials. Iron, cobalt and nickel are generally used as high-permeability materials and are produced with a very low coercive field. Note that the coercive field varies greatly across sources, since it greatly depends on production details.

until $H_0 = -H_c$: at the coercive field the permanent magnetisation breaks down and follows the field to saturation (bottom left). So if the material should keep its magnetic orientation, an external field should remain lower than the coercive field. Only the very first time (or after demagnetisation), the material may have zero magnetisation at zero field; this is not shown in the magnetisation curve. In that situation, different magnetic moments inside the material may cancel each other. When a field is applied, these moments align and remain aligned when the field is removed again. So a permanently magnetic material must first be magnetised to show remanence.

When a paramagnetic material is used in a cilium, it is desirable to have a high susceptibility. The material for a permanently magnetic cilium should have a high remanent field and a coercive field higher than that of the actuating external field. In both cases, a high saturation magnetisation is beneficial.

As a paramagnetic material, superparamagnetic magnetite (Fe₃O₄) nanoparticles have been used before, which have a saturation magnetisation of 0.49MA/m (see table A.2 on page 63). Its susceptibility depends on the particle size, as it is superparamagnetic¹¹. For particles with a diameter of 10nm, the equivalent bulk susceptibility has been measured to be around 16 [90].

Permanently magnetic materials can be found in

¹¹This is touched upon in section A.3. Because a superparamagnetic particle is free to take any orientation, every magnetic moment present will align itself with the field on average. The particle's diameter determines its response, and subsequently its susceptibility.

ferromagnets. Iron, cobalt and nickel are classical examples. Of these, iron has the highest saturation magnetisation, which is 1.7MA/m. Since iron is used as high-permeability material, it usually has a coercive field in the order of 100A/m¹², which is 0.1mT¹³. Rare-earth magnets have a similar saturation magnetisation but much higher coercive fields¹⁴. See table 2.2 for an overview.

Because production details are so important for the resulting magnetic properties (except saturation magnetisation), it is worthwhile to look at characteristics of ferromagnetic nanoparticles, since these will need to be used. Rare-earth magnetic nanoparticles are not readily available, so metals remain. Carbon encapsulated nanoparticles of iron, cobalt and nickel of about 18nm are reported to have a remanent magnetisation of $\frac{1}{3}$ of the saturation magnetisation; the coercive field for iron and cobalt is about 50kA/m, which amounts to 70mT [37]. Although this kind of particles is still the subject of research, they are becoming available commercially.

¹²[6] mentions an iron sample with a coercive field of 159kA/mm, but such a high H_c may be hard to find elsewhere.

¹³In the SI system of units, $B = \mu_0(H + M)$, with B the magnetic induction (which can be called magnetic field too) and $\mu_0 = 4\pi \cdot 10^{-7}$. When considering a permanent magnet with no external field, $H = 0$ and so $B = \mu_0 M$. Though the unit of B is Tesla (T) and that of H is Ampere per metre (A/m), it is possible to use these units interchangeably with a conversion factor of $1\text{T} = \mu_0 \text{A/m}$. So the magnetisation as well as the magnetic field (using $B = \mu_0 H$) can be expressed in Tesla.

¹⁴Two types of coercive field may be mentioned in literature: flux coercivity and intrinsic coercivity. To understand the difference, consider a magnetised material in an opposing external field. The strength of the external field needed to force the magnet's magnetisation to zero is called the flux coercivity. When the external field is subsequently removed, the permanent magnet will have the same magnetisation as before. But when a larger opposing external field is applied, the magnetisation is reversed and becomes parallel to the external field. The field needed for this is the intrinsic coercivity. This is explained in more detail in [85]. The relevant coercivity here is the flux coercivity, since at that external field strength the material's magnetisation becomes zero.

		<i>min</i>	<i>actual</i>	<i>max</i>	<i>units</i>	
Young's modulus	E	0.5	0.5	5	MPa	
Thickness	W	0.1	...	1000	μm	
Length	L	1	...	1000	μm	
vol% particles in PDMS	vol%	0	5	10	vol%	
<i>induced paramagnetic moment:</i>						
Current	I	0	...	5	A	
Current density	j	0	...	10^{11}	A/m^2	$I = j\pi r^2$
Wire radius	r		= W			
Distance wire - cilium	R		= $3W$			
Susceptibility	χ		16			
Saturation magnetisation	M_s^i		615		mT	
<i>permanent ferromagnetic moment:</i>						
External magnet's field	H_0	0	...	100	mT	
Coercive field	H_c		70		mT	$H_0 < H_c$
Saturation magnetisation	M_s^p		1471		mT	
Remanent field	M_r		490		mT	= $\frac{1}{3}M_s$

Table 2.3: The relevant parameters and their bounds as identified in section 2.3. Minimum (min) and maximum (max) values are shown. Actual choices made for some parameters (actual) are shown, with “...” to indicate that the parameter is varied in the discussion in section 2.4. Magnetic properties that depend on volume (χ , M_s and M_r) are specified for the magnetic particles and need to be multiplied by the particle concentration (vol%) to obtain the magnetic properties of the composite.

2.4 Expected order of magnitude

Now that both the theory and parameters have been explored, they can be put together to make an estimation of the expected behaviour. This order-of-magnitude calculation serves as a tool for choosing parameter values, and is verified by numerical simulations. Note that the theory is only an approximation that is valid for small deflections. As such it gives insight into the onset of movement, and helps determining if movement is possible at all, or not. What happens when the deflection of a cilium exceeds a couple of its widths, is not possible to say without modifications to the theory presented.

The deflection δ_p caused by a permanent moment has been derived in equation 2.7. When the field is perpendicular to the cilium, it can be written in scalar notation as follows

$$\frac{\delta_p}{W} = \frac{4\mu_0 L^3 M H_0}{E W^3}. \quad (2.14)$$

Note that for a permanently magnetic material that has been magnetised, $M = M_r$. The deflection δ_i of an induced moment because of a current wire is obtained by combining equations 2.5 and 2.13. When assuming that the magnetic field is parallel to the cilium, the gradient is perpendicular. The total deflection becomes

$$\frac{\delta_i}{W} = \frac{\mu_0 \chi L^3 I^2}{E W^2 \pi^2 R^3}. \quad (2.15)$$

This is summarised in table 2.1 on page 17. The parameter space and its boundaries are summarised in table 2.3 on the preceding page. Figure 2.8 shows a graph of the deflection, for a certain choice of thickness $W = 10\mu\text{m}$ and length $L = 120\mu\text{m}$, as function of the actuating field. For the induced magnetic moment, this is a current; while for the permanently magnetic material, an external homogeneous field is used. Both the theoretical relation and results of simulations are shown.

The result of the simulation with $I = 3.5\text{A}$ is shown in more detail in figure 2.7. The black circle in the top centre of the plot is the current wire. The slab is almost touching it, having a deflection of about $\frac{3}{2}$ its width. When the current is increased, the cilium collides with the current wire, which is not accounted for in theory or simulations.

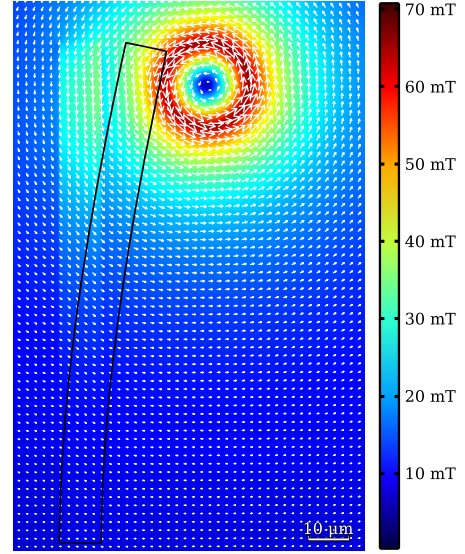


Figure 2.7: The result of a finite element simulation of an artificial cilium with induced magnetic moment having parameter values as specified in table 2.3 and $W = 10\mu\text{m}$, $L = 120\mu\text{m}$, $I = 3.5\text{A}$. The magnetic flux density is shown as surface and arrow plot. The deformed beam is drawn on top, showing a deflection of about $3/2$ times the width of the beam. Note that simulations do not take into account the change of field when it approaches the current wire.

Theory and simulation of the permanently magnetic and induced artificial cilium in figure 2.8 agree well for deflections up to two times the width. Above that, the cilium is bent considerably and the assumption that \vec{M} is perpendicular to \vec{H}_0 no longer holds, so the deflection is lower than predicted. Also the deflection formula 2.3 is not valid anymore.

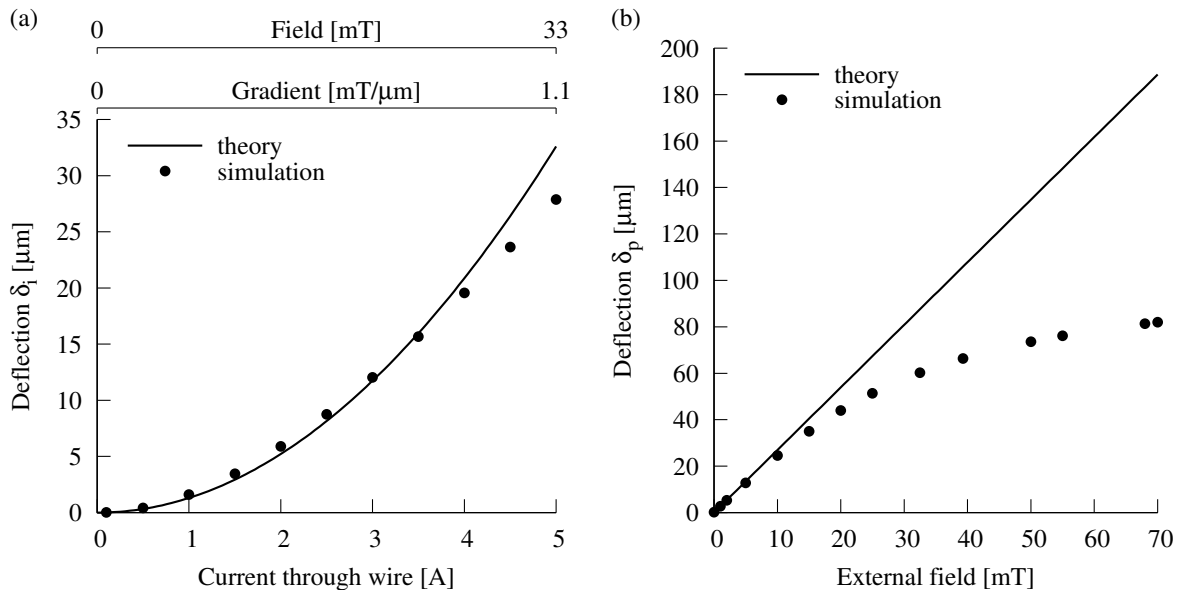


Figure 2.8: The deflection of an artificial cilium with (a) a magnetic induced moment actuated by a current wire, and (b) a permanently magnetic moment actuated by the homogeneous field of an external magnet. The cilium in question has parameter values as specified in table 2.3 with $W = 10\mu\text{m}$ and $L = 120\mu\text{m}$. In graph (a), the field and field gradient of the current wire at the cilium's tip are indicated on top, since they scale linearly with the current.

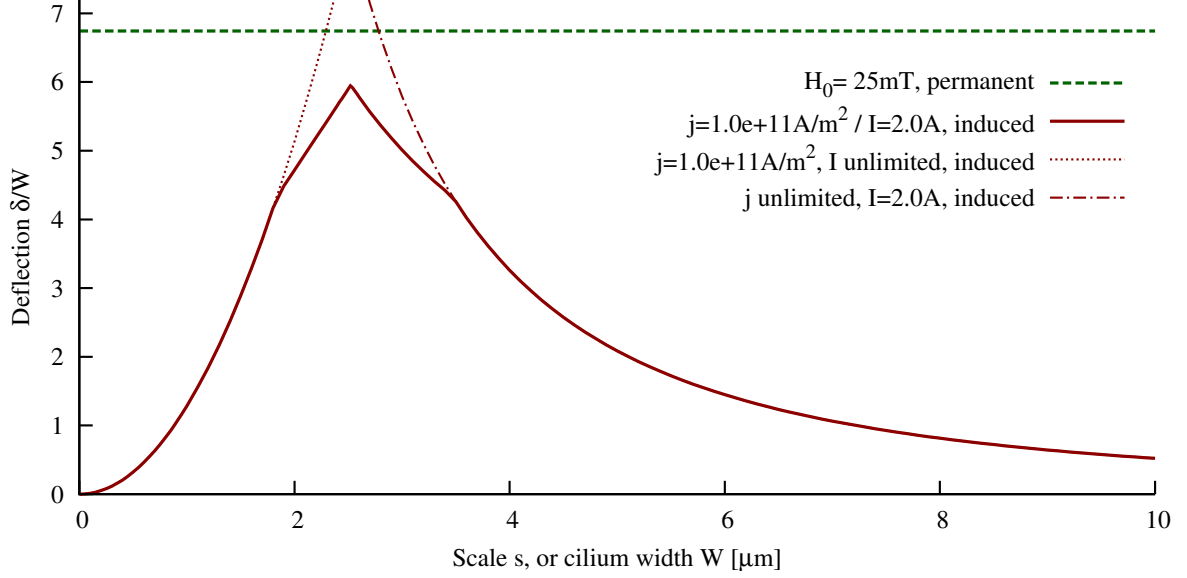


Figure 2.9: Deflection in terms of cilium width as a function of scale. At a scale of one, the cilium width is $W = 1\mu\text{m}$ and $L = 12\mu\text{m}$; at a scale of ten $W = 10\mu\text{m}$ and $L = 120\mu\text{m}$ (which would correspond to a point in figure 2.8a and 2.8b); etc. etc. Parameters not mentioned are according to table 2.3. The dashed, green, horizontal line is the deflection of a permanently magnetic cilium, which is clearly independent of scale. The other (red) lines are deflections of an induced cilium. For the dashed red lines, either the current is kept constant while scaling (right), or the current density (left). For these, limits to maximum current, current density, and magnetisation of the paramagnetic material have not been taken into account. When this is done, the solid red line is obtained. Note that H_0 and the upper current limit are a fraction of their maximum parameter value, so to obtain a concise graph. It is clear from figure 2.8 that the permanent deflection is indeed higher than the induced for H_0 and I at maximum parameter values.

2.4.1 Scaling behaviour

When scaling the complete system, the behaviour of a cilium with a permanent and induced magnetic moment is different. Equations 2.14 and 2.15 show the deflection in terms of cilium width, a scale-invariant measure of performance. The deflection for the permanently magnetic cilium scales with $\delta_p/W \propto (L/W)^3$ and is independent of system size. The deflection of the magnetically induced cilium scales with $\delta_i/W \propto L^3W^{-2}R^{-3}$. With s the amount by which every dimension is scaled, this can be expressed as $\delta_i/W \propto s^{-2}$ if the current I is kept constant. If the current density is kept constant instead, I increases with scale and $\delta_i/W \propto L^3r^4W^{-2}R^{-3} \propto s^2$. These relations are shown in figure 2.9 and summarised in table 2.4.

In reality though, there are limits to current and current density. There is also a maximum to the magnetisation of the paramagnetic material: $M = \chi H_0 \leq M_s^i$, with M_s^i the material's saturation magnetisation¹⁵. When these are taken into account, the solid red line is obtained, so that either the current is at its maximum ($s > 2.52$), or the current density ($s < 2.52$). Note that in this graph, H_0 and I were limited to a fraction of their maximum value. This gives a deflection in a range where the theory is still reasonably valid, and shows

¹⁵The current approach effectively models the Langevin curve (figure 2.6a) as a line with slope χ (dashed line in the aforementioned figure), capped by a horizontal line at $M = \pm M_s^i$. Simulations on induced cilia in this report were done with a magnetisation curve of the actual Fe_3O_4 -PDMS composite, measured with a VSM by the first author of [90].

a graph in which the interesting features are visible all together.

Looking at the deflection of the induced cilium (solid red line), one can see that the scaling behaviour of constant current density ($\delta_i/W \propto s^2$, dotted red line) is followed up to $s = 1.8$. There, the material's magnetisation $M = \chi H_0 = \frac{\chi j \pi r^2}{2\pi R} = 0.6\text{T} = M_s^i$ reaches its saturation. Because of that, the slope decreases an order in s and remains constant until $s = 2.5$, at which point the maximum current $I = j\pi r^2 = 2\text{A}$ is reached. When the scale is increased even more, the current density drops, while the distance between cilium and current wire increases, so the deflection decreases too. At $s = 3.5$, the magnetisation drops below saturation, and the behaviour of constant current to infinity ($\delta_i/W \propto s^{-2}$) is followed.

Besides scaling, there is a geometric dependence on aspect-ratio $p = L/W$. Since both the cilium with induced and permanent magnetic moment have an L^3 -dependence, they share their p^3 behaviour. This can also be recognised in table 2.4.

2.5 Conclusion

In this chapter, a theory has been presented which gives insight into the parameters affecting performance of magnetically actuated artificial cilia. It has been verified by numerical simulations. Boundaries for the relevant parameters have been identified, so that a reasonable expectation of feasibility could be made. And indeed, deflection of a magnetic artificial cilium is feasible, at least up to several times its width.

For a cilium with an induced magnetic moment, the size of the system has to be chosen carefully. A cilium with a permanently magnetic moment, deflected by a torque, however, behaves independently of its size. It also has, within the parameter range that was found reasonable, a deflection that is, at best, a couple of times larger than that of the induced cilium. Both issues favour the permanently magnetic cilium, and the remainder of this report is about creating and characterising exactly that.¹⁶

¹⁶Combining the mechanisms of an induced and permanently magnetic cilium would be possible when the scale is chosen optimally ($s = 2.5$ in figure 2.9). This is touched upon in section 6.2.

Permanently magnetic	$\frac{\delta_p}{W} \propto p^3 s^0 \cdot M_r^p H_0$
Induced, j fixed	$\frac{\delta_i}{W} \propto p^3 s^2 \cdot \chi j^2$
Induced, j fixed, saturated	$\frac{\delta_i}{W} \propto p^3 s^1 \cdot M_s^i j$
Induced, I fixed, saturated	$\frac{\delta_i}{W} \propto p^3 s^{-1} \cdot M_s^i I$
Induced, I fixed	$\frac{\delta_i}{W} \propto p^3 s^{-2} \cdot \chi I^2$

Table 2.4: The dependency of the deflection on the scaling s and aspect-ratio p is an important design parameter. The permanently magnetic cilium and the different regimes of the paramagnetic cilium display different behaviour.

Chapter 3

A permanently magnetic PDMS composite

3.1 PDMS

Polydimethylsiloxane (PDMS) is a silicon-based organic polymer which is transparent, non-flammable and non-toxic. As mentioned in section 2.3.2, it is widely used in microfluidics in cross-linked form and available from various vendors¹. This alternating co-polymer is built from the monomer $-\text{Si}(\text{CH}_3)_2-\text{O}-$. PDMS is visco-elastic, which means that it behaves as a liquid at large timescales (order of a day for uncured PDMS), and as an elastic solid at small timescales (order of a second for uncured PDMS).

In uncured form, polymer chains are not connected and can slide alongside each other. To create more solid structures with PDMS, links need to be created between the long molecules so their relative movement is restricted. This process is termed cross-linking or curing, and makes the polymer more like an elastic solid, a silicone resin. One way to achieve this is to turn some of the methyl ($-\text{CH}_3$) groups into $-\text{H}$. Combined with vinyl ($-\text{CH}_2=\text{CH}_3$) groups at the ends, cross-links are made between different PDMS chains. The commercially available product Sylgard-184 (Dow Corning, [77]) employs this technique, and is shown in figure 3.1. In practise, vinyl-terminated PDMS (called “base”) is supplied separately from H -group-containing PDMS (cross-linking agent). Just before processing, they are mixed. Then the mixture is cast into the desired shape. After a day it has

¹PDMS is produced by Dow Corning, GE Silicones, Gelest and UnitedChem; it is sold by e.g. ABCR and Sigma Aldrich.

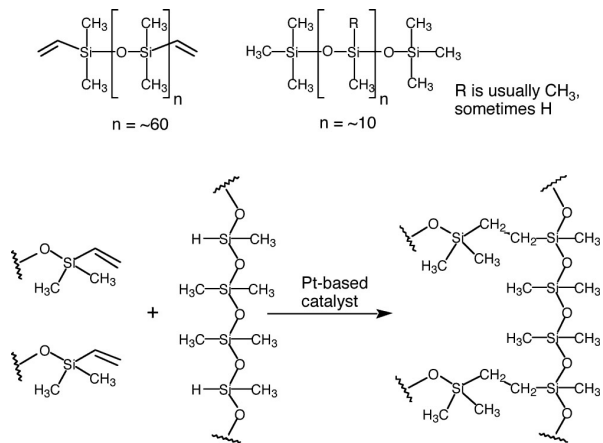


Figure 3.1: The Sylgard-184 formulation of polydimethylsiloxane (PDMS) (top left) and the accompanying cross-linking agent (top right), which are mixed together and cured to create cross-links and make a silicone resin (bottom). [26]

become solid, though only after seven days cross-linking is completely finished. This curing can be accelerated by increasing temperature; at 100°C it becomes solid after an hour already [18].

PDMS is given a specific shape by casting it into a mold during curing. When it is cured, the mold is removed and the solid PDMS keeps its shape. How exactly PDMS is put into a cilium-shape will be treated in chapter 4. The current chapter describes how PDMS is made magnetic by doping it with magnetic particles. The initially liquid state of PDMS helps in dissolving and making a homogeneous composite.

3.2 Particle selection

As discussed in section 2.3.4, permanently magnetic particles with high remanent magnetisation and high coercive field are required. Their size should be a fraction of the smallest dimension of the cilium. Although particles of rare-earth magnetic materials would be preferable because of their high coercive field, they have not been found to be commercially available with diameters of tens of micrometres or below. Therefore, iron was chosen as an alternative; cobalt is a good second choice, having a somewhat lower saturation magnetisation.

There is a problem though, when using nanoparticles because they react when exposed to air [52]; at the very least, an oxide layer is formed with less favourable magnetic properties. A solution was found in coated nanoparticles. By having the particles encapsulated in a protective shell, they are shielded from air. Mknano sells carbon-coated iron particles of 70nm in diameter, of which the outer 2 – 5nm is carbon shell, according to the manufacturer. The chemical notation of such carbon-coated iron particles is Fe@C. The iron core has a diameter of at least 60nm, which is above the theoretical single-domain limit of 13nm, so that multiple domains exist in each particle (appendix A). Other suppliers and products are summarised in appendix B.

3.3 Fabrication

3.3.1 Dispersion

To get a homogeneous material, magnetic particles need to be well dispersed in PDMS, which has too high a viscosity to be able to add particles directly. Particles were mixed first with a solvent in which they remained better dispersed. Then the PDMS base was added, and they were mixed. To be able to process PDMS in the regular way, the solvent was allowed to evaporate by putting it on a hotplate for about 12h just below its boiling point.

A requirement of the solvent is that it mixes well with PDMS. This was investigated in [48], from which a selection of compatible solvents was made².

²Tetrahydrofuran (THF), xylene, chloroform, hexane, toluene, methanol, dimethylsulfoxide (DMSO), demi-water and ethanol were selected; acetone was impractical because it dissolves most plastics too easily, and glycerol has too high

The solvent with best dispersion for the Fe@C particles was determined experimentally as follows. A fixed amount of 0.005g of Fe@C powder was added to 1.2ml of solvent, after which it was put in an ultrasonic bath for five minutes. After that, Fe@C particles were dissolved in each of the solvents, giving them a black tint. Subsequently, the dispersions were allowed to sediment. After an hour, only tetrahydrofuran (THF) and chloroform were still non-transparent. After a day, the THF dispersion was sedimented completely, which left chloroform as the more suitable solvent. To almost completely disperse all particles into chloroform, an amount of about 240ml is needed for each gram of Fe@C.

When mixing particles in a solvent, care must be taken that all particles are dispersed in the solvent and little is sedimented. While the ultrasonic bath breaks apart clusters of particles, it does not mix the solution on a large scale. Especially with large amounts of solvent, it is necessary to mix the particles through the whole volume by shaking it by hand before putting it in the ultrasonic bath. Even then, it may require several cycles of hand-shaking and ultrasonic bath to mix the particles well enough.

The imperfect dispersion of these particles may be improved by the use of a suitable surfactant. This is quite common in paramagnetic particle suspensions, also called ferro-fluids. A surfactant usually prevents their clumping together; only when particle clusters are small enough does the Brownian motion keep them in state of suspension. While paramagnetic particles have no interacting magnetic moment in zero external field, permanently magnetic particles always cluster magnetically, which makes it harder to keep them in suspension.

3.3.2 Casting & curing

When the particles are mixed with the PDMS base and the solvent is evaporated, the PDMS can be processed regularly (as specified by the manufacturer). The curing agent is added in a 10:1 ratio, and stirred by hand or a vortex shaker. From this point, cross-linking begins and does not stop until the PDMS is solid. According to the manufacturer, its viscosity is doubled within two hours at room

a viscosity to dissolve particles homogeneously.

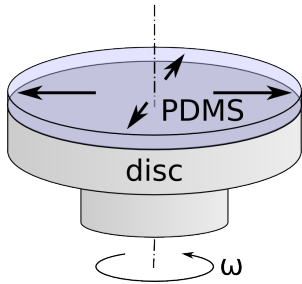


Figure 3.2: A thin layer of PDMS can be obtained by spin-coating it on a disc. The rotation speed ω of the disc pushes the PDMS outward, while a flat layer remains.

temperature. Within that time span, it has to be put in the desired shape (more on that shortly). To avoid bubbles being caught in the material that entered during mixing, it is essential to place the sample a couple of minutes in vacuum, until no bubbles come out anymore. Finally it is put on a 90°C hot-plate for two hours, after which it can be peeled off the substrate if required. Full mechanical strength will only be attained after longer curing times, up to seven days at room temperature.

It is often desirable to have a flat layer of PDMS, for example as part of a multi-layer production process. This is commonly obtained by spin-coating the still liquid PDMS base + agent mixture onto a substrate, rotating it with a well-defined speed (see figure 3.2). The centrifugal force pushes the material to the outer edges until it is equal to the shearing force, which depends on layer thickness and viscosity. In this way it is possible to create a layer of a specific thickness W by setting the rotation speed ω . Their relation is described by

$$W = k\eta_0^\beta\omega^\alpha, \quad (3.1)$$

with η_0 the initial viscosity and α , β and k empirically determined constants [63]. Sylgard-184 PDMS thicknesses resulting from different spin-coating speeds are presented in figure 3.3. A fit resulted in values of³ $k\eta_0^\beta = 0.23 \text{ m rpm}^{-\alpha}$ and $\alpha = -1.14$.

There is an upper limit to the layer thickness that can be obtained by spin-coating. During rotation, excess polymer is pushed to the outer edge of the sample. If the force is large enough, it is pushed

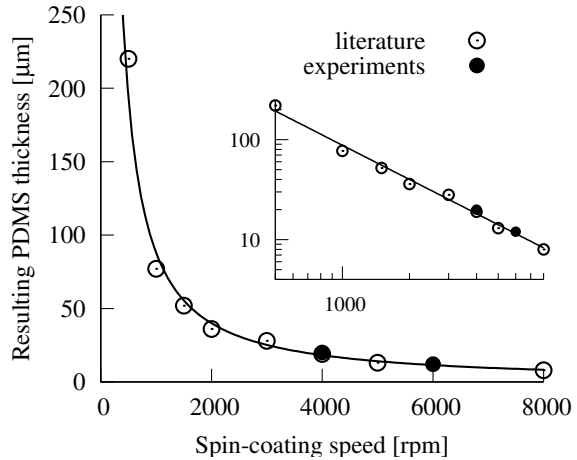


Figure 3.3: Sylgard-184 PDMS thickness as a function of spin speed, just after base and agent were mixed in a 10:1 ratio. Closed circles are measurements with a spin time of $t = 30\text{s}$, open circles are data points from [58] with $t = 60\text{s}$, and the solid line is a theoretical fit discussed in the text. The inset shows the same plot on logarithmic scales.

over the edge and released from the sample. But there is a barrier of surface tension that needs to be overcome, resulting in a thicker layer of PDMS near the edge. While the relative amount of extra PDMS near the edge is negligible for a small thickness, it becomes a real problem at several hundreds of micrometres and beyond (for substrate areas in the order of cubic centimetres and below). When such a thickness is needed, other processes may be better. For example, putting a defined amount of polymer on a sample of known area. Gravity will cause it to flow and create a flat layer. Again, surface tension may alter the edges, but the centre is flat if the sample is large enough.

While spin-coating is a practical method in general, it has sometimes proved to be problematic with magnetic particles inside. During rotation, there is a lot of polymer movement going on. Magnetic particles move with it and interact with each other. This can, for example, make them cluster and swirl in the direction of rotation. [31] mentions some remedies, or alternatively the method as described in the previous paragraph can be used.

³Empirical relations can be a bit sturdy on dimensions.

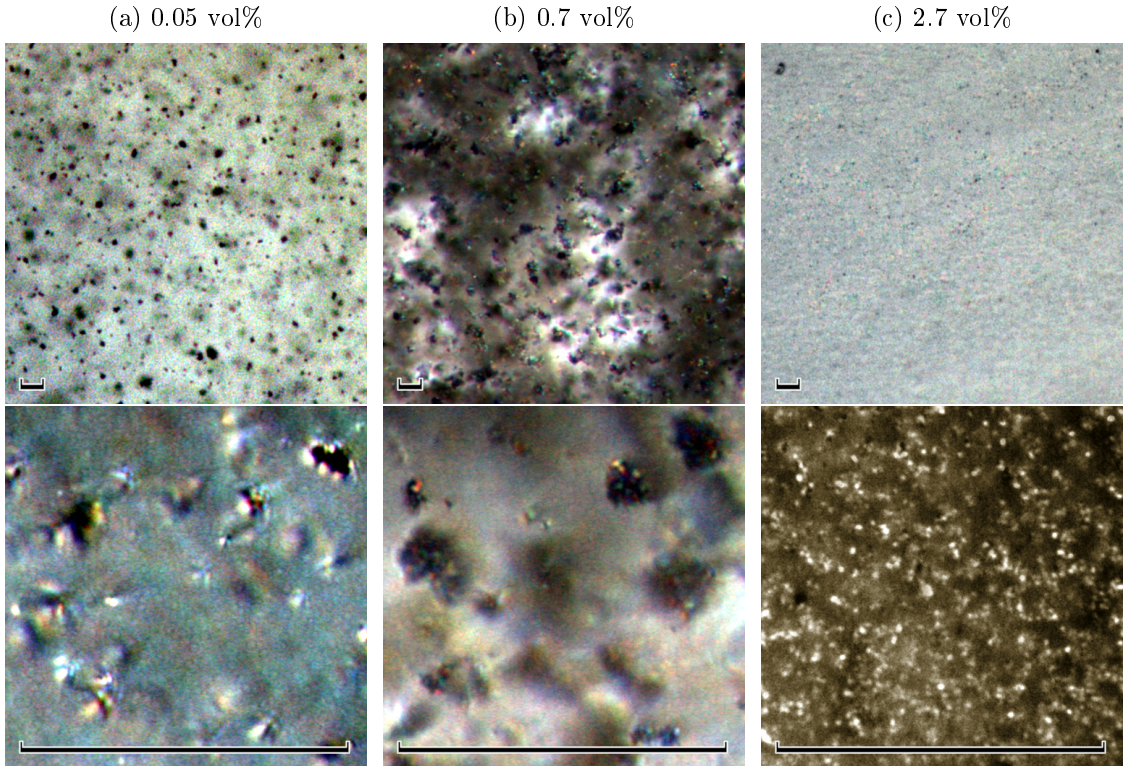


Figure 3.4: Microscope images of Fe@C-PDMS composites with different volume percentages of Fe@C in PDMS. The scale bar in each image is $25\mu\text{m}$ in length. Since the particle-density is so different for these samples, lighting and post-processing were adapted for each image to make the features better visible. Colour or brightness can not be compared, but the increasing particle density is recognisable; also clusters and aggregations can be recognised. Because of the high particle density in (c), it is impossible to look as deeply into the sample as the others, so larger three-dimensional aggregations are hardly visible.

3.4 Result

Fe@C-PDMS composites with volume percentages in the range between zero and ten were created according to the directions in section 3.3. Samples with concentrations over 3vol% appeared to be not fully cured after seven days, sticking to whatever it touched; the higher the concentration, the less mechanically stable it was. A Sylgard 184 datasheet mentions explicitly that organo-metallic compounds can inhibit curing [77]; this apparently limits the maximum Fe@C concentration to 3vol% in Sylgard-184.

3.4.1 Optical inspection

Figure 3.4 shows micrographs of a selection of composites at different concentrations. At low concen-

trations, much of the incident light passes through the sample and gives a deep look into it. One can see that clusters of up to about $10\mu\text{m}$ in diameter are formed. While this is not as well visible for figure 3.4c, it has been observed for higher concentrations as well.

When the volume percentage is low, Fe@C clusters are relatively homogeneously dispersed throughout the PDMS. As the concentration increases, the magnetic interaction increases, and larger-scale structures are formed. This is visible in figure 3.4b as dark clouds in the background.

While the orientation of these structures is random throughout the material, it can be made anisotropic by applying a magnetic field early in the curing process. This aligns the magnetic moment of particles in the direction of the field; and because the composite is still liquid at that time, particles

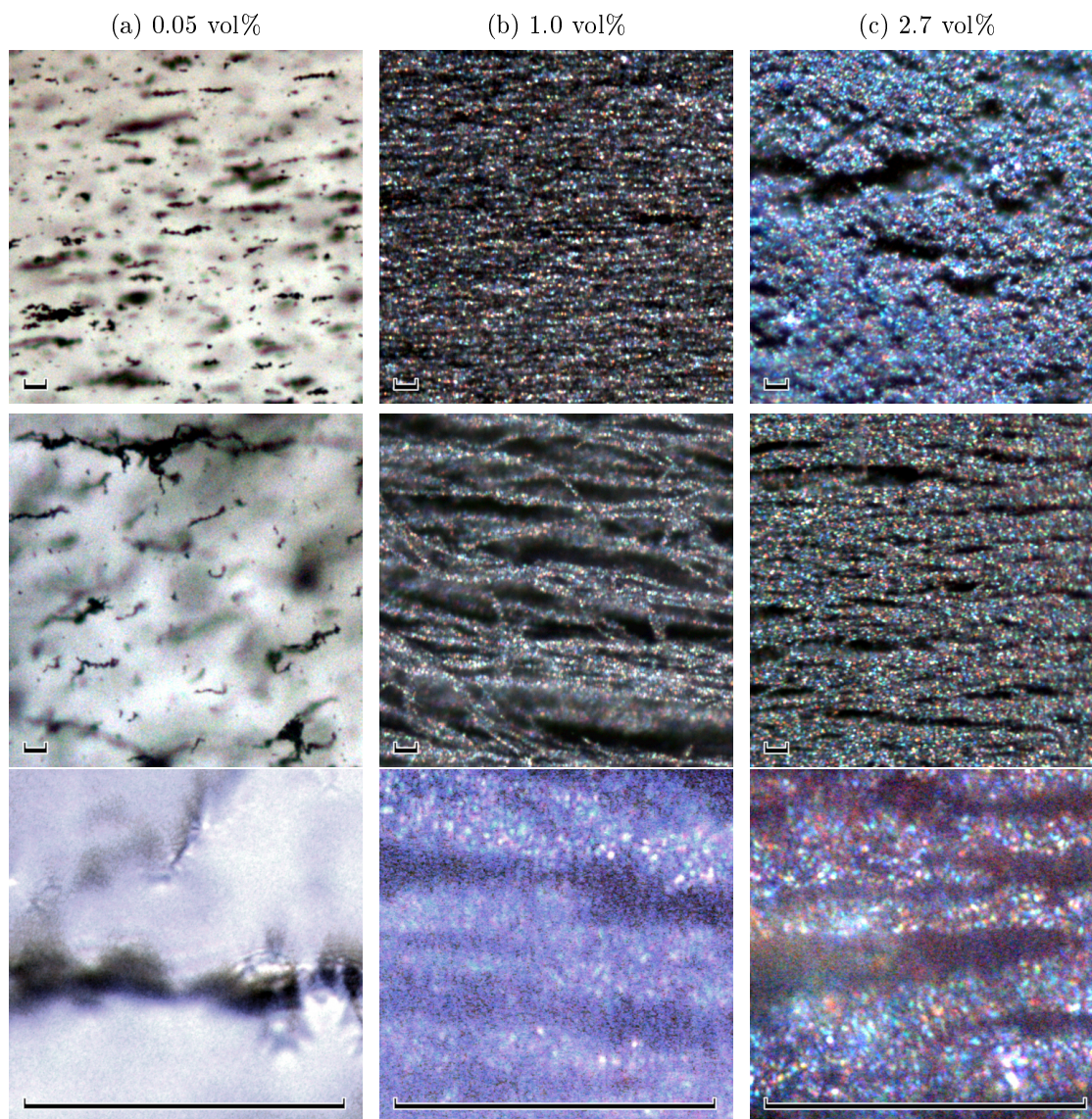


Figure 3.5: Microscope images of Fe@C-PDMS composites with different volume percentages that were partly cured in a horizontal magnetic field. The scale bar in each image is $25\mu\text{m}$ in length. Before curing on the hotplate, the samples were placed in a magnetic field for a day at 4mT (top row) or for a minute at 92mT (middle and bottom row). Note that lighting conditions and post-processing were different for each image, so the same comment applies as for figure 3.4.

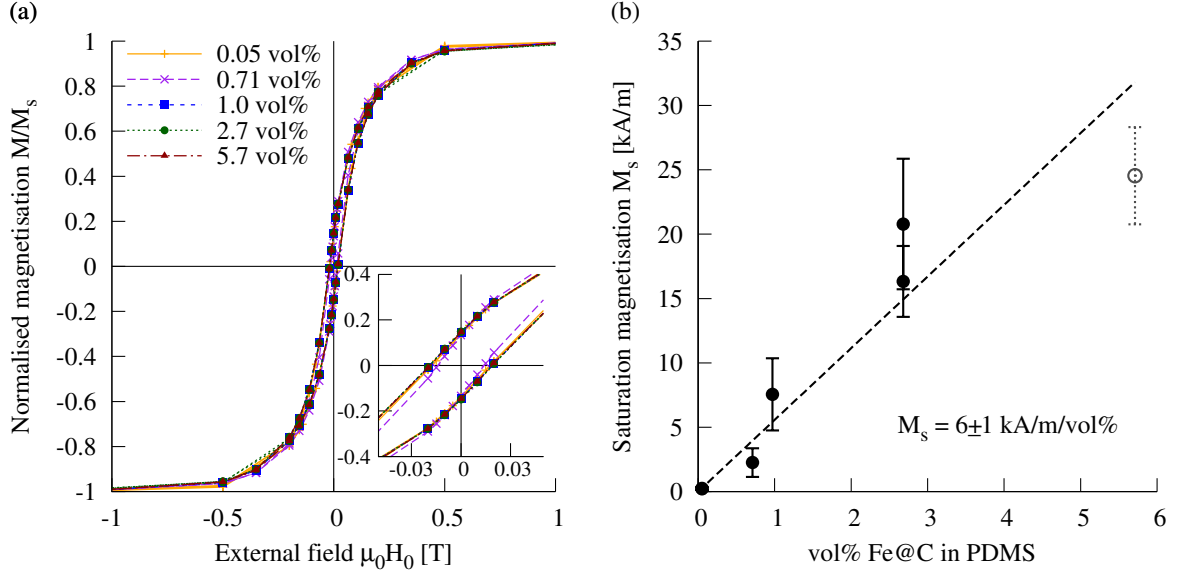


Figure 3.6: Magnetic measurements on Fe@C-PDMS composites of different volume percentages Fe@C in PDMS. (a) shows hysteresis curves divided by their saturation magnetisation so that $M/M_s = 1$ at saturation. The different curves overlap quite well, so qualitatively magnetic behaviour is independent of particle concentration. (b) shows the relation between concentration and saturation magnetisation $M_s = \mu/V$ with μ the measured magnetic moment; the volume measurement is the source of the large error bars. The most right data point at 5.7 vol% was not taken into account for fitting, since at this high a concentration not all Fe@C ended up in the PDMS, and the actual volume percentage is lower.

are free to move and structure themselves along the field lines. This can be seen in figure 3.5. When a magnetic field was applied for a day (top row), particles had much time to rearrange themselves; the field was kept low to avoid excess movement towards the pole tips. When a stronger magnetic field was applied for a minute (middle and bottom row, 92mT), less regular complexes were formed with an average direction along the field lines.

Since each Fe@C cluster has more or less the shape of a sphere, there is a demagnetising field (section 2.2.3) that reduces the total magnetic moment. By creating long structures, the demagnetisation factor can be reduced, which results in a larger effective magnetisation. The influence of field-curing has been shown to have a considerable effect on the susceptibility of paramagnetic composites [90]. But the influence on magnetic properties of this material needs to be quantified by magnetic characterisation.

3.4.2 Magnetic characterisation

The magnetic response of the Fe@C-PDMS composite has been measured by a vibrating sample magnetometer (VSM; DMS Magnetics, Model 10 VSM). To cancel the effect of the demagnetising field caused by shape anisotropy, a thin disc of 5.5mm in diameter and about 0.2mm high was cut out of the composite. It was measured with a field parallel to the long axes, so with $\mathcal{N}_\perp \approx 0.94$ and for both in-plane axes $\mathcal{N}_\parallel \approx 0.03$ it is negligible (see figure 2.4).

3.4.2.1 Concentration dependence

Figure 3.6a shows the magnetisation curves of composites of different concentrations. Each was scaled with respect to its saturation magnetisation. The fact that all of these overlap is an indication that the interaction between particles is comparable for the different composites, and independent of the volume percentage of Fe@C in PDMS. The rema-

nent magnetisation is $M_r = 0.16 M_s$ and the coercive field is $H_c = 17.5\text{mT}$. This is considerably lower than the 70mT for the particles mentioned in section 2.3.4, but in the same order of magnitude.

Of each sample, the volume was estimated with a calliper. By dividing the total magnetic moment μ as measured with the VSM by the volume, the magnetisation is obtained. The saturation magnetisation is shown in figure 3.6b as a function of Fe@C concentration. Since magnetic behaviour does not seem to depend on the concentration, a linear relation can be expected. Assuming this, a volume percentage of 100% Fe@C would result in an equivalent bulk saturation magnetisation of $0.6 \pm 0.1 \text{ MA/m}$. When the volume of the carbon shells is subtracted, this results in a saturation magnetisation of the iron particles⁴ of $0.8 \pm 0.2 \text{ MA/m}$ (for 2 – 5nm carbon shells). This is considerably less than bulk iron, which has⁵ $M_s = 1.7\text{MA/m}$. While the error may be larger than estimated here due to imperfect dispersion of Fe@C in PDMS, this cannot account for a factor of two. It is possible that, despite the protective carbon coating, some oxidation has taken place, turning iron into magnetite (Fe_3O_4), which has a saturation magnetisation⁵ of 0.5MA/m .

Since the scaled curves for different concentrations overlap, also the susceptibility χ has a linear relation with the volume percentage. For 100% Fe@C, this would result in $\chi = 5$ (near the origin)

3.4.2.2 Liquid, solid

For comparison, magnetic measurements on Fe@C were done in two other ways. First, Fe@C powder was packed in a container and covered with a thin layer of glue. This resulted in the solid green magnetisation curve of figure 3.7, and it can be seen that the behaviour of the composite is followed. This shows again that the interaction between clusters is independent of concentration.

Secondly, Fe@C particles were suspended into chloroform; in this case the vibration of the VSM measurement kept the particles better suspended in the solvent. The saturation magnetisation was

⁴The relation between the average magnetisation of Fe@C and the magnetisation of Fe is given by $\frac{M_{s,\text{Fe@C}}}{M_{s,\text{Fe}}} = \frac{\mu/V_{\text{Fe@C}}}{\mu/V_{\text{Fe}}} = \frac{V_{\text{Fe@C}}}{V_{\text{Fe}}} = \frac{(r-d)^3}{r^3}$, with r the radius of the particle, and d the thickness of the carbon shell.

⁵See table 2.2 on page 20 and A.2 on page 63.

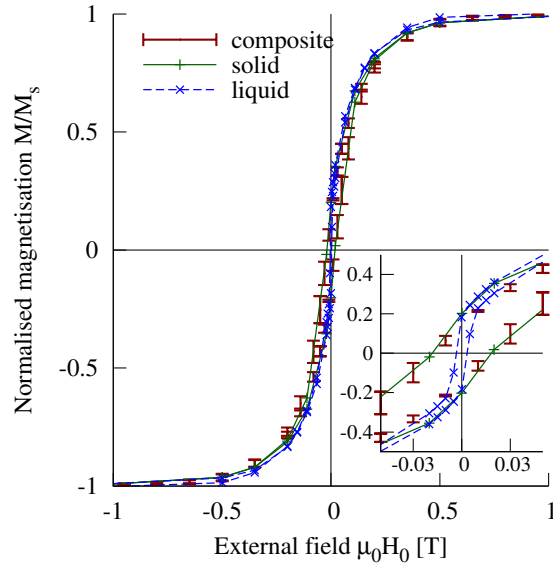


Figure 3.7: Normalised magnetisation curves of Fe@C in different forms. The dashed blue line is a measurement of Fe@C particles suspended in chloroform, the solid green line of a pressed powder of Fe@C particles, and the red vertical error bars show the smoothly interpolated average of the PDMS-composites of figure 3.6a.

measured to be $0.7 \pm 0.2\text{MA/m}$, which confirms the composite's measurement. The magnetisation curve is shown as the dashed blue line in figure 3.7 and follows the other curves, except near the origin. This is caused by the mobility of the particles in the fluid. When an external field is applied, the magnetic domains inside the particle rotate to align the field. But if the particles are inside a fluid, the moment can additionally be aligned by physical rotation of the particles. Because they can relax more easily, the energy required for rotation of the magnetic moment is reduced. Near the origin, where the external field is smaller than the particles' coercive field, the nanoparticles can rotate physically to align their magnetic moment, whereas particles fixed in a matrix can not. This explains the difference between the magnetisation curve for the liquid suspension, and the composite and solid curves.

Another consequence, albeit very small, is that the liquid curve remains above the others and reaches saturation a little sooner. The particles in

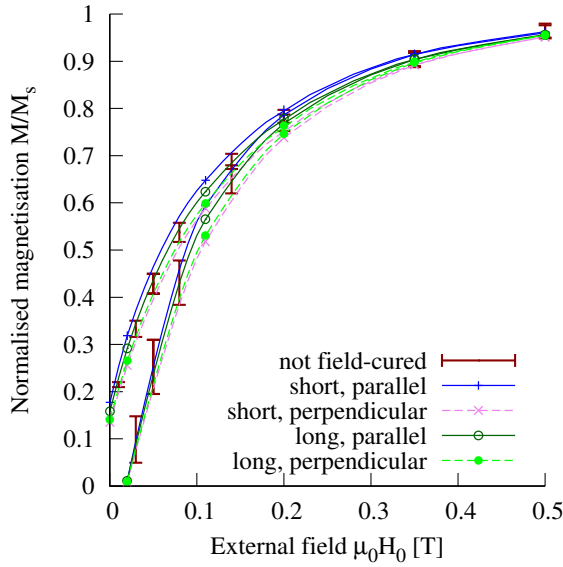


Figure 3.8: Normalised magnetisation curves of field-cured Fe@C-PDMS composites of 1.0vol% (only part of the upper right quadrant is shown). The composite was either cured for a day in a field of 4mT (long) or for a minute at 92mT (short); see also image 3.5 on page 31. Measurements were done with the external field parallel to the curing-field of the sample as well as perpendicular. The difference between the solid and dashed curves shows that field-curing induced magnetic anisotropy. The smoothly interpolated average of non-field-cured composites is shown as error bars.

the liquid have an extra mechanism for domain reversal, so they can follow the field slightly faster. Rotation and growth of domains inside particles is equal for the liquid, solid and composite.

3.4.2.3 Field-curing

Also the composites that have been put in a magnetic field early in the curing process have been measured with the VSM. The result is shown in figure 3.8. The solid lines were measured with the external field parallel to the direction of the curing-field, the dashed lines perpendicularly. There is a consistent difference between the parallel and perpendicular measurements, showing that field-curing has a magnetic effect and causes magnetic anisotropy. However, the magnitude of this effect is almost completely within the errors bars of normal

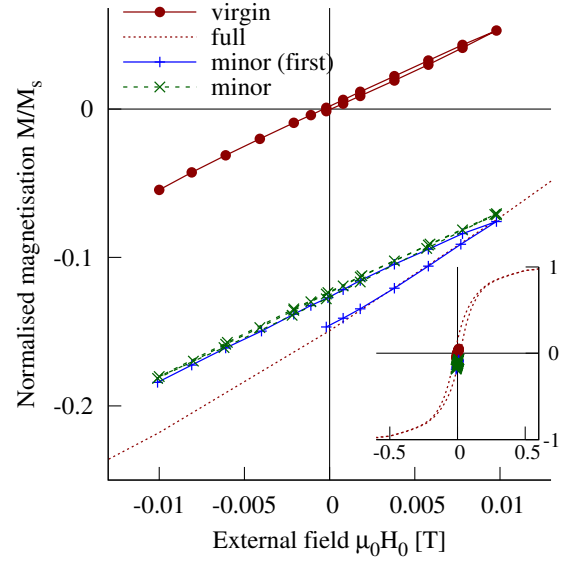


Figure 3.9: The behaviour of a 2.7vol% Fe@C-PDMS composite with external fields below the coercive field. The unmagnetised sample follows the virgin curve in the centre, showing no remanent magnetisation. After magnetising the sample, the solid blue line was measured, showing that the remanent field decreases slightly. Subsequent curves with fields below the coercive field are shown as dashed green lines, which are without hysteresis. The full hysteresis curve is shown as a dotted red line.

composite measurements. One can conclude that the effect of field-curing is small and of limited use to increase the magnetisation in permanently magnetic cilia.

The effect of field-curing is small and of limited use for application in permanently magnetic artificial cilia.

3.4.2.4 Minor loops

In section 2.3.4 it was explained that a permanently magnetic material only remains magnetised in a certain direction when the external field H_0 is smaller than the coercive field H_c . Therefore the behaviour of the magnetisation was measured for a composite in low opposing fields; this would be comparable to the actual operation of a per-

manently magnetic artificial cilium⁶. The result of this is shown in figure 3.9. First, the unmagnetised material was measured at low fields, giving the virgin curve (solid red line). Since the coercive field was not exceeded, there is hardly any hysteresis. Only after bringing the sample into magnetic saturation by an external field of 2T and removing it again, a remanent field remained. Then, magnetisation curves were measured, taking care that H_0 was kept below the coercive field. Such a magnetisation curve with fields below H_c is termed a minor loop. The first minor curve measured is shown as a solid blue line. It starts at the red dotted line, since that's where the magnetising process left it (coming here from $-2T$). A field is applied in opposing direction (a positive field in this case), and the magnetisation follows the full magnetisation curve. When the field starts to decrease again at 0.01T, it is abandoned. Subsequent minor loops (two of them were measured, shown as dashed green lines) show no hysteresis and keep a remanent magnetisation that is slightly lower than what the full hysteresis curve shows.

When a permanently magnetic artificial cilium is magnetised once and then actuated by application of a non-parallel magnetic field, it is important that the remanent magnetisation remains after repeated traversal of minor loops. These measurements give an indication that such is the case.

3.5 Conclusion

It is possible to create a permanently magnetic PDMS using 70nm Fe@C particles up to a concentration of 3vol% in Sylgard-184. Clusters of magnetic particles are present of up to $10\mu\text{m}$ in diameter. This composite has a saturation magnetisation $\text{vol}\% \cdot M_s = 18\text{kA/m}$, remanent magnetisation $\text{vol}\% \cdot M_r = 2.9\text{kA/m} = 3.6\text{mT}$ and coercive field $H_c = 17.5\text{mT}$. The use of field-curing has no substantial effect on the magnetic behaviour. Repeated actuation of a magnetised sample has no significant effect on magnetic properties.

The remanent magnetisation and coercive field are considerably lower than predicted in section

2.3.4. The maximum deflection for a permanently magnetic artificial cilium of $W = 10\mu\text{m}$ and $L = 120\mu\text{m}$ now becomes $\delta_p/W = 0.7$. This is not very promising, but could be improved by enlarging the aspect-ratio, increasing the particle concentration by use of another PDMS (whose curing is not affected by the presence of nanoparticles; see, for example, section 4.1.2), or by using stronger magnetic particles.⁷

⁶Although a permanently magnetic cilium would be actuated using a field perpendicular to its magnetisation and not opposing it, this measurement may give an idea of the behaviour in non-parallel fields.

⁷Furthermore, it will become clear in section 5.1.2 that the low coercive field does not prohibit the use of larger actuation fields.

Chapter 4

Micro-fabrication of artificial cilia

To create an artificial cilium, the polymer polydimethylsiloxane (PDMS) needs to be put into a shape with a large aspect-ratio, horizontally hanging over the surface (like figure 4.1, step ⑨). On the scale of a millimetre, this can be done by cutting the PDMS and fixing it on a surface, but smaller structures need a more sophisticated fabrication procedure.

Because PDMS is liquid in uncured form (see section 3.1) and exhibits low shrinkage upon curing, it can be poured into a mold to give it the desired shape, after which it is cured and becomes a resin. A mold is often created using the photoresist SU-8, which can be structured to sub-micrometre precision. While this replication-molding works well for many structures, the shape of a horizontal artificial cilium cannot be made using this method; the open space between cilium and substrate would require the mold to be present there, but removing the mold would break the PDMS structure just created. Hence the choice of horizontal fabrication by the use of a sacrificial layer to achieve a high aspect-ratio.

Before deposition of the PDMS, a sacrificial layer of polyvinyl alcohol (PVA)¹ was created at those places where the cilium should be hanging freely above the substrate. Then the PDMS was spin-coated and shaped using photo-lithography. After the PDMS had cured, the sacrificial layer was dissolved, resulting in a half-suspended beam.

The fabrication process is shown in detail in figure 4.1. The sacrificial layer was not photosensitive

¹PVA was chosen as sacrificial layer material, because it needs to withstand all subsequent fabrication steps, but still be dissolved at the end without affecting the cilium just created. PVA does not dissolve into the organic solvents used, and dissolves into water, which doesn't affect PDMS.

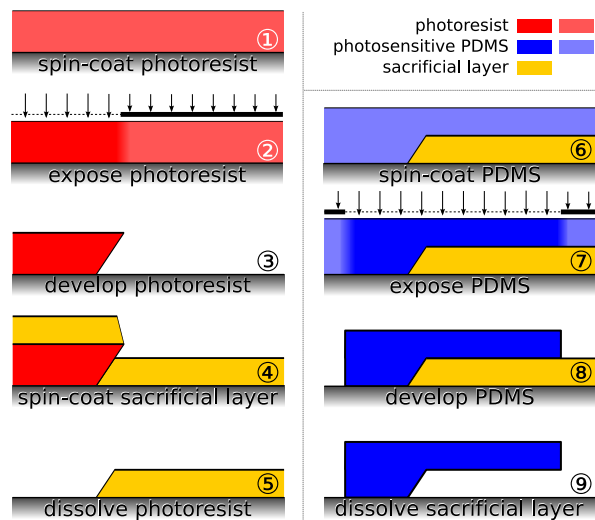


Figure 4.1: A schematic overview of the multi-layer photo-lithographic fabrication procedure of artificial cilia in PDMS. The left column shows how the sacrificial layer is created, the right column depicts how PDMS is processed.

in itself, so a photoresist was used to structure it using a lift-off technique. While that is a fairly standard procedure, photo-lithography of PDMS is not so widespread. The following sections will first explore the options for photosensitive PDMS and then discuss the entire fabrication procedure as explained here.

4.1 Photosensitive PDMS

Photo-lithography is a way to transfer a pattern from a photo-mask to a photosensitive material (photoresist or resist). A light source placed above

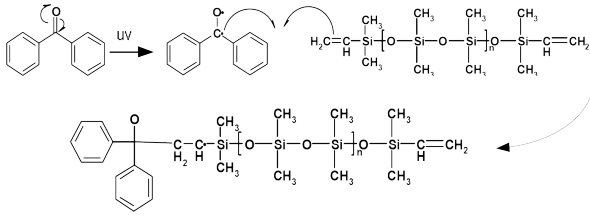


Figure 4.2: The presence of benzophenone in photoPDMS prevents PDMS from curing when exposed to UV by forming radicals that prevent cross-linking. [76]

the mask passes through its transparent parts, and projects the image onto the sample. Since UV light is typically used, the mask must be made from a UV-transparent material like quartz. Exposure induces a chemical process in the photosensitive material, and this is exploited in a succeeding development step to remove unexposed and keep exposed parts (a negative photoresist), or the other way around (a positive photoresist).

PDMS is not photosensitive in itself, absorbing only wavelengths below 250nm. It can be modified to be UV-sensitive, so that curing is either induced or prohibited for exposed areas. This is achieved by modification of the polymer to include photosensitive groups, or by addition of a photo-initiator that creates free radicals when exposed to UV. The latter is preferred because the former usually requires custom polymer synthesis.

While research on making photosensitive PDMS is an ongoing work [46, 88], there are two formulations with a low Young's modulus that have actually been applied to making microfluidic elements. The first, photoPDMS, makes common PDMS photosensitive by addition of a photo-initiator that prohibits subsequent curing when exposed to UV-light; the second, s-PDMS, is a combination of a specific PDMS combined with a photo-initiator that only cures when exposed to UV. These will be explained in more detail in the following sections, including experimental results.

4.1.1 photoPDMS

Heat-cured Sylgard-184 PDMS as described in section 3.1 was made photosensitive by the addition of benzophenone as described in [75, 76]. When exposed to UV light below 365nm, the C=O bond in benzophenone opens and it becomes a radical,

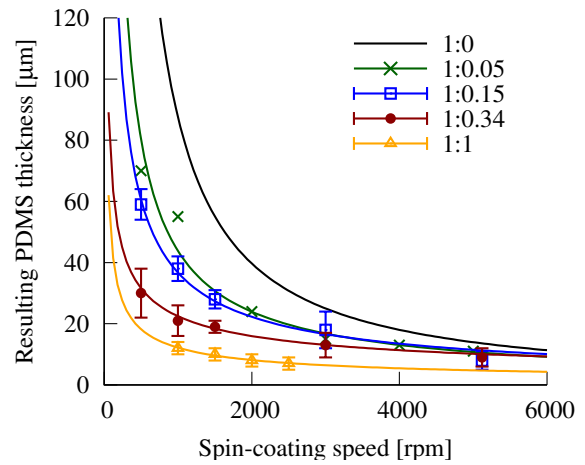


Figure 4.3: photoPDMS thickness as a function of spin speed for different PDMS:xylene ratios (in weight). The solid black line with no xylene is regular Sylgard-184 PDMS as discussed in section 3.3.2. Values for a ratio of 1:0.05 were obtained from [75], other data points were measured. Each curve was fitted separately to equation 3.1.

which prevents cross-linking of PDMS by reacting with its vinyl group (the absorption peak of benzophenone is around 250nm, see [24] for the absorption spectrum). The reaction is shown in figure 4.2. After exposure, photoPDMS is cured regularly, but only unexposed parts can cross-link with the regular mechanism as described in section 3.1. The exposed, uncured PDMS is subsequently washed away by toluene (development). Using this method, it should be possible to obtain a resolution of 100 μ m. Since the light absorption of benzophenone is mainly outside the visible spectrum, photoPDMS is suitable for processing under normal ambient light conditions.

4.1.1.1 Procedure

PhotoPDMS is created and used as follows. 0.033g of benzophenone is dissolved into 0.2g xylene. 1g of Sylgard-184 PDMS is mixed with 0.1g of its curing agent by stirring manually. Then both mixtures are put together, and all is mixed with a vortex shaker for 15 minutes. Bubbles are removed by putting it into a vacuum chamber for up to 15 minutes. At this time photoPDMS is ready for use.

Glass slides are used as a substrate and need to

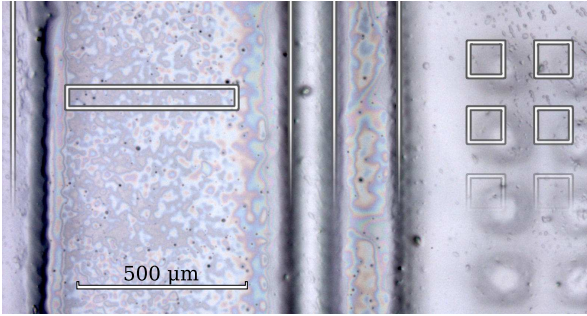


Figure 4.4: Microscope image of a photoPDMS sample of $12\mu\text{m}$ thick. The outline of mask that was used during UV-exposure is overlaid in white; it can be seen that the PDMS has swollen a little during the process. While vertical lines and troughs are distinctly visible, other shapes are barely formed (holes right), or completely removed (vertical bars left). The method is very sensitive to development and rinsing.

be cleaned beforehand to promote adhesion of photoPDMS; if this is left out, the structured PDMS will too easily get loose from the substrate during development and rinsing. The glass substrate is first cleaned using a detergent² and tap water. Then it is rinsed with ethanol and blow-dried using nitrogen gas. It is given a UV-ozone treatment for 10 minutes³, and again blow-dried with nitrogen just before use.

The photoPDMS mixture is spin-coated onto the glass slide. Because the presence of xylene makes the viscosity of the photoPDMS mixture lower than that of plain PDMS, the resulting layer thickness is different from Sylgard-184 (section 3.3.2). Figure 4.3 shows the thickness versus spin-coating speed for a number of dilutions⁴; the green line with a PDMS:xylene ratio of 1:0.05 corresponds to this procedure.

Then the sample is prepared for UV-exposure by positioning the photo-mask just above it with a spacer ($\leq 1\text{mm}$). Since at this point the photoPDMS is still non-cross-linked and sticky, the

²Dubro afwasmiddel, art. nr. 800

³Novascan PSD-UV

⁴Each curve was fitted separately to formula 3.1. This relation does not seem to describe these xylene-PDMS mixtures very well, since it was impossible to fit the curves with a shared parameter α and still obtain an acceptable correspondence. The graph should be seen as a starting-point for selecting a spin-coating speed.

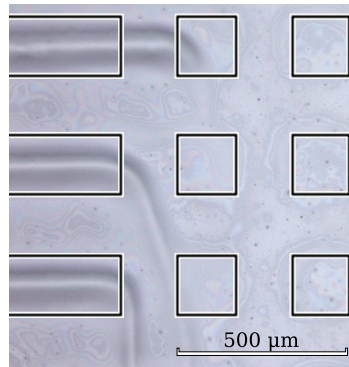


Figure 4.5: Microscope image of a photoPDMS sample of $10\mu\text{m}$ thick. The outline of the mask is overlaid in black. The downward bending of the horizontal bars shows that fluid movement during developing and rinsing affects the structures.

mask should not touch the sample. The sample is subsequently exposed to UV-light through the mask for 10 minutes at a distance of 35cm from the light source⁵. Immediately after that, it is put onto a hotplate at 120°C . The post-exposure bake time depends on PDMS thickness; for a thickness of $10\mu\text{m}$ (spin-coating speed of 5000rpm), 45s is suitable. Then the sample is developed by dipping it into toluene for 5s, rinsed with IPA and blow-dried using N_2 gas. Further curing is required to fully cross-link the PDMS.

4.1.1.2 Result

Figure 4.4 shows a resulting sample. Vertical features are clearly recognisable, but the right holes are barely developed, and the vertical bars left have vanished completely. This is due to development and rinsing; after post-exposure bake, the PDMS is still far from being completely cross-linked⁶ and very sensitive to mechanical tension created by putting it into the developer, removing, and rinsing. Still, this is necessary to remove the UV-exposed parts of PDMS. Probably the direction of fluid flow determines what features remain, and what parts are washed away. This is better visible in figure 4.5, where the ends of the vertical bars are

⁵EXFO Omnicure S1000 UV spot curing system with a high pressure 100W mercury short arc lamp and 320–500nm filter. The light was directed with an 8mm light guide and adjustable collimating adaptor. At a distance of 35cm from the light output, the spot size diameter was 13cm, so that with a recently purchased system and iris set to 100%, the irradiance was estimated to be $28\text{mW}/\text{cm}^2$.

⁶While cross-linking could be increased by baking longer, benzophenone would fail to inhibit curing so that the sample can no longer be developed.

increasingly affected. But features of about $100\mu\text{m}$ are attainable if this is only required in one direction.

4.1.1.3 Process parameters

Process parameters have been explored by varying UV-exposure dose, post-exposure bake time, and development time. Doubling the UV-exposure time did not make much difference, only the resolution was slightly worse (edges more spread out); this is probably due to benzophenone radicals having more time to diffuse in the PDMS. Also the timing between exposure and baking had to be kept to a minimum to avoid deteriorated resolution, which is likely to have the same origin.

The process appeared to be quite sensitive to post-exposure bake and development time. Too high a baking time results in curing of UV-exposed areas, and too low a baking time does not cross-link unexposed PDMS enough to survive development. There is just a small difference in cross-linking density between exposed and unexposed areas. During development most of the less cross-linked PDMS is dissolved, while most of the more cross-linked PDMS remains; but if the sample is left in the developer longer, eventually all PDMS is dissolved. This lack of selectivity is a problem for the robustness of this method.

4.1.2 s-PDMS

s-PDMS is a combination of the photo-initiator 2,2-dimethoxy-2-phenylacetophenone (DMPAP⁷) and the PDMS formulation RMS-033^{8,9} (Gelest), both shown in figure 4.6. In contrast with photoPDMS, this is a negative photoresist, where UV-exposure induces cross-linking. Its use is described in [20, 21, 22] and, more recently, in [46, 45]. DMPAP splits into two radicals when exposed to light (see [24] for the absorption spectrum). This also happens in ambient lighting conditions, so it has to be

⁷Sometimes abbreviated as DMPA or DMAP instead. It is also produced by Ciba under the name of Irgacure 651.

⁸2-4% methacryloxypropylmethylsiloxane - dimethylsiloxane copolymer, 1000-2000 cSt. Produced and sold by Gelest as RMS-033; also sold by ABCR as product AB113533.

⁹RMS-033 is commonly used, but DMPAP has also been used with other materials, including Sylgard-184 [88]. This was too experimental to pursue here, though.

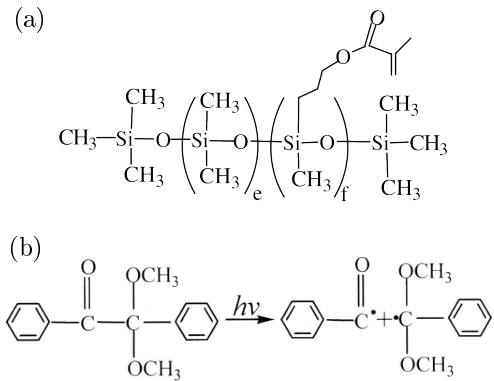


Figure 4.6: s-PDMS consists of (a) the PDMS formulation RMS-033 and (b) photo-initiator DMPAP, which forms radicals when exposed to UV-light. [46, 68]

processed in a yellow room. Since these radicals strongly react with oxygen[68], exposure needs to happen in an oxygen-free environment.

4.1.2.1 Procedure

s-PDMS is created and used as follows; all of this should happen in a yellow room to avoid premature activation of DMPAP. 0.02g of DMPAP is dissolved into 0.04g of xylene¹⁰. Then 1g RMS-033 is added and mixed by hand and vortex shaker. Bubbles are removed by putting it into a vacuum chamber for up to 15 minutes.

Glass slides are prepared as mentioned in section 4.1.1.1 to promote adhesion of PDMS to the surface, and the s-PDMS mixture is spin-coated on the glass substrate; at 5000rpm a PDMS thickness of about $10\mu\text{m}$ is obtained.

At this point, the sample is ready for UV-exposure. It is placed in an oxygen-free chamber with the photo-mask on top¹¹. For best result, the distance between photo-mask and sample should

¹⁰In [21, 22] the use of only 0.02g of xylene is mentioned, after which it is mixed it for an hour and let to stand overnight. When using twice this amount of solvent, the process as mentioned in the text appeared to suffice.

¹¹This can be achieved, for example, by taking a box that is open at the top, using the quartz photo-mask as a lid. By driving nitrogen gas through the box for a while before exposure, the oxygen is removed. During exposure, a steady flow of nitrogen gas maintains an over-pressure and keeps the oxygen out.

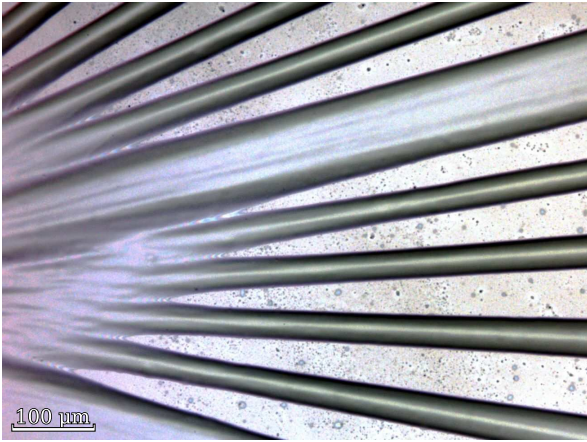


Figure 4.7: An *s*-PDMS sample of $6\mu\text{m}$ thickness that shows what resolution can be obtained. The speckled background is the substrate. Features are well defined down to a width of $40\mu\text{m}$; below that, PDMS remained at unexposed sites. This sample was created with 2wt% DMPAP and 8wt% xylene by spin-coating at 3000rpm and developing for 60s.

be small ($\leq 1\text{mm}$), but since the PDMS is still liquid, it should not touch the photo-mask. Then the sample is exposed to UV-light through the mask for about 60s at a distance of 70cm from the light source¹². Immediately after that, the unexposed *s*-PDMS is removed by developing it in xylene for 30s, and washing in IPA for 30s. After blow-drying the sample with N_2 gas, it is finished.

4.1.2.2 Result

Figure 4.7 shows an *s*-PDMS sample that was exposed with a photo-mask of converging lines. In this case, the lines have a height of $6\mu\text{m}$ over all of the substrate (this low thickness at a spin-coating speed of 3000rpm is due to 8wt% of xylene used here, instead of 4wt%). The substrate is clearly visible (speckled areas) and has no substantial remains of PDMS¹³. A feature size down to $40\mu\text{m}$ results in clearly defined, separate features; below that, PDMS remains at unexposed areas. This is caused

¹²See footnote 5 on page 39. At a distance of 70cm, the spot size was 27cm and the intensity was estimated to be $6\text{mW}/\text{cm}^2$.

¹³This was confirmed by scratching the surface and comparing the height of the scratched area with unexposed parts of the sample. No difference was found.

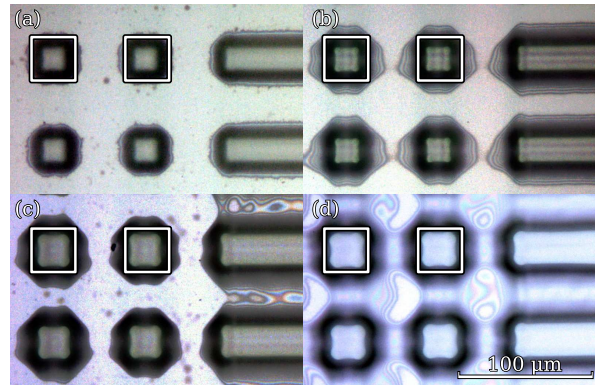


Figure 4.8: Microscope images of *s*-PDMS samples with increasing UV-exposure times. The rectangular mask outline is shown partially. (a) was exposed for 15s, resulting in a PDMS height of $2\mu\text{m}$; (b) exposure 30s, height $4\mu\text{m}$; (c) exposure 120s, height $8\mu\text{m}$; (d) exposure 240s, height $8\mu\text{m}$. The last sample is over-exposed, since some PDMS remained at unexposed areas. These samples were spin-coated at 5000rpm; only 1wt% of DMPAP and 2.5wt% of xylene was used.

by a combination of effects like diffusion of radicals into unexposed parts, and exposure of supposedly unexposed areas. The latter can be caused by reflections, and by the spacing between photo-mask and sample combined with a non-perfectly-parallel light source. Both result in some cross-linking of unexposed areas, which are not completely washed away by the developer. This resolution has been observed too in samples of $10\mu\text{m}$ thickness.

4.1.2.3 Process parameters

It is important to keep away oxygen during UV-exposure. [21, 22, 45] claim to achieve this by covering the sample with Mylar foil¹⁴ just after spin-coating. However, attempts to keep away oxygen using this method were not successful¹⁵. Sometimes it appeared hard to avoid air being trapped between PDMS and Mylar, preventing curing at those places. Furthermore, some PDMS remained stuck to the foil after exposure, and foil removal would take away also some cured PDMS. Doing UV-exposure while the sample is in a nitrogen-environment prevents these problems.

¹⁴A thickness of $23\mu\text{m}$ and $1.5\mu\text{m}$ was mentioned.

¹⁵Mylar C films with thicknesses between $6\mu\text{m}$ and $23\mu\text{m}$ were used (Pütz Folien, Germany).

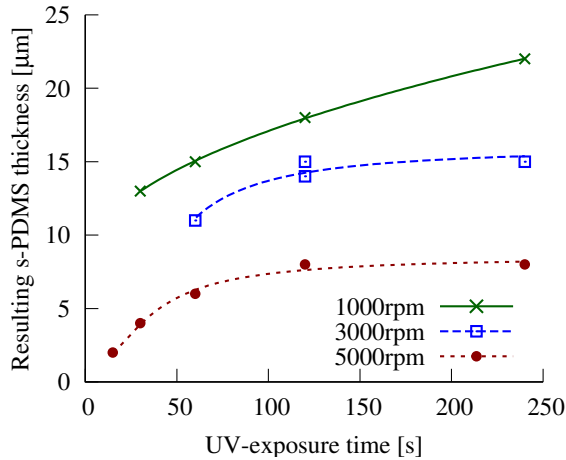


Figure 4.9: Resulting *s*-PDMS thickness as a function of UV-exposure time, for different spin-coating speeds. At 5000rpm and 3000rpm, an exposure of 100s mostly cures the layer, but thicker layers (lower spin-coating speeds) need a much longer exposure to fully cross-link. For these samples, only 1wt% of DMPAP and 2.5wt% of xylene was used.

The UV-exposure time depends on layer thickness. It must be large enough to cross-link the layer of its entire thickness, but over-exposure results in cross-linking of unexposed areas. This can be seen in figure 4.8, which shows micrographs for samples with different exposure times. As the exposure time increases, the size of the features increases, including their height. Ideally, the height of exposed PDMS should be equal to its height after spin-coating, and unexposed PDMS should dissolve into the developer. With a graph like figure 4.9 it is possible to determine the minimal exposure time, which is where the derivative approaches zero; note that only 1wt% of DMPAP and 2.5wt% of xylene was used in these measurements, which is slightly different from the procedure mentioned before. For a spin-coating speed of 5000rpm and 3000rpm, the minimal exposure time is around 100s (and with 2wt% DMPAP, the 60s mentioned in section 4.1.2.1 is reasonable). At lower exposure times, the material is not fully cross-linked. At higher exposure times, supposedly unexposed PDMS cures by the spacing between photo-mask and sample, light reflections and diffusion of radicals (figure 4.8d). Because thicker layers need more exposure, they have

a worse photo-lithographic resolution.

Development of the sample removes unexposed *s*-PDMS from the surface, because it has not cross-linked. The development time should be long enough to fully dissolve uncured PDMS, and longer development does not dissolve cured *s*-PDMS (in contrast with photoPDMS). However, the developer xylene does swell PDMS [48]. Especially large structures can swell so much that they detach from the substrate and start floating in the developer. For 10 μm -thick *s*-PDMS, this becomes a problem after a development time of 30s (for thicker samples this is even less). When longer development is needed, it is possible to wash the sample (shortly, as IPA also swells PDMS to some extent) and blow-dry it. When the sample has dried completely, the develop-rinse-dry procedure can be repeated with a lesser risk of swelling.

4.1.3 Conclusion

Two existing procedures for photo-lithographic processing of PDMS have been investigated. photoPDMS was able to obtain a resolution of about 100 μm with careful design of the photo-mask. *s*-PDMS could attain a resolution of 30 μm . While *s*-PDMS needs a yellow room and UV-exposure in an oxygen-free environment, its production process is more robust than that of photoPDMS; especially the sensitivity to the development time, which is already short, makes photoPDMS hard to use reliably.

This favours *s*-PDMS as a photo-lithographic solution. The following section will investigate the addition of magnetic particles and how it affects lithography.

4.2 Permanently magnetic photosensitive PDMS

Photo-structuring magnetically doped PDMS involves combining the procedures for the fabrication of a magnetic PDMS composite (section 3.3) and photo-lithographic PDMS (section 4.1). This is done by first dispersing particles into a solvent, mixing that with the plain PDMS (which is the PDMS base for photoPDMS, or RMS-033 for *s*-PDMS), and letting the solvent evaporate as described in section 3.3.1. Then the procedure

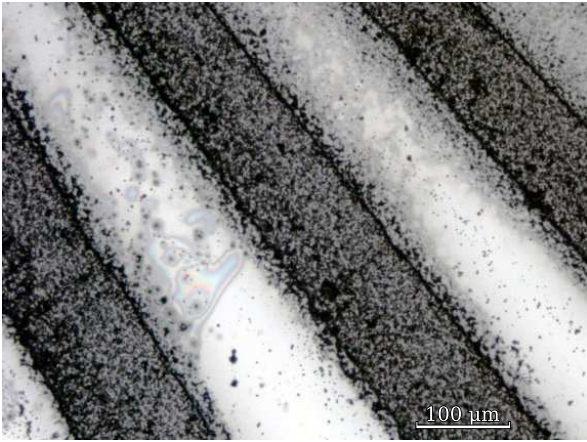


Figure 4.10: *s*-PDMS sample prepared with 8wt% of Fe@C particles with a thickness of $8\mu\text{m}$. The composite was structured in lines, which appear grey because of the particles. Clusters of particles are visible as black spots. While the substrate is visible in the lower right corner, a small layer of *s*-PDMS remained when the feature size dropped below $130\mu\text{m}$. Please refer to the text for more details.

for photo-sensitive PDMS is followed, using the particle-PDMS mixture instead of plain PDMS.

The photo-lithographic procedure is unmodified, except for UV-exposure. Magnetic particles are likely to absorb and scatter UV-light. This would increase the required exposure dose because of increased absorption, while light scattering into areas that are covered by the photo-mask would decrease the resolution. Also the maximum processable thickness can be lower for PDMS with particles inside. Since the amount of light remaining throughout the PDMS decreases from top to bottom, so does the amount of scattered light. So there is a trade-off between the particle concentration, resolution at the top, and attainable thickness (full cross-linking is required from top to bottom, since partly cross-linked PDMS at the bottom would dissolve in the developer and release the PDMS from the substrate).

While these issues are likely to play an important role at high particle concentrations, an unmodified UV-exposure time still yielded acceptable results for *s*-PDMS samples doped with 8wt% of Fe@C particles. An example is shown in figure 4.10. The substrate itself is visible in the lower right corner. Halfway the image, it can be seen that

a small layer of PDMS remained at unexposed areas; here the distance between neighbouring lines is about $130\mu\text{m}$, which is the resolution for this sample. Since the UV-exposure and development time were not modified from the standard procedure, it can be expected that optimisation results in a better resolution. For demonstration of the feasibility of a permanently magnetic cilium, this resolution suffices.

It is interesting to note that 8wt% exceeds the maximum particle concentration for Sylgard-184 as found in chapter 3. *s*-PDMS has a different cross-linking reaction that is not inhibited by the presence of Fe@C particles¹⁶. Even higher concentrations may be possible, although UV-exposure sets a limit on the thickness.

4.3 Micro-structured artificial cilia

Artificial cilia were fabricated following the process shown in figure 4.1 on page 37; circled numbers appearing in the text correspond to production steps in this figure. The procedure will be summarised again shortly, and described in detail afterwards.

4.3.1 Procedure

A sacrificial layer of polyvinyl alcohol (PVA, see footnote 1 on page 37) is deposited first to make sure that part of the cilium remains free from the surface and can move freely. Because it is not photosensitive in itself, a photoresist is used to shape it. First the photoresist is structured ①-③, and then the sacrificial layer is put on top ④, after which the photoresist is removed ⑤. Its removal lifts-off the sacrificial layer at places where the photoresist was present. Then the photo-sensitive PDMS is deposited on top and structured, after which the sacrificial layer is removed and the artificial cilium remains.

To successfully structure the sacrificial layer with the photoresist, some care needs to be taken. When photoresist covers the desired areas on the substrate ④, the sacrificial layer is spin-coated on top

¹⁶In contrast to Sylgard-184, there is no platinum-based catalyst that is affected by the presence of iron/carbon particles.

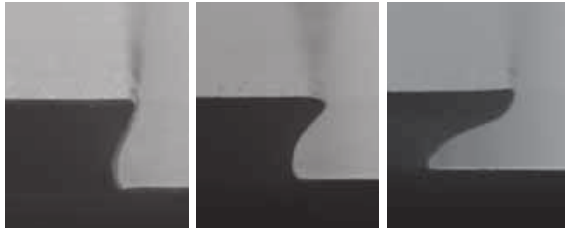


Figure 4.11: Cross-section of a ma-N 1400 (black) edge of a $2\mu\text{m}$ thick layer developed for 65s, 80s and 120s from left to right respectively. It can be seen that increasing development time increases under-etching. [93]

of it ⑤. Now some part of the sacrificial layer lays directly on the substrate, while another part is situated on top of the photoresist. The former is lifted-off the sample when the photoresist is dissolved. This can only happen reliably if these two parts are not in contact with each other. This is achieved firstly by keeping the distance between these parts at least twice the thickness of the sacrificial layer. Secondly, the photoresist needs to have a sharp edge (as depicted in ④ and figure 4.11). Both avoid that the surface-tension of the sacrificial layer keeps the parts connected.

Now following is the procedure for creating micro-structured artificial cilia. The numbers relate to figure 4.1. Please note that the procedure described here was used to create a proof-of-concept prototype. While some optimisation was done on critical steps (like photo-sensitive PDMS), it is outside the scope of current work to have this process completely fine-tuned.

- ① *Spin-coat photoresist* - a glass substrate is prepared as described in section 4.1.1.1, on which the photoresist ma-N 1420¹⁷ is spin-coated at a speed of 350rpm for 30s, which results in a layer of about¹⁸ $8\mu\text{m}$.

¹⁷Micro resist technology GmbH, ma-N 1400 series is a photoresist tailored specifically for lift-off that allows under-etching. See [55, 62] for more information.

¹⁸This is a little higher than what ma-N 1420 was meant for; spin-coating at such low a speed increases the risk of thickness inhomogeneity. There are other photoresists in the ma-N series that are more suitable, but with a sacrificial layer of less than a micrometer, the photoresist thickness can easily be reduced by a factor two. Nevertheless, the procedure as described is suitable and would allow the use of a thicker sacrificial layer.

- ② *Expose photoresist* - the substrate with photoresist is first baked on a hotplate at 120°C for $5\frac{1}{2}$ minutes, and then UV-exposed through a mask for about¹⁹ 150s at 70cm.

- ③ *Develop photoresist* - the sample is developed in ma-D 533S²⁰ for 5 minutes. Since the photoresist has a red tint, its progress can be monitored visually. The exact development time controls the amount of under-etching, as depicted in figure 4.11. After development, the sample is rinsed in demi-water for two minutes and dried.

- ④ *Spin-coat sacrificial layer* - a solution of 8.7wt% polyvinyl alcohol (PVA) in demi-water²¹ is spin-coated with a speed of 500rpm for 60s. It is subsequently baked on a hotplate for two minutes at 100°C to let the water evaporate. The resulting PVA thickness is about a micrometer.

- ⑤ *Dissolve photoresist* - the sample is then immersed into acetone, and as such put in an ultrasound bath for 5 minutes. This dissolves the photoresist and lifts-off these parts of the sacrificial layer where there underlying photoresist was exposed to UV.

- ⑥ *Spin-coat PDMS* - s-PDMS with Fe@C particles is created as described earlier in this chapter. It is spin-coated at 5000rpm for 30s on top of the sacrificial layer, so to obtain a layer of about $8\mu\text{m}$ thick. Details of steps ⑥-⑧ are mentioned in sections 4.1.2.1 and 4.2.

- ⑦ *Expose PDMS* - the sample is exposed to UV light in an oxygen-free environment.

- ⑧ *Develop PDMS* - subsequently it is developed in xylene, washed in IPA, and blow-dried using nitrogen gas. At this point, the PDMS is fully structured, with the sacrificial layer between the motile part of the cilium and the substrate.

- ⑨ *Dissolve sacrificial layer* - finally the sacrificial layer is dissolved in demi-water by immersion. The cilia come loose from the surface and the

¹⁹Corresponding to an exposure dose of $6\text{mW}/\text{cm}^2$; see also footnote 12 on page 41.

²⁰Also available from Micro resist technology GmbH as part of its negative photoresist series.

²¹This happened to be the maximum amount that could be dissolved, although heating may be able to improve it.

sample is ready.²²

Figure 4.12 shows micrographs of some of the intermediate steps. In subfigure (a) the under-etching can be recognised as the dark-red border. In subfigure (b) the resulting border of the sacrificial layer can be recognised. (c) shows a different sample with the sacrificial layer near the bottom corners; the vertical rugged lines in the centre are a scratch on the sacrificial layer, and it can be recognised in subfigure (d) that a small layer of PDMS has remained there. The two black squares of PDMS in (c) were in large part on top of the sacrificial layer, and hence have disappeared in (d). The only cilium on this sample that was situated to be freely suspended above the surface, is the most right one. This one will be analysed in the following chapter.

Other cilia were created too, and success greatly depended on the shape of the photo-mask. Large pieces of PDMS swelled a lot and came loose from the substrate, for example. Long cilia that were close together, tended to clump together (an example is shown in section 5.2.1) or stuck to the surface. The resolution for structuring Fe@C-PDMS appeared to be limited to some $100\mu\text{m}$, but this can be improved by fine-tuning the process, which has not been done for PDMS with particles inside. These and other issues would need to be investigated and addressed for application in microfluidic systems, where it is required to reliably make multiple artificial cilia. This is outside the scope of the current work, however; for now, it has been possible to micro-fabricate artificial cilia, and so their motile behaviour can be investigated in the following chapter.

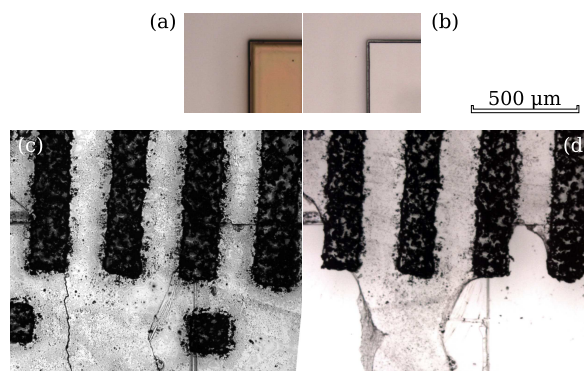


Figure 4.12: Micrographs of some intermediate steps in the production process, corresponding to step ④, ⑤, ⑧ and ⑨ of figure 4.1. (a) shows the structured photoresist (red) and the PVA sacrificial layer. In (b) the photoresist is dissolved and only the sacrificial layer remains. (c) shows a different sample with the structured layer of Fe@C-PDMS on top of the sacrificial layer; in (d) the sacrificial layer is removed. For the sample of (c) and (d), only the most right cilium actually succeeded because of a vertical scratch in the sacrificial layer over the centre of the image.

²²Just after dissolution of the sacrificial layer, the PDMS cilia are freely suspended above the substrate in water. As will become apparent in the next chapter, the sample has to remain inside a liquid to keep the cilia from sticking to the surface. Capillary forces pull them towards the substrate upon drying. But it is possible to mechanically release the cilia again.

Chapter 5

Feasibility prototypes

Now that a permanently magnetic PDMS composite has been created and characterised in chapter 3, and a fabrication method was developed in chapter 4, it is possible to experimentally investigate the behaviour of artificial cilia. Results will be compared with the theory presented in chapter 2, and will ultimately show if magnetically induced motion in permanently magnetic artificial cilia is feasible.

Two feasibility prototypes have been created: one with lengths in the order of millimetres, and another with a length in the order of tenths of millimetres. These will be treated in the following sections.

5.1 Large

Since the relative deflection of a permanently magnetic cilium δ_p/W is independent of scaling (section 2.4.1), the theory can easily be tested using a prototype with macroscopic dimensions, without having to resort to micro-scale fabrication techniques such as described in the previous chapter. A sample of a 2.2vol% Fe@C-PDMS composite was prepared as described in section 3.3. It was casted by spin-coating on a glass substrate at 1500rpm. When cured, a beam of $T = 3\text{mm}$ wide and about a centimetre long was cut out. The thickness was measured by a microscope to be $W = 66 \pm 4\mu\text{m}$.

The resulting macroscopic artificial cilium was attached to a piece of polystyrene by adhesion. The beam was then magnetised along its long axis by repeated movement of a permanent magnet at a field of about 0.5T. Subsequently it was placed in the homogeneous field of an electromagnet and observed from top with a microscope. A micrograph of one experiment is shown in figure 5.1.

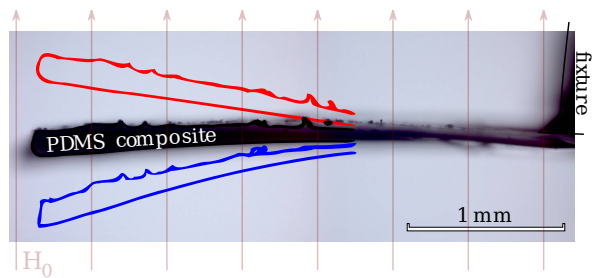


Figure 5.1: Annotated microscope image of a large permanently magnetic artificial cilium in a perpendicular magnetic field H_0 , which is generated by an electromagnet. The centre black shape is the cilium in the absence of a magnetic field. The upper red shape shows the deflection for a positive field, while the lower blue shape shows it for a negative field. Note that the cilium is twisted a little, so that it appears thicker at the tip.

A quantitative analysis was done by measuring the deflections for different field strengths. This is shown in figure 5.2 for two different lengths of cilia, where each line is a linear fit. That the solid blue line does not go through the origin is due to a small amount of hysteresis present in the cilium movement¹.

The macroscopic artificial cilia have a deflection that is linear with field strength, as predicted by formula 2.7. For the cilium of length $L = 0.92\text{mm}$, the experiment shows a deflection of $\delta/W = 0.012\text{mT}^{-1}\mu_0 H_0$. According to equation 2.7 and the parameters of the experiment², this would indicate that the Fe@C particles inside the

¹This was best visible by the zero position not being equal every time. There is both a small amount of mechanical hysteresis of the cilium and magnetic hysteresis of the magnet.

² $L = 920\mu\text{m}$, $W = 66\mu\text{m}$, $E \approx 0.5\text{MPa}$, $\text{vol}\% = 2.2\%$

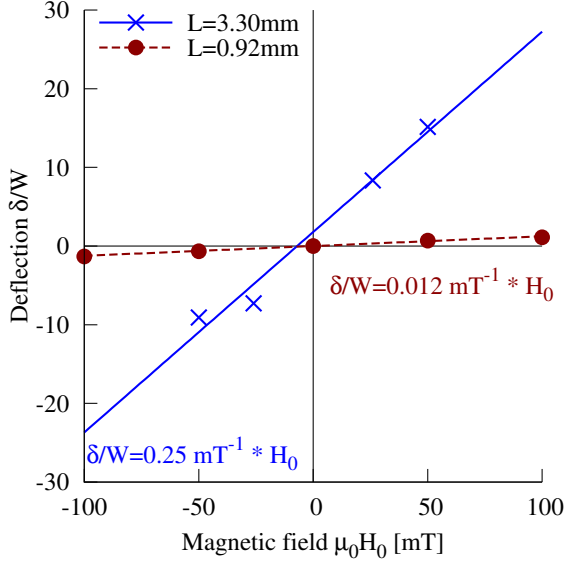


Figure 5.2: Deflection as a function of field strength for two permanently magnetic artificial cilia of different lengths L , but otherwise equal. The thickness is $W = 66\mu\text{m}$.

cilium have a magnetisation of $M = 25\text{kA/m}$ parallel to the cilium, perpendicular to the field. Although a magnetisation corresponding to the maximum remanent magnetisation $M_r = 96\text{kA/m}$ may have been expected from VSM measurements in section 3.4.2, it is quite probable that magnetising beforehand did not completely magnetise the material, and so the remanent field is just a fraction.

The artificial cilium of length $L = 3.3\text{mm}$ shows a deflection of $\delta/W = 0.25\text{mT}^{-1}\mu_0H_0$. If the magnetisation is calculated directly from the model valid for small deflections (equation 2.7), the Fe@C particles' magnetisation would be³ $M = 11\text{kA/m}$. This is about half the value for the previous experiment, and can be explained by the much larger deflection. Figure 2.8 on page 23 shows that for deflections over five times the width, behaviour becomes sub-linear. So the actual magnetisation required for this deflection would be higher, which is in agreement with the previous experiment.

³ $L = 3300\mu\text{m}$, $W = 66\mu\text{m}$, $E \approx 0.5\text{MPa}$, $\text{vol}\% = 2.2\%$

5.1.1 Estimation of induced moment

To rule out the influence of an induced magnetic moment in this experiment, the deflection because of a parallel as well as a perpendicular induced moment will be estimated.

A permanently magnetic material has a remanent field when no external field is present, but it also has a susceptibility so that its magnetisation changes when a field is applied. This allows an induced magnetic moment to play a role in a permanently magnetic cilium, of which the component parallel to the field induces a force in the direction of the gradient, perpendicular to the cilium; the resulting deflection δ_i is described by equation 2.5. The electromagnet was analysed by simulations, and the gradient was determined to be below 0.8T/m within the cilium's area of movement. Taking a susceptibility⁴ $\text{vol}\% \cdot \chi \approx 0.1$, this would give a maximum deflection of $\delta_i/W \approx 0.004\text{mT}^{-1}\mu_0H_0$ for $L = 3.3\text{mm}$ and $\delta_i/W \approx 0.0001\text{mT}^{-1}\mu_0H_0$ for $L = 0.92\text{mm}$. In both cases it is two orders of magnitude lower than the deflection induced by the torque of the permanently magnetic moment. This can be seen for $L = 0.92\text{mm}$ in figure 5.3 by noting that the slope of the line corresponding to the cilium with a permanent moment is higher than that of one with the induced moment⁵.

Apart from this quantitative argument, there is also a qualitative argument that rules out the effect of an induced magnetic moment parallel to the field. The relation between the deflection δ_i of a cilium with an induced moment and the magnetic field \vec{H}_0 can be written as

$$\delta_i \propto \chi \left(\vec{H}_0 \cdot \nabla \right) \vec{H}_0 \propto \frac{\chi}{2} \nabla \left(\vec{H}_0 \right)^2, \quad (5.1)$$

using the product rule for $\nabla(\vec{A} \cdot \vec{B})$. It shows that the deflection is independent of the sign⁶ of the magnetic field. The deflection δ_p of a permanently magnetic cilium is related to the magnetic field by

$$\delta_p \propto \vec{M} \times \vec{H}_0 \quad (5.2)$$

⁴The effect of shape anisotropy on the susceptibility (section 2.2.3) is neglected here; this would only decrease the resulting deflection by a small amount.

⁵Note that the susceptibility used in the graph is 40 times the measured susceptibility, so the slope of the induced moment is even 40 times lower than the graph shows.

⁶“direction” may be the better term, but as the theory assumes that the field is perpendicular to the cilium, “sign” is more appropriate here.

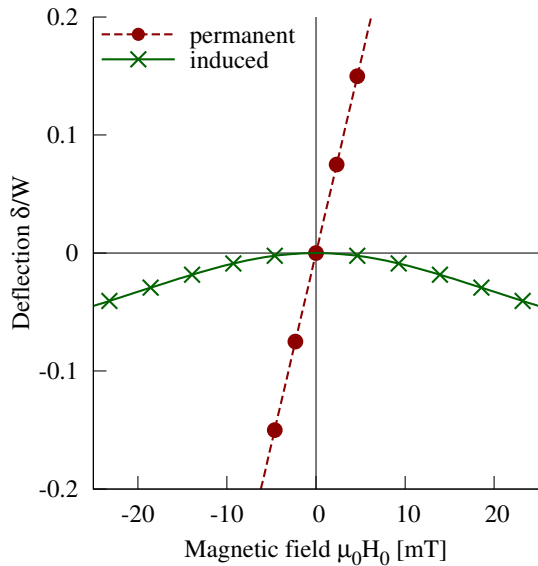


Figure 5.3: Deflection of an artificial cilium in the field of an electromagnet for a permanently magnetic and magnetically induced cilium, obtained by simulations modelled after the macroscopic experiment discussed in the text ($L = 0.92\text{mm}$). It is clear that a permanently magnetic cilium has a deflection that is dependent on field direction, while the induced cilium has a deflection independent of field sign. The permanently magnetic cilium was given a permanent magnetisation of $M_r = 96\text{kA/m}\cdot\text{vol}\%$ (the value from VSM measurements), and the induced cilium a susceptibility $\chi = 196\cdot\text{vol}\%$ (40 times the value from VSM measurements, to enhance readability of the graph). Note that deflection by an induced moment is caused by a gradient force (δ_i , equation 2.5) as well as an induced torque ($\delta_{i,\tau}$, equation 2.11).

with \vec{M} in a fixed direction, so it is dependent on the sign of H_0 . This difference in behaviour can also be recognised in figure 5.3. It shows again that the deflection in the experiments is not caused by an induced moment⁷.

Because of shape anisotropy, a magnetically induced moment can also have a component perpendicular to the magnetic field, creating a magnetically induced torque. The resulting deflection $\delta_{i,\tau}$

⁷This has also been verified experimentally by using a nickel-PDMS composite, which is softly ferromagnetic and has a negligible remanent field. Using the same setup as here, the direction of deflection was found to be independent of field direction and dependent on field gradient.

has an upper bound as specified by equation 2.11, discussed in section 2.2.3. Since $\delta_{i,\tau} \propto |\vec{H}_0|^2 \sin 2\alpha$, with α the angle between the field and the cilium, it only becomes relevant at angles close to 45° . For the experiment with $L = 3.3\text{mm}$ at $H_0 = 50\text{mT}$, $\alpha = 76^\circ$ and so with $\delta_{i,\tau}/W < 4.1$ this effect is present but not dominating (although it would at higher fields or angles). The experiment with $L = 0.92\text{mm}$ has $\alpha \approx 85^\circ$, so $\delta_{i,\tau}/W < 0.12$ at $H_0 = 100\text{mT}$ which is negligible.

5.1.2 The coercive field

The field at which the experiments were done exceeds the coercive field $H_c = 17.5\text{mT}$ as was measured by VSM (section 3.4.2.1). This contradicts the condition put forward in section 2.3.4 that the actuating field must remain lower. If the external field would indeed destroy the remanent magnetisation by forcing it into the direction of the field, the magnetic moment would be completely induced. However, the previous section has shown both quantitatively and qualitatively that this can not be the case, so a permanent moment must have remained despite the external field exceeding H_c .

The fact that the angle α between the cilium's remanent magnetisation and the external field (figure 2.5 on page 16) is somewhere between perpendicular and parallel may explain this. At small deflections, the cilium is mostly perpendicular to the field. The coercive field for this perpendicular situation can be different from the anti-parallel coercive field; only the latter was measured by VSM as H_c . Stoner-Wohlfarth theory (section A.2 on page 60) may suggest that the coercive field can only become smaller for non-anti-parallel angles, but ferromagnetic materials can be bound to other behaviour. [16, 19, 98] mention that for a ferromagnetic material whose magnetic behaviour is determined by domain-wall pinning, the coercive field can be governed by a $1/\cos \alpha$ relationship⁸; only the field projection parallel to the magnetisation contributes to

⁸This is in the limit that $H_c \ll H_A$ [19], with the anisotropy field $H_A = \frac{2K}{\mu_0 M_s}$, where K is the anisotropy constant (see also section A.2 and [30, §1.1.3.4]). As an estimation, H_A can be evaluated using the anisotropy constant for iron (table A.2) and the measured saturation magnetisation of iron inside the nanoparticles (section 3.4.2.1), which results in $H_A = 95\text{kA/m} = 120\text{mT}$. Since $H_c \ll H_A$, this behaviour may indeed be present in the Fe@C nanoparticles.

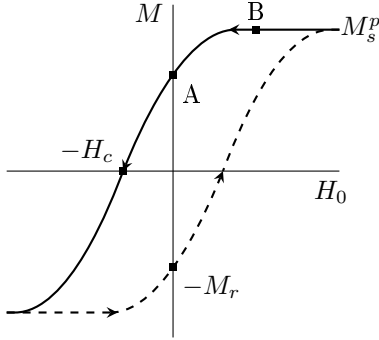


Figure 5.4: Magnetisation curve of a permanently magnetic material. It shows how a permanently magnetic material responds to an applied magnetic field H_0 by changing its magnetisation M . The saturation magnetisation M_s^p , coercive field H_c , and remanent magnetisation M_r are indicated. Note that the magnetisation curves are symmetric, and H_c and M_r are defined as positive quantities. See also figure 2.6 on page 19.

to the coercive field from the demagnetising field. Since the field experienced by the Fe@C particles $H_i = H_0 - \mathcal{N}M$ is smaller than the external field H_0 , the latter can exceed the coercive field while the magnetisation is retained. Only when $H_i = H_c$ do the particles rotate their magnetisation. So the effective coercive field is $H_{c,\text{eff}} = \{H_0 \mid H_i = H_c\} = H_c + \mathcal{N}M \approx H_c + \mathcal{N}M_r$. With $\mathcal{N} \approx 0.9$ this becomes $H_{c,\text{eff}} = H_c + 0.11\text{T} \cdot \text{vol}\%$ for Fe@C, which would mean an increase of 2.4mT for a 2.2vol% composite sample; a small contribution indeed.

rotation of the magnetisation[30, §3.3.5.1]. While this behaviour is of course a simplification — an infinite coercivity at $\alpha = 90^\circ$ is highly unlikely — the perpendicular coercive field can be an order of magnitude higher than the parallel⁹ coercive field, as computed in [19], for example. When applied to the permanently magnetic cilium, $\alpha \approx 90^\circ$ at small deflections, and the coercive field can be much higher than measured by parallel⁹ VSM measurements.

When deflection becomes significant, the bending of the cilium starts to play a role so that the angle α between the cilium's permanent magnetisation and the external field decreases. This results in a magnetic field with a component parallel to the cilium's magnetisation. This component follows the magnetisation curve as measured by VSM, shown schematically in figure 5.4. As α decreases from 90° towards zero, the external field parallel to the cilium increases. This corresponds to a movement from point A (field perpendicular to magnetisation) to point B. When the external field is removed again, the solid curve is followed to point A, so the original remanent magnetisation remains.

Apart from this, there is a small contribution

⁹'Anti-parallel' might be technically more correct, but possibly somewhat confusing.

this page was almost left blank to keep the following pages together

5.2 Small

A smaller feasibility prototype was created using the fabrication method described in chapter 4. It was created by spin-coating the photoresist ma-N 1420 at 350rpm for 30s on a clean glass substrate. This was baked on a hotplate at 120°C for 5½ minutes, UV-exposed for 150s and developed for 5 minutes in m-D 533 and finally rinsed with demi-water, resulting in a layer of about 8µm. Then the sample was covered with PVA (8.7% of weight in demi-water), spin-coating at 500rpm for 30s and baking on a hotplate at 100°C for 2 minutes. The photoresist was subsequently dissolved in acetone in an ultrasound bath for 5 minutes. Thereafter, an 1.6vol% Fe@C-s-PDMS composite was created and spin-coated on the sample at 3000rpm for 30s. It was UV-exposed in a nitrogen environment for 30s to create the beam structures, post-exposure baked on a hotplate at 120°C for 15 minutes¹⁰, developed in xylene for 40s, flushed in isopropanol (IPA) and blow-dried with nitrogen. Finally, the sacrificial layer was dissolved by putting the sample in demi-water. From this point on, it was important to keep the sample in a liquid, to prevent the cilia from getting stuck to the substrate because of surface tension forces during drying.

from sticking to the substrate by surface tension when drying. The demi-water was gradually replaced by IPA to make sure that the sample remained inside the liquid; the hydrophobic PDMS may have popped out of the fluid otherwise. Then the cilia were observed with a microscope as shown in figure 5.5a.

The micrograph shows the cilium free from the surface at the left. Slightly right from the centre, a vertical line marks the boundary where the sacrificial layer once was; at its left, the PDMS is free, while at its right it is fixed to the surface. The triangular pieces above and below the flap are residues of PDMS that remained despite not being UV-exposed. They are so thin, however, that they have no substantial effect. This can be seen clearly by a scanning electron micrographs (SEM)

¹⁰This step is not mentioned in chapter 4 but it happens that this specific sample has had the treatment; skipping the post-exposure bake should not make any noticeable difference. Except, possibly, for an increase in resolution because of the DMPAP radicals have less time to diffuse without the baking step.

of figure 5.6. The images also show that the homogeneity of Fe@C particles in the cilium is not very good; large clusters are present, much larger than found in chapter 3; this is probably the cause of the irregular thickness, which can be seen very clearly in the SEM pictures.

To quantify the motile response of this cilium, its dimensions have been estimated to be $L \approx 250\mu\text{m}$, $T \approx 150\mu\text{m}$ and $W \approx 10\mu\text{m}$; there are no hard edges, so the error is several micrometres. When the cilium was put in the magnetic field of a rare-earth permanent magnet at a distance where the field is about 50mT, there was a large deflection as shown in figure 5.5b, estimated¹¹ to be $\delta \approx 183\mu\text{m}$. When computing the magnetisation of the Fe@C particles that would be needed for such a deflection by a torque, it gives $M = 183\text{kA/m}$, about twice the remanent field of the Fe@C particles as measured by VSM ($M_r = 96\text{kA/m}$). Note that the uncertainty is more than 50%, because of the large error in the measurement of W .

The deflection by an induced moment perpendicular to the cilium can be ruled out because the deflection is dependent on the magnetic field direction; turning the magnet by 180° to change the poles made the cilium bend downwards instead of upwards. With a magnetic field gradient below 20T/m at the distance of the cilium as determined by simulations on the permanent magnet, the maximum deflection for this would be $\delta_i/W \approx 0.002\text{mT}^{-1} \mu_0 H_0 \approx 0.1$, which is negligible.

An induced moment parallel to the cilium may have an impact, though, since the deflection is so large that $|\sin 2\alpha| \rightarrow 1$. With $\alpha \approx 54^\circ$, still $\delta_{i,\tau}/W < 0.5$ at $H_0 = 50\text{mT}$, so this is no substantial effect either.

Conclusion is that a permanently magnetic moment parallel to the cilium must be the cause of the deflection. The magnetisation required for deflection is higher than expected, although the uncertainty is more than 50%; if the height would be $W = 7\mu\text{m}$ (instead of $10\mu\text{m}$), the required magnetisation would already be $M = 90\text{kA/m}$. The difference could also be caused by the Young's modulus being a factor of two lower than predicted because the cilium is drenched in IPA, which swells

¹¹Assuming that the shape of the deflected cilium is parabolic, one can obtain the deflection δ from the projected length in figure 5.5b.

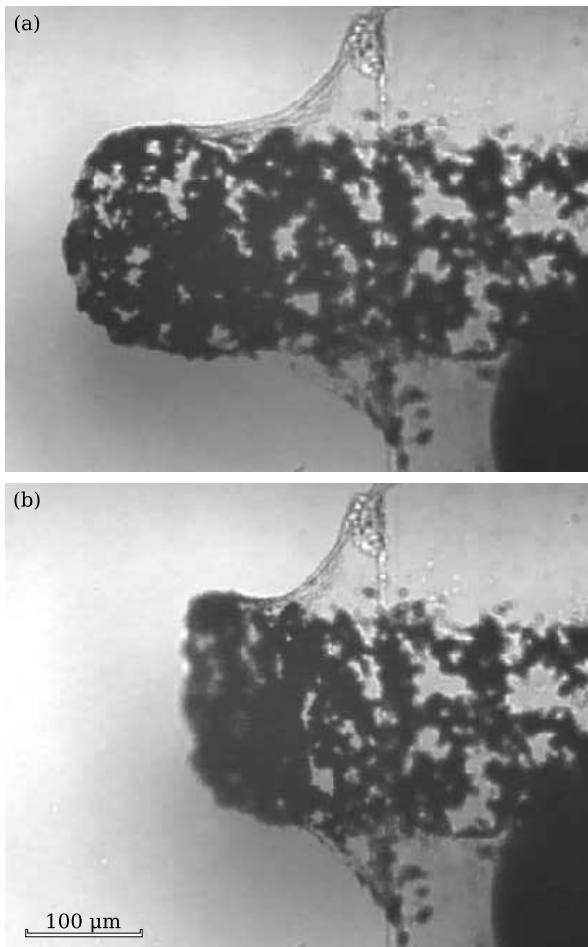


Figure 5.5: Optical micrograph of a micro-fabricated artificial cilium in IPA, (a) in rest without an external field as well as (b) in an external magnetic field of about 50mT, more or less perpendicular to the cilium.

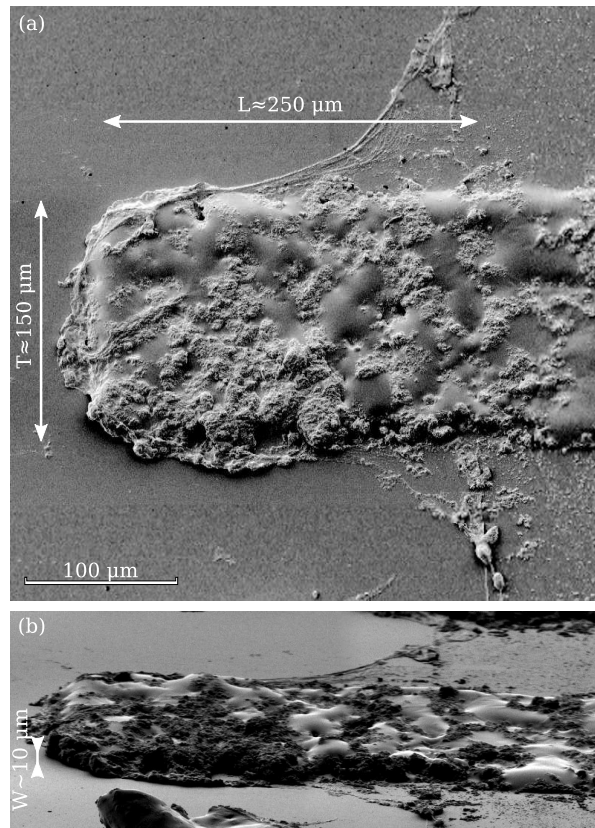


Figure 5.6: Scanning electron microscope images of a micro-fabricated artificial cilium (same as figure 5.5). The cilium has an inhomogeneous distribution of Fe@C particles inside. (a) is a top view (stitched together from images with different resolutions), while (b) is taken under an angle of 70° . The thickness is estimated to be about $W \approx 10\mu\text{m}$, but has considerable variations over the surface.

PDMS[48] and may reduce its modulus. Furthermore, there are no measurements of s-PDMS with magnetic particles inside, so the actual elasticity may be different from the plain s-PDMS.¹²

¹²While the presence of particles may reduce cross-linking and decrease the modulus, interaction of the permanently magnetic particles can also increase it. The amount of DM-PAP used also affects the amount of cross-links made, so it is likely to affect the modulus too (just as the amount of curing agent in Sylgard-184 PDMS determines the resulting elasticity).

5.2.1 Very long cilia

While the micro-fabricated cilium just discussed was long enough to show a considerable deflection, much longer cilia were created too. Although their behaviour was not thoroughly investigated, some general remarks can be made. Microscope images of such a sample are shown in figure 5.7. Actuation was done by moving a rare-earth permanent magnet underneath the sample, generating a field of about 50mT.

The images show that longer cilia do not remain flat, but have a tendency to be bent in rest as well as in a magnetic field. Part of this could be a result of the photo-lithographic procedure, where particles inside the PDMS interact with UV light so that the bottom is cross-linked less than the top¹³. When a magnetic field is applied, the cilia start to twist around their axes. Apparently it is more favourable to align their magnetic moment with the second-longest axis by twisting, than to align it against the length of the cilium by deflecting. The latter would magnetically be favourable (lower demagnetisation), but cost more mechanical energy. A small upward movement like with the shorter cilia has been observed too, though.

In figure 5.7b it can be recognised that the most right cilium displays little movement. This is one among others that were stuck to the surface, mostly at the upper end. By repeated magnetic actuation, some came loose. This confirms that the fabrication procedure needs work to reliably create artificial cilia. This fine-tuning is outside the scope of this work, however, as the proof of principle has been demonstrated.

Neighbouring cilia attract each other magnetically when their distance is short. This can be seen in figure 5.7a by the left four cilia clumping together at the end. The actuating field was strong enough to overcome this interaction, however.

5.3 Conclusion

Artificial cilia have been created with a width of $W = 66\mu\text{m}$ and $W \approx 10\mu\text{m}$. All cilia show movement when actuated with an external field of about

¹³This might be solved by UV-exposing the sample again for a long time after development (flood-exposure). This must be done before dissolving the sacrificial layer, since at that moment the cilia come loose and get their bent shape.

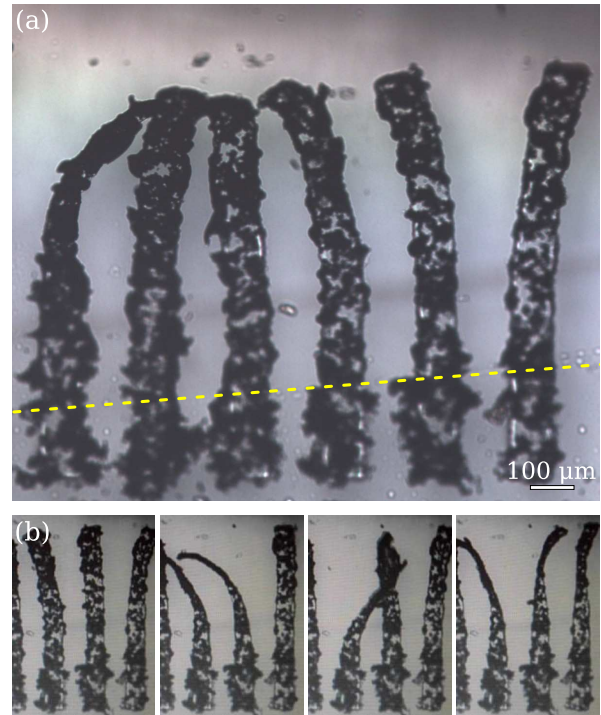


Figure 5.7: Microscope images of micro-fabricated artificial cilia with a high aspect-ratio. (a) shows the sample in zero field. The yellow dashed line indicates the boundary where the sacrificial layer was: the part of the cilia above it is free, the part below is attached to the surface. (b) shows several images of the most right three cilia under application of a mostly perpendicular magnetic field. By moving the magnet underneath and varying the angle, cilia could be made to move.

50mT. The relation between the field and deflection is linear, as predicted by theory. The actuating field exceeded the coercive field, but it has been argued that this does not adversely affect the performance. The cilia's movement has been shown to be caused by a permanently magnetic moment, and the magnetisation required for the deflection measured has the same order of magnitude as the remanent field measured by VSM. Cilia with an aspect-ratio over 50 have been found to twist rather than deflect.

All in all, it appears that magnetic actuation of artificial cilia with a permanently magnetic material is feasible, and their behaviour can be characterised by the theory presented in chapter 2.

Chapter 6

Conclusion & outlook

6.1 Conclusion

Cilia in nature are found to induce mixing and pumping. The same principle can be used to achieve such in the domain of microfluidics. By moving thin, long structures inside a fluid, motion is induced. Magnetically induced motion of artificial cilia created from a magnetic PDMS composite was analysed in theory and practise. Two configurations were considered: a cilium with an induced magnetic moment in the magnetic field of a current wire, and a permanently magnetic cilium in the homogeneous field of a magnet. An estimation of the resulting cilia movement favoured the permanently magnetic cilium, which could achieve a greater deflection than the induced cilium and whose behaviour was independent of scaling. Both showed a p^3 -dependence on aspect-ratio.

A permanently magnetic PDMS composite was created using Sylgard-184 PDMS and Fe@C particles with a diameter of 70nm. The maximum volume concentration that could be achieved was 3vol%, with particle clusters appearing up to a diameter of $10\mu\text{m}$. The magnetic behaviour of Fe@C-doped-PDMS was measured by VSM and appeared to be independent of concentration, with which the saturation magnetisation M_s , remanent field M_r and susceptibility χ scaled linearly. Extrapolating the measurements to a 100vol% Fe@C-PDMS composite resulted in $M_s = 0.6\text{MA/m}$, $M_r = 0.16M_s$ and $\chi \approx 5$. The coercive field was measured at $H_c = 17.5\text{mT}$. While these values are smaller than was expected from iron, it was still suitable for use in a feasibility prototype. Field-curing of the composite did not substantially enhance its magnetic properties.

To obtain high aspect-ratio micro-structures, ar-

tificial cilia were created in a horizontal fashion using a sacrificial layer lift-off technique. To shape PDMS, it was made photosensitive so it could be processed by photo-lithography. Two options were explored: photoPDMS and s-PDMS, of which the latter was selected because of the better resolution and selectivity. This resulted in a resolution of $30\mu\text{m}$ for plain s-PDMS and about $130\mu\text{m}$ for s-PDMS with 8wt% of Fe@C particles inside, although the latter may likely be improved by optimisation of the fabrication parameters.

Finally feasibility prototypes of permanently magnetic artificial cilia were created. A macroscopic experiment was done by cutting a slab out of Sylgard-184 Fe@C-PDMS. The deflection was linear with field strength, as predicted by theory, and in the same order of magnitude as expected from order-of-magnitude calculations. Although the actuating field exceeded the coercive field as measured by VSM, this didn't seem to remove the remanent magnetisation. Ferromagnetic domain theory was able to give a possible explanation for this.

A micro-fabricated artificial cilium with an aspect ratio of 18 was found to show a considerable deflection in a 50mT field, in the same order-of-magnitude as calculated from theory and VSM measurements. Micro-fabricated cilia with much larger aspect ratios were found to twist rather than bend and showed interaction between different cilia.

Concluding, magnetic actuation of permanently magnetic artificial cilia is feasible, and the order of magnitude of their behaviour can be described by the theory presented.

6.2 Outlook

Now that permanently magnetic artificial cilia have been shown to bend under application of a magnetic field, their use can be applied to the domain of microfluidics. This requires multiple cilia to be fabricated in parallel inside a microfluidic channel. Because of swelling of large patches of PDMS during development (section 4.1.2.3), the lay-out of the photo-mask is important for a reliable fabrication process. Also the aspect-ratio and spacing between cilia need to be chosen carefully to avoid interaction (section 5.2.1).

While the fabrication of magnetic photosensitive PDMS as discussed in section 4.2 yielded acceptable results, the influence of magnetic particles with respect to UV-exposure and development, as well as the attainable resolution, would need to be investigated to obtain optimal and better reproducible results.

The performance of the cilia can be increased by improvement of magnetic properties, like an increase of the particle concentration. While Sylgard-184 had a maximum concentration of 3vol% Fe@C particles (section 3.4), s-PDMS follows a different cross-linking mechanism allowing for higher concentrations. Homogeneous dispersion of the particles would still be an issue, though; the use of a surfactant may be able to improve this.

While iron nanoparticles were used because of their commercial availability, rare-earth magnetic materials would be preferable. There are reports of rare-earth nanoparticles $< 1\mu\text{m}$ with superior magnetic properties [89], although this usually involves custom milling or synthesis.

When the details of cilia fabrication are in control, focus will be shifted to obtaining useful microfluidic interaction. Multiple cilia need to be actuated in such a way, that mixing or pumping is induced, requiring asymmetry [94]. One way would be to combine the behaviour of the magnetically induced and permanent cilium: while the permanent moment of artificial cilia makes them deflect in an external field, the induced moment (also present in a permanently magnetic cilium) could be exploited to achieve additional local actuation by a current wire when positioned correctly. Another way would be to apply a rotating magnetic field, by which an asymmetric movement can be induced for pumping, for example.

Acknowledgements

This work wouldn't have been possible without the help of others. First of all, I'd like to thank Francis Fahrni, my direct supervisor and Ph.D. student on the larger project about polymer MEMS. His patience during the explanation of all those basic theoretical and experimental things that one needs to grasp; the insightful and knowledgeable remarks that were granted from an always open door. You have been invaluable.

Leo van IJzendoorn was my other supervisor. His eye was watching steadily from the sideline, not failing to question and to elucidate at the appropriate time. His remarks and discussions were helpful and brought understanding.

The group "Molecular biosensors for medical diagnostics" (MBx) where I have spent a year deserves a word of thanks for the friendly atmosphere and for their company; the discussions that took place at the weekly meeting and elsewhere have not failed to bring new ideas, and gave me an opportunity to present and discuss my progress. The inter-disciplinary PolyMEMS meetings were always interesting and stimulating and did not lack knowledgeable people.

I'd like to thank Casper van Oosten for the use of his facilities at the chemical laboratories, and Klara Maturova for the use of the nitrogen glove-box. Also the sponsoring of Dutch Polymer Institute (DPI) project #532 is acknowledged. The department of applied physics is thanked for their financial support.

Finally, Arthur de Jong is complimented for his keen eye in spotting the Remaining Error.

Appendix A

Critical diameters in nano-magnetism

The permanently magnetic composite used in this work was created by suspending permanently magnetic nanoparticles in a polymer matrix. For the selection of nanoparticles, it is important to know the influence of particle size on their magnetic properties. This is treated in the current appendix.

When (ferro)magnetic particles have a size in the order of nanometres, magnetic behaviour may be quite different than from bulk. The apparent saturation magnetisation, for example, can become an order of magnitude lower. Around 1950, there still was doubt among physicists about the exact origins of this effect[5], but since then many experiments have shaped and confirmed present theory. This appendix provides an introduction to the physics at a nanometre scale, and derives some critical diameters. A more thorough treatment of the theory is given by many textbooks: [11, 30, 47] among others. One noteworthy article is [3] by Kittel.

A.1 Single- and multi-domain particles

A permanent magnet creates a magnetic field in space, which carries energy. This energy can be

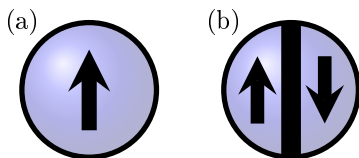


Figure A.1: Magnetisation of (a) a single domain particle, and (b) the simplest multi-domain particle.

minimised by creating oppositely facing domains in the material, so that the external field is decreased. The boundary between domains carries energy, but for larger particles this is less than the energy benefit obtained. When the dimensions of a magnetic particle get close to the domain wall size, it may be more energetically favourable for the particle to form a single domain.

The critical size between a single- or multi-domain particle can be estimated by considering the two situations depicted in figure A.1. The energy of single-domain particle (a) has the magnetostatic energy of a spherical particle with radius R , saturation magnetisation M_s and demagnetisation factor \mathcal{N} (section 2.2.3):

$$E_{sd} = \frac{1}{2}\mu_0\mathcal{N}M_s^2 \cdot \frac{4}{3}\pi R^3. \quad (\text{A.1})$$

The two-domain particle (b) includes the energy of a domain wall:

$$E_{md} = \gamma\pi R^2 + \alpha\frac{1}{2}\mu_0\mathcal{N}M_s^2 \cdot \frac{4}{3}\pi R^3, \quad (\text{A.2})$$

with γ the domain wall energy per surface area. The exact magnetostatic energy of a two-domain particle is not easily derivable, therefore it is written as a fraction α of the single-domain case. Since the two-domain particle has a lower stray field, the magnetostatic two-domain energy is less than the single-domain energy and $\alpha < 1$. It is obvious that $\alpha > 0$. Several textbooks take α to be $\frac{1}{2}$, which is followed here [11, 30, 47].

The critical domain diameter D_{do} is found when the energies of the single- and multi-domain config-

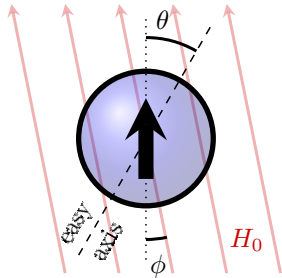


Figure A.2: A spherical particle in an external field H_0 with one anisotropy axis. The angle between the particle's magnetisation and the external field is ϕ and the angle between the particle's magnetisation and its anisotropy axis is θ .

urations are equal, $E_{sd} = E_{md}$. This results in

$$D_{do} = 2R_{do} = \frac{6\gamma}{2(1-\alpha)\mu_0\mathcal{N}M_s^2} = \frac{18\gamma}{\mu_0M_s^2}. \quad (\text{A.3})$$

Spherical particles with a diameter below D_{do} consist of a single magnetic domain, larger particles consist of multiple domains.

A.2 Homogeneous rotation

A typical single domain particle will have all its spins pointing in the same direction. When an external magnetic field is applied, these spins rotate in unison to become parallel to the field and minimise the Zeeman energy. This behaviour is also termed coherent or homogeneous rotation.

A particle may, however, have a preferential direction for its magnetisation. This magnetic anisotropy creates an energy barrier, which can prohibit the magnetisation from following the external field perfectly. The anisotropy may be due to particle shape, crystal structure, or mechanical tension¹.

To rotate the magnetisation, this anisotropy barrier needs to be overcome. Stoner-Wohlfarth theory[2] describes this for a particle with a single anisotropy axis.

Consider a spherical particle with one easy axis in an external field, as sketched in figure A.2. ϕ is

¹To be complete, exchange anisotropy (discovered in 1957) should be mentioned here too.

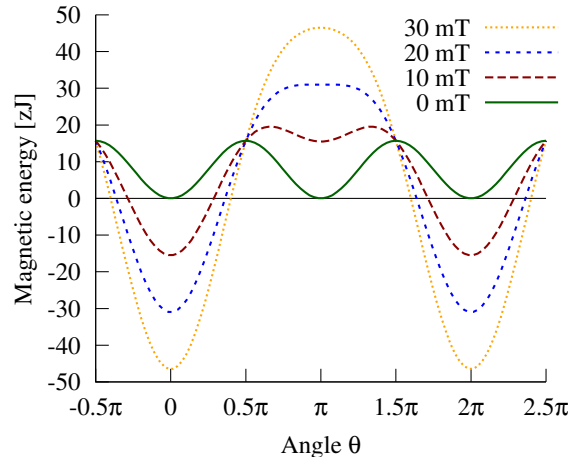


Figure A.3: Stoner-Wohlfarth energy of a particle as a function the angle θ between its magnetisation and anisotropy axis, for different external field strengths. The nickel nanoparticle has a diameter of 20nm and its anisotropy axis parallel to the external magnetic field H_0 (constants used are found in table A.2).

the angle between the particle's magnetisation and the magnetic field H_0 , while θ is the angle between the particle's easy axis and its magnetisation. The magnetic energy of this particle is the sum of the magnetostatic, anisotropy, and Zeeman energy:

$$E_{sw} = V \left[\frac{1}{2}\mu_0\mathcal{N}M_s^2 + K \sin^2\theta - \mu_0H_0M_s \cos\phi \right], \quad (\text{A.4})$$

with K the anisotropy constant and V the particle volume. When the field is (anti-)parallel to the easy axis, the anisotropy barrier is largest: $\theta = \phi$. This situation is plotted for different fields in figure A.3. The two energy minima at $\theta = 0$ and $\theta = \pi$ are along its easy axis. In zero field $H_0 = 0\text{mT}$, both situations have the same energy. When an external field is applied, the Zeeman term increases the energy of a magnetisation anti-parallel with the field. When this energy is lower than the barrier at $\theta = \frac{1}{2}\pi$, there still is a local minimum and particle in that state retains its magnetisation ($H_0 = 10\text{mT}$ in the figure). This minimum disappears at the anisotropy field $H_0 = H_{sw}$, and the particle aligns its magnetisation to the external field.

The anisotropy field H_{sw} can be determined by detecting when the second derivative of the Stoner-

Wohlfarth energy with respect to θ changes sign, $\frac{\partial^2 E_{sw}}{\partial \theta^2} = 0$, resulting in

$$H_{sw} = \frac{2K}{\mu_0 M_s}. \quad (\text{A.5})$$

For the nickel nanoparticle of figure A.3 this results in $H_{sw} = 18\text{mT}$.

A.3 The superparamagnetic limit

When the size of a particle is very small, thermal energy $k_B T$ may be enough to overcome the anisotropy barrier KV . This results in the magnetisation being rotated spontaneously every once in a while. When many particles are considered and no external field is present, the random moments cancel each other and give an average magnetisation of zero. When an external field is present, the randomly fluctuating moments have an average magnetisation parallel to the field². This phenomenon is called superparamagnetism; D_{th} is the diameter below which this occurs, the superparamagnetic limit. The approach of thermally activated switching of a single-domain particle is called the Neel-Brown model.

The average time τ_m it takes for the thermal energy to flip the magnetisation can be expressed using the Arrhenius-Neel law[4]:

$$\tau_m = \tau_0 e^{\frac{KV}{k_B T}}, \quad (\text{A.6})$$

with τ_0 the resonance relaxation time of the spin system, which is generally in the order of 10^{-10}s [7]. This equation can be understood directly by recognising the Boltzmann-factor, although it is possible to derive it from a magnetic energy expression like done in previous paragraphs [30].

For a given time span τ_m , the critical diameter is

$$D_{th} = \sqrt[3]{\frac{6k_B T}{\pi K} \ln \frac{\tau_m}{\tau_0}}; \quad (\text{A.7})$$

a particle of this diameter has a stable magnetisation for a time span of just τ_m . The value taken

²This holds for an ensemble of many particles, but, according to the ergodic hypothesis, also for a single particle averaged over time.

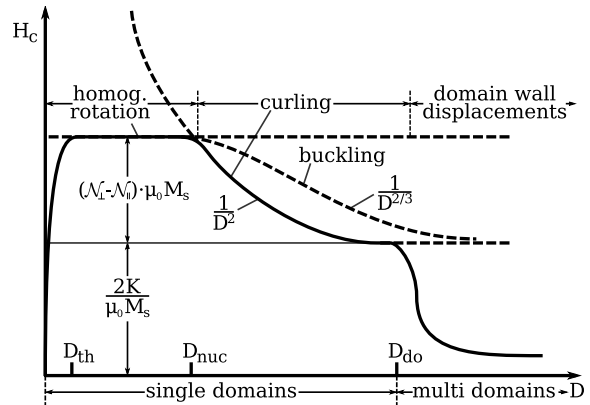


Figure A.4: A schematic graph of the coercive field as a function of diameter. The different size regimes can be recognised. [47]

for τ_m is application dependent. In superparamagnetic particles for biomedical applications, one second is generally appropriate. Hard disks need permanently magnetic areas for storing data and should not be disturbed by thermal processes; a lifetime in the order of tens of years is much more reasonable there.

A.4 The different regimes

So far, we have seen three regimes: multi-domain (bulk, $D > D_{do}$), stable single-domain ($D_{th} < D < D_{do}$), and superparamagnetic ($D < D_{th}$). In figure A.4, the coercive field is shown as a function of size. This is the external field needed to rotate the magnetisation, and a measure for the internal energy. Multi-domain particles decrease the field by forming domains, while single-domain particles have a high coercive field, originating from magnetocrystalline ($2K_1/M_s$) and shape ($(\mathcal{N}_\perp - \mathcal{N}_\parallel) \cdot M_s$) anisotropy. Below the superparamagnetic limit D_{th} , the coercive field decreases because thermal energy is enough to overcome the barrier.

Below the critical domain diameter D_{do} , the energy of a domain wall is too large to reduce the stray field. But there are other options for reduction, besides creating multiple domains. This is what happens in the curling and buckling magnetisation modes: the magnetisation varies continuously over the geometry. The exchange energy re-

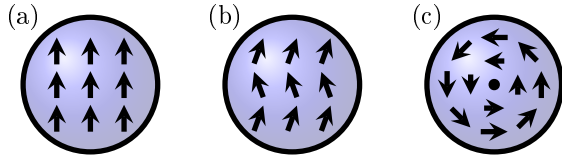


Figure A.5: Magnetisation modes of a single domain: (a) homogeneous rotation, (b) buckling, and (c) curling. The centre of the curling mode is pointing out of (or into) the plane.

sulting from slightly nonparallel spins is kept small, while spins are cancelling each other's field over a larger area. Figure A.5 shows the most basic modes. We have seen homogeneous rotation (a) before, where all spins are parallel. With buckling (b), the magnetisation is homogeneously varying along one direction. In the figure, it is varying upwards; fluctuations to the left and right cancel each other, thereby decreasing the total stray field. Buckling often occurs in thin rods. Similarly, the curling mode reduces the stray field to a minimum by circular symmetry. It has also small exchange energy, but for the centre: there opposed spins are just next to each other, forcing the magnetisation to rotate out of plane. This mode is found primarily in thin disks; the vortex state depicted has a centre magnetisation either into the paper, or out of it.

A.5 Critical diameters for selected materials

For permanently magnetic materials, like nanoparticles in a permanently magnetic cilium, it is desirable to have stable domains with parallel spins. The superparamagnetic regime is unstable, so $D > D_{\text{th}}$ is desired. Individual spins cancel each other in de curling mode, so that is undesirable too. While homogeneous rotation would be preferable because of the high coercive field and magnetisation, it may be hard to achieve in practise, since the theory presented here is no more than a basic estimation. So to be sure of good permanently magnetic properties, the regime of multiple-domains is be preferable.

For some common ferromagnetic materials, critical diameters have been computed in table A.1.

The material properties used there are presented in table A.2.

Figure A.4 may suggest that critical diameters have a natural order of succession, but table A.1 shows that this is not necessarily the case. In iron and nickel, for example, is the limit of homogeneous rotation larger than the single-domain limit, so that no curling or buckling mode exists.

	<i>symbol</i>	<i>expression</i>	Iron	Cobalt	Nickel	Magnetite	Nd ₂ Fe ₁₄ B	<i>units</i>
Single-domain limit	D_{do}	$\frac{3\gamma}{\mathcal{N}(1-\alpha)\mu_0 M_s^2}$	13	68	30	119	219	<i>nm</i>
Limit of homogeneous rotation	D_{nuc}	$3.68 \cdot \sqrt{\frac{2A}{\mathcal{N}\mu_0 M_s^2}}$	22	32	48	57	17	<i>nm</i>
Superparamagnetic limit	D_{th}	$\sqrt[3]{\frac{6k_B T}{\pi K_1} \ln \frac{\tau_m}{\tau_0}}$	19	9	43	32	4	<i>nm</i>
Bloch domain wall width (bulk)	δ_B	$\pi \cdot \sqrt{\frac{A}{K_1}}$	65	26	137	104	4	<i>nm</i>

Table A.1: Critical diameters for selected materials. For comparison, the domain wall width is mentioned too. Note that the formulae are estimations, and the material properties used can differ among sources; the numbers presented here should be treated doubly as estimations only.

	<i>symbol</i>	Iron	Cobalt	Nickel	Magnetite	Nd ₂ Fe ₁₄ B	<i>units</i>	<i>refs</i>
Density	ρ	7.875	8.90	8.912	5.17	7.629	10^3 kg/m^3	
Saturation magnetisation	M_s	1.7	1.4	0.49	0.49	1.28	MA/m	[6, 30]
First crystal anisotropy	K_1	48	453	-4.5	-11	4900	kJ/m^3	[30, 47, 11]
Exchange stiffness	A	21	30	9	12	7.7	pJ/m	[30, 47, 34, 54]
Domain wall energy density	γ	2.6	9.3	0.5	2.0	25	mJ/m^2	[30]
Spin lifetime (application dependent)	τ_m				1		<i>s</i>	
Demagnetisation factor (sphere)	\mathcal{N}				1/3			
Two-domain stray field reduction	α				1/2			

Table A.2: Material properties at room temperature (293K) used for computation of critical diameters. Note that values for crystal anisotropy, exchange stiffness and domain wall energy density can differ across sources; in these cases a more common value has been taken.

Appendix B

Commercially available ferromagnetic micro- and nanoparticles

As discussed in section 2.3.4 and 3.2, permanently magnetic particles were needed for the creation of artificial cilia. Their size should be below a micrometre, as to create a homogeneous composite. This appendix summarises commercially available magnetic particles of the basic ferromagnetic elements: iron, cobalt and nickel. Most available particles are in the range 0 – 100nm. Besides the data shown, mknano sells 1.2 μ m cobalt particles, and NanoAmor sells 200nm, 400nm and 800nm nickel particles; Micron Metals has particles in the micrometer-range.

The following data is based on information found on the suppliers' websites and personal communication. It does not pretend to be a list of all existing suppliers, nor give the full possibilities of each supplier; often, a manufacturer is able to create particles on request, which isn't shown here. Nevertheless, it should be a good overview of current commercial offerings.

The particles selected for use in permanently magnetic artificial cilia are 70nm Fe@C particles from mknano. As explained in section 3.2, the carbon shell can protect against oxidation, and the diameter is far above the superparamagnetic limit of 19nm and consists of multiple domains (table A.1) .

B.1 Iron nanoparticles

Supplier	Material	Available diameters [nm]
NanoAmor	Fe@C	20
NaBond	Fe	25
Iolitec	Fe	25, 100
NanoAmor	Fe	25, 30-60, 60-100
MTI	Fe	50
mknano	Fe@C	70
Argonide	Fe	100

B.2 Cobalt nanoparticles

Supplier	Material	Available diameters [nm]
Strem	Co	10-12
NanoAmor	Co@C	20
NanoAmor	Co	20-50, 28
MTI	Co	28
NaBond	Co	28
Iolitec	Co	28, 100

B.3 Nickel nanoparticles

Supplier	Material	Available diameters [nm]
MTI	Ni	20
NaBond	Ni	20
NanoAmor	Ni	20, 30-60, 60-100
Argonide	Ni	50, 100
Iolitec	Ni	50, 100
mknano	Ni	80
nGimat	Ni	5-120

B.4 Alloy nanoparticles

Supplier	Material	Available diameters [nm]
Strem	FeCo	5-8, 10
NaBond	FeCo	30
NaBond	FeNi	10-30
NanoAmor	FeNi	30-60, 60-100
nGimat	FeNi	5-120

Bibliography

The following references contain a digital object identifier (DOI) where possible. To read the article online, either follow the hyperlink (in the digital version, see page 5), or go to <http://dx.doi.org/> and enter the identifier.

- [1] J. A. Osborn (1945). *Demagnetizing factors of the general ellipsoid*. *Physical Review* 67(11-12):351. doi:10.1103/PhysRev.67.351
- [2] E. C. Stoner and E. P. Wohlfarth (1948). *A mechanism of magnetic hysteresis in heterogeneous alloys*. *Philosophical Transactions of the Royal Society of London. Series A, Mathematical and Physical Sciences* 240(826):599–642. ISSN 0080-4614. <http://links.jstor.org/>
- [3] C. Kittel (1949). *Physical theory of ferromagnetic domains*. *Reviews of Modern Physics* 21(4):541. doi:10.1103/RevModPhys.21.541
- [4] L. Néel (1949). *Influence des fluctuations thermiques sur l'aimantation de grains ferromagnétiques très fins*. *Séance du académie des sciences* 228(8):664–666
- [5] C. Kittel, J. K. Galt, and W. E. Campbell (1950). *Crucial experiment demonstrating single domain property of fine ferromagnetic powders*. *Physical Review* 77(5):725. doi:10.1103/PhysRev.77.725
- [6] R. Bozorth (1951). *Ferromagnetism*. The Bell Telephone Laboratories series. Van Nostrand, London. ISBN 0780310322
- [7] W. Brown (1963). *Thermal fluctuations of a single-domain particle*. *Physical Review* 130(5):1677. doi:10.1103/PhysRev.130.1677
- [8] R. Rikmenspoel (1966). *Elastic properties of the sea urchin sperm flagellum*. *Biophysical Journal* 6(4):471–479. <http://www.biophysj.org/>
- [9] S. A. Baba (1972). *Flexural rigidity and elastic constant of cilia*. *Journal of Experimental Biology* 56(2):459–467. <http://jeb.biologists.org/>
- [10] J. C. Blair, C. R. Fuller, P. B. Ghate, and C. T. Haywood (1972). *Electromigration-induced failures in, and microstructure and resistivity of, sputtered gold films*. *Journal of Applied Physics* 43(2):307–311. doi:10.1063/1.1661112
- [11] B. D. Cullity (1972). *Introduction to Magnetic Materials*. Metallurgy and Materials. Addison-Wesley. ISBN 0201012189
- [12] R. J. Roark (1975). *Formulas for stress and strain*. McGraw-Hill, 5th edn. ISBN 0070530319
- [13] C. Brennen and H. Winet (1977). *Fluid mechanics of propulsion by cilia and flagella*. *Annual Review of Fluid Mechanics* 9(1):339–398. doi:10.1146/annurev.fl.09.010177.002011
- [14] M. Okuno and Y. Hiramoto (1979). *Direct measurements of the stiffness of echinoderm sperm flagella*. *Journal of Experimental Biology* 79(1):235–243. <http://jeb.biologists.org/>
- [15] R. J. Harker (1986). *Elastic energy methods of design analysis*. Elsevier, Amsterdam. ISBN 0-444-01035-1
- [16] D. Givord, P. Tenaud, and T. Viadieu (1988). *Angular dependence of coercivity in sintered magnets*. *Journal of Magnetism and Magnetic Materials* 72(3):247–252. doi:10.1016/0304-8853(88)90218-1
- [17] D.-X. Chen, J. Brug, and R. Goldfarb (1991). *Demagnetizing factors for cylinders*. *IEEE Transactions on Magnetics* 27(4):3601–3619. doi:10.1109/20.102932
- [18] Dow Corning Corporation (1991). *Information about high technology silicone materials*. <http://www.particle.kth.se/~pearce/>
- [19] B. Edwards and D. I. Paul (1995). *Ferromagnetic coercivity and applied field orientation*. *Journal of Magnetism and Magnetic Materials* 147(3):331–340. doi:10.1016/0304-8853(95)00058-5
- [20] J. C. Lötters, W. Olthuis, P. H. Veltink, and P. Bergveld (1996). *Polydimethylsiloxane as an elastic material applied in a capacitive accelerometer*. *Journal of Micromechanics and Microengineering* 6(1):52–54. doi:10.1088/0960-1317/6/1/010
- [21] J. C. Lötters, W. Olthuis, P. H. Veltink, and P. Bergveld (1997). *The mechanical properties of the rubber elastic polymer polydimethylsiloxane for sensor applications*. *Journal of Micromechanics and Microengineering* 7(3):145–147. doi:10.1088/0960-1317/7/3/017
- [22] J. C. Lötters, W. Olthuis, P. H. Veltink, and P. Bergveld (1997). *Polydimethylsiloxane, a photocurable rubberelastic polymer used as spring material in micromechanical sensors*. *Microsystem Technologies* 3(2):64–67. doi:10.1007/s005420050057

- [23] A. Aharoni (1998). *Demagnetizing factors for rectangular ferromagnetic prisms*. Journal of Applied Physics 83(6):3432–3434. doi:10.1063/1.367113
- [24] Aldrich Chemical Co., Inc. (1999). *Aldrich polymer products applicaton & reference information: Free radical initiators*. <http://www.sigmaaldrich.com/>
- [25] D. Armani, C. Liu, N. Aluru, and C. Liu (1999). *Re-configurable fluid circuits by PDMS elastomer micromachining*. pp. 222–227. Orlando, FL, USA. doi:10.1109/MEMSYS.1999.746817
- [26] D. Campbell, K. Beckman, C. Calderon, P. Doolan, R. Moore, A. Ellis, and G. Lisensky (1999). *Replication and compression of surface structures with polydimethylsiloxane elastomer*. Journal of Chemical Education 76(4):537–541. <http://jchemed.chem.wisc.edu/>
- [27] H.-P. Chou, C. Spence, A. Scherer, and S. Quake (1999). *A microfabricated device for sizing and sorting DNA molecules*. Proceedings of the National Academy of Sciences of the United States of America 96(1):11–13. <http://www.pnas.org/content/96/1/11>
- [28] J. Coey (1999). *Permanent magnets*. Wiley Encyclopedia of Electrical and Electronics Engineering doi:10.1002/047134608X.W4506
- [29] L. Lagorce, O. Brand, and M. Allen (1999). *Magnetic microactuators based on polymer magnets*. Journal of Microelectromechanical Systems 8(1):2–9. doi:10.1109/84.749396
- [30] R. Skomski and J. Coey (1999). *Permanent Magnetism*. Studies in Condensed Matter Physics. Taylor & Francis. ISBN 0750304782
- [31] Cost Effective Equipment (2000). *Spin coater theory*. <http://www.brewerscience.com/>
- [32] R. Krupnik (2000). *The speed of a protozoan*. <http://hypertextbook.com/>
- [33] H. Lodish, A. Berk, L. S. Zipursky, P. Matsudaira, D. Baltimore, and J. Darnell (2000). *Cilia and Flagella: Structure and Movement (Chapter 19.4)*. W.H. Freeman and Company, New York, 4th edn. <http://www.ncbi.nlm.nih.gov/>
- [34] A. Michels, J. Weissmüller, A. Wiedenmann, J. S. Pedersen, and J. G. Barker (2000). *Measuring the exchange-stiffness constant of nanocrystalline solids by elastic small-angle neutron scattering*. Philosophical Magazine 80(12):785–792. doi:10.1080/0950083001000180S
- [35] S. R. Quake and A. Scherer (2000). *From micro- to nanofabrication with soft materials*. Science 290(5496):1536–1540. doi:10.1126/science.290.5496.1536
- [36] H. Schmid and B. Michel (2000). *Siloxane polymers for high-resolution, high-accuracy soft lithography*. Macromolecules 33(8):3042–3049. doi:10.1021/ma9820341
- [37] X. Sun, A. Gutierrez, M. J. Yacaman, X. Dong, and S. Jin (2000). *Investigations on magnetic properties and structure for carbon encapsulated nanoparticles of Fe, Co, Ni*. Materials Science and Engineering A 286(1):157–160. doi:10.1016/S0921-5093(00)00628-6
- [38] M. A. Unger, H.-P. Chou, T. Thorsen, A. Scherer, and S. R. Quake (2000). *Monolithic microfabricated valves and pumps by multilayer soft lithography*. Science 288(5463):113–116. doi:10.1126/science.288.5463.113
- [39] Y. M. M.-C. Bélanger (2001). *Hemocompatibility, biocompatibility, inflammatory and in vivo studies of primary reference materials low-density polyethylene and polydimethylsiloxane: A review*. Journal of Biomedical Materials Research 58(5):467–477. doi:10.1002/jbm.1043
- [40] W. C. Jackson, H. D. Tran, M. J. O'Brien, E. Rabinovich, and G. P. Lopez (2001). *Rapid prototyping of active microfluidic components based on magnetically modified elastomeric materials*. Journal of Vacuum Science & Technology B: Microelectronics and Nanometer Structures 19(2):596–599. doi:10.1116/1.1350840
- [41] C. S. Lee, H. Lee, and R. M. Westervelt (2001). *Microelectromagnets for the control of magnetic nanoparticles*. Applied Physics Letters 79(20):3308–3310. doi:10.1063/1.1419049
- [42] T. Baynes (2002). *Analysis of the demagnetisation process and possible alternative magnetic treatments for naval vessels*. Ph.d., University of New South Wales. <http://www.phys.unsw.edu.au/~tmb/>
- [43] K. Kim, S. Park, J.-B. Lee, H. Manohara, Y. Desta, M. Murphy, and C. H. Ahn (2002). *Rapid replication of polymeric and metallic high aspect ratio microstructures using PDMS and LIGA technology*. Microsystem Technologies 9(1):5–10. doi:10.1007/s00542-002-0194-6
- [44] T. H. Schulte, R. L. Bardell, and B. H. Weigl (2002). *Microfluidic technologies in clinical diagnostics*. Clinica Chimica Acta 321(1-2):1–10. doi:10.1016/S0009-8981(02)00093-1
- [45] MEMS-talk mail archive (2002-2006). *Various messages: "Photocurable PDMS" (↔), "photopatternable PDMS" (↔), "Photosensitive PDMS" (↔)*. <https://www.memsnet.org/mems/groups>
- [46] K. Choi and J. Rogers (2003). *A photocurable poly(dimethylsiloxane) chemistry designed for soft lithographic molding and printing in the nanometer regime*. Journal of the American Chemical Society 125(14):4060–4061. doi:10.1021/ja029973k
- [47] H. Kronmüller and M. Fähnle (2003). *Micromagnetism and the Microstructure of Ferromagnetic Solids*. Cambridge University Press. ISBN 0521331358
- [48] J. Lee, C. Park, and G. Whitesides (2003). *Solvent compatibility of poly(dimethylsiloxane)-based microfluidic devices*. Analytical Chemistry 75(23):6544–6554. doi:10.1021/ac0346712
- [49] A. R. Wheeler, W. R. Throdsset, R. J. Whelan, A. M. Leach, R. N. Zare, Y. H. Liao, K. Farrell, I. D. Manger, and A. Daridon (2003). *Microfluidic device for single-cell analysis*. Analytical Chemistry 75(14):3581–3586. doi:10.1021/ac0340758
- [50] V. A. Yardley (2003). *Magnetic detection of microstructural change in power plant steels*. Ph.d., University of Cambridge. <http://www.msm.cam.ac.uk/>

- [51] C. Ahn, J.-W. Choi, G. Beaucage, J. Nevin, J.-B. Lee, A. Puntambekar, and J. Lee (2004). *Disposable smart lab on a chip for point-of-care clinical diagnostics*. Proceedings of the IEEE 92(1):154–173. doi:10.1109/JPROC.2003.820548
- [52] P. Gould (2004). *Nanoparticles probe biosystems*. Materials Today 7(2):36–43. doi:10.1016/S1369-7021(04)00082-3
- [53] D. J. Laser and J. G. Santiago (2004). *A review of micropumps*. Journal of Micromechanics and Microengineering 14(6):R35–R64. doi:10.1088/0960-1317/14/6/R01
- [54] M. Ma, Y. Wu, J. Zhou, Y. Sun, Y. Zhang, and N. Gu (2004). *Size dependence of specific power absorption of Fe₃O₄ particles in AC magnetic field*. Journal of Magnetism and Magnetic Materials 268(1-2):33–39. doi:10.1016/S0304-8853(03)00426-8
- [55] Micro Resist Technology GmbH (2004). *ma-N 400 and ma-N 1400 photoresists - technology for lift-off process*. <http://www.nanophys.kth.se/>
- [56] D. Wheatley (2004). *Primary cilia: new perspectives*. Cell Biology International 28(2):75–77. doi:10.1016/j.cellbi.2003.11.005
- [57] C. Yamahata and M. Gijs (2004). *Plastic micropumps using ferrofluid and magnetic membrane actuation*. pp. 458–461. doi:10.1109/MEMS.2004.1290621
- [58] W. Zhang, G. Ferguson, and S. Tatic-Lucic (2004). *Elastomer-supported cold welding for room temperature wafer-level bonding*. pp. 741–744. doi:10.1109/MEMS.2004.1290691
- [59] F. K. Balagadde, L. You, C. L. Hansen, F. H. Arnold, and S. R. Quake (2005). *Long-term monitoring of bacteria undergoing programmed population control in a microchemostat*. Science 309(5731):137–140. doi:10.1126/science.1109173
- [60] Y. Hirai, T. Yoshikawa, M. Morimatsu, M. Nakajima, and H. Kawata (2005). *Fine pattern transfer by nanocasting lithography*. Microelectronic Engineering 78-79:641–646. doi:10.1016/j.mee.2004.12.080
- [61] G. Matthews (2005). *Pond life photomicrographs: Protozoa*. [Online; accessed 16-May-2008]. <http://www.gpmatthews.nildram.co.uk/>
- [62] Micro Resist Technology GmbH (2005). *Negative tone photoresist series ma-N 1400 - processing guidelines*. <http://www.nanophys.kth.se/>
- [63] K. Norrman, A. Ghanbari-Siahkali, and N. B. Larsen (2005). *Studies of spin-coated polymer films*. Annual Reports Section "C" (Physical Chemistry) 101:174–201. doi:10.1039/b408857n
- [64] G. J. Schmitz, C. Brückner, and P. Jacobs (2005). *Manufacture of high-aspect-ratio micro-hair sensor arrays*. Journal of Micromechanics and Microengineering 15(10):1904–1910. doi:10.1088/0960-1317/15/10/016
- [65] T. M. Squires and S. R. Quake (2005). *Microfluidics: Fluid physics at the nanoliter scale*. Reviews of Modern Physics 77(3):977–1027. doi:10.1103/RevModPhys.77.977
- [66] C. Yamahata, F. Lacharme, and M. A. Gijs (2005). *Glass valveless micropump using electromagnetic actuation*. Microelectronic Engineering 78-79:132–137. doi:10.1016/j.mee.2004.12.018
- [67] C. Yamahata, C. Lotto, E. Al-Assaf, and M. A. M. Gijs (2005). *A PMMA valveless micropump using electromagnetic actuation*. Microfluidics and Nanofluidics 1(3):197–207. doi:10.1007/s10404-004-0007-6
- [68] F. Li, S. Zhou, B. You, and L. Wu (2006). *Kinetic investigations on the UV-induced photopolymerization of nanocomposites by FTIR spectroscopy*. Journal of Applied Polymer Science 99(4):1429–1436. doi:10.1002/app.22629
- [69] J. Nagel, G. Mikhail, H. Noh, and J. Koo (2006). *Magnetically actuated micropumps using an Fe-PDMS composite membrane*. Proceedings of SPIE, the International Society for Optical Engineering 6172(1):617213–617222. doi:10.1117/12.658012
- [70] J.-H. Nam, J. R. Cotton, E. H. Peterson, and W. Grant (2006). *Mechanical properties and consequences of stereocilia and extracellular links in vestibular hair bundles*. Biophysical Journal 90(8):2786–2795. doi:10.1529/biophysj.105.066027
- [71] K. W. Oh and C. H. Ahn (2006). *A review of microvalves*. Journal of Micromechanics and Microengineering 16(5):R13–R39. doi:10.1088/0960-1317/16/5/R01
- [72] D. Orenstein (2006). *'Microfluidic' chips may accelerate biomedical research*. Stanford Report <http://news-service.stanford.edu/>
- [73] N. Pamme (2006). *Magnetism and microfluidics*. Lab on a Chip 6(1):24–38. doi:10.1039/b513005k
- [74] G. M. Whitesides (2006). *The origins and the future of microfluidics*. Nature 442(7101):368–373. doi:10.1038/nature05058
- [75] A. A. S. Bhagat, P. Jothimuthu, and I. Papautsky (2007). *Photodefinable polydimethylsiloxane (PDMS) for rapid lab-on-a-chip prototyping*. Lab on a Chip 7(9):1192–1197. doi:10.1039/b704946c
- [76] A. A. S. Bhagat, P. Jothimuthu, and I. Papautsky (2007). *Photosensitive poly(dimethylsiloxane) (photodms) for rapid and simple polymer fabrication*. pp. 537–540. doi:10.1109/SENSOR.2007.4300186
- [77] Dow Corning Corporation (2007). *Sylgard® 184 silicone elastomer, solar product information*. <http://www.dowcorning.com/>
- [78] B. Evans, A. Shields, R. Carroll, S. Washburn, M. Falvo, and R. Superfine (2007). *Magnetically actuated nanorod arrays as biomimetic cilia*. Nano Letters 7(5):1428–1434. doi:10.1021/nl070190c
- [79] Gaspar, Piyasena, Daroczi, and Gomez (2007). *Magnetically controlled valve for flow manipulation in polymer microfluidic devices*. Microfluidics and Nanofluidics doi:10.1007/s10404-007-0204-1
- [80] J. Green, A. E. Holdo, and A. Khan (2007). *A review of passive and active mixing systems in microfluidic devices*. The International Journal of Multiphysics 1(1):1–32. doi:10.1260/175095407780130544

- [81] M. Hermans (2007). *Construction of individual addressable PDMS slabs for microfluidic mixing*. Internship report, Technische Universiteit Eindhoven
- [82] V. V. Khatavkar, P. D. Anderson, J. M. J. den Toonder, and H. E. H. Meijer (2007). *Active micromixer based on artificial cilia*. *Physics of Fluids* 19(8):083605–13. doi:10.1063/1.2762206
- [83] X. Liang, A. Liu, C. Lim, T. Ayi, and P. Yap (2007). *Determining refractive index of single living cell using an integrated microchip*. *Sensors and Actuators A: Physical* 133(2):349–354. doi:10.1016/j.sna.2006.06.045
- [84] D. R. Lide (ed.) (2007). *CRC Handbook of Chemistry and Physics, Internet Version*. Taylor and Francis, Boca Raton, FL, USA, 87th edn. <http://www.hbcnpnetbase.com/>
- [85] Magnetic Component Engineering (2007). *About coercivity and intrinsic coercivity*. <http://www.mceproducts.com/>
- [86] F. M. Sasoglu, A. J. Bohl, and B. E. Layton (2007). *Design and microfabrication of a high-aspect-ratio PDMS microbeam array for parallel nanonewton force measurement and protein printing*. *Journal of Micromechanics and Microengineering* 17(3):623–632. doi:10.1088/0960-1317/17/3/027
- [87] S. Smith, T. Tang, J. Terry, J. Stevenson, B. Flynn, H. Reekie, A. Murray, A. Gundlach, D. Renshaw, B. A. D. Dhillon, A. A. O. Ohtori, Y. A. I. Inoue, and A. A. W. Walton (2007). *Development of a miniaturised drug delivery system with wireless power transfer and communication*. *Nanobiotechnology, IET* 1(5):80–86. doi:10.1049/iet-nbt:20070022
- [88] K. Tsougeni, A. Tserepi, and E. Gogolides (2007). *Photosensitive poly(dimethylsiloxane) materials for microfluidic applications*. *Microelectron. Eng* 84(5-8):1104–1108. doi:10.1016/j.mee.2007.01.011
- [89] Y. Wang, Y. Li, C. Rong, and J. P. Liu (2007). *Sm-Co hard magnetic nanoparticles prepared by surfactant-assisted ball milling*. *Nanotechnology* 18(46):465701. doi:10.1088/0957-4484/18/46/465701
- [90] F. Fahrni, L. J. van Ijzendoorn, and M. W. J. Prins (2008). *Magnetization and actuation of polymeric microstructures containing dispersed magnetic nanoparticles*. Submitted to the *Journal of Magnetism and Magnetic Materials*
- [91] Iverson and Garimella (2008). *Recent advances in microscale pumping technologies: a review and evaluation*. *Microfluidics and Nanofluidics* doi:10.1007/s10404-008-0266-8
- [92] C.-Y. Lee, H.-T. Chang, and C.-Y. Wen (2008). *A MEMS-based valveless impedance pump utilizing electromagnetic actuation*. *Journal of Micromechanics and Microengineering* 18(3):035044. doi:10.1088/0960-1317/18/3/035044
- [93] Micro Resist Technology GmbH (2008). *ma-N 400 and ma-N 1400 - negative tone photoresists*. <http://www.microresist.de/>
- [94] J. den Toonder, F. Bos, D. Broer, L. Filippini, M. Gillies, J. de Goede, T. Mol, M. Reijme, W. Talen, H. Wilderbeek, V. Khatavkar, and P. Anderson (2008). *Artificial cilia for active micro-fluidic mixing*. *Lab on a Chip* 8(4):533–541. doi:10.1039/b717681c
- [95] Wikipedia (2008). *Cilium — wikipedia, the free encyclopedia* [Online; accessed 16-May-2008]. <http://en.wikipedia.org/wiki/Cilium>
- [96] Wikipedia (2008). *Paramecium — wikipedia, the free encyclopedia*. [Online; accessed 15-May-2008]. <http://en.wikipedia.org/wiki/Paramecium>
- [97] X. Yang, R. Dillon, and L. Fauci (2008). *An integrative computational model of multiciliary beating*. *Bulletin of Mathematical Biology* 70(4):1192–1215. doi:10.1007/s11538-008-9296-3
- [98] G. Yi-Min, L. Zhi-Huan, Y. Yu, D. Xiao-Bo, W. Wen-Quan, W. Xue-Feng, S. Feng, L. Lei, Z. Zhi-Sheng, J. Han-Min, and W. Ge-Hui (2008). *Angular dependence of coercivity of grains in nanocrystalline permanent magnets*. *Chinese Physics B* 17(3):1130–1134. doi:10.1088/1674-1056/17/3/063
- [99] J. F. Zhong, Y. Chen, J. S. Marcus, A. Scherer, S. R. Quake, C. R. Taylor, and L. P. Weiner (2008). *A microfluidic processor for gene expression profiling of single human embryonic stem cells*. *Lab on a Chip* 8(1):68–74. doi:10.1039/b712116d